DESIGN AND PRELIMINARY MEASUREMENTS INSIDE A SIMPLIFIED HIGH TEMPERATURE GAS-COOLED REACTOR BUILDING

A Thesis

by

MARK BRYAN SILBERBERG

Submitted to the Office of Graduate and Professional Studies of
Texas A&M University
in partial fulfillment of the requirements for the degree of

MASTER OF SCIENCE

Chair of Committee,	Yassin A. Hassan
Committee Members,	Gerald L. Morrison
	Maria D. King
Head of Department,	Andreas A. Polycarpou

May 2017

Major Subject: Mechanical Engineering

ABSTRACT

A simplified high temperature gas-cooled reactor building was developed at Texas A&M University to understand the response of an actual facility to a depressurization accident scenario. A set of scaling laws were established to preserve the major flow phenomena and the geometry of the facility was simplified to focus on characterizing the key phenomena that determine the reactor building atmospheric concentration over time without the complexity of modeling the detailed features of an actual reactor building. The facility was outfitted with several instruments to measure localized oxygen concertation, pressure and temperature with the flexibility for the addition of measurement devices for future testing.

The design of the facility required computing the leak rate scaled to the amount of air leaked from the prototype facility in one day. After determining the target leak rate the facility leak paths were acclimated to allow for air to leak from the facility. This was achieved by adjusting a set of needle valves at select locations on the simplified facility. Comparison of the achieved leak rate with an analytical fit to the model was shown to have a high degree of statistical similitude from determination of the R^2 values. The analytical model was determined by assuming the helium and air inside the faculty behave as an ideal gas. Finally, several tests were conducted to characterize the phenomena for a sudden depressurization inside of the simplified test facility. The velocity in the flow path connecting two adjoining test volumes was determined from the response of the oxygen probes to air intrusion into the facility.

Finally, PIV measurements were conducted to analyze a helium buoyant jet flowing through a check valve that operates at 1 psid. Temporal resolution of the velocity field displayed erratic behavior in the region downstream of the inlet near the steam generator wall and was suspected to be from the development of flow instabilities from the difference in density between the helium jet and air. Entrainment effects were hypothesized to have occurred due to Rayleigh-Taylor instabilities that resulted in the development of vortical structures and local acceleration of the flow field.

DEDICATION

First and foremost, I would like to dedicate this work to all of my friends that have helped me along on this arduous journey. They know that it has been a bumpy ride, but without their support I know I would not be where I am today. For that, I am and will always be eternally grateful and I hope to one day return the favor to you guys.

This is to my mom, who supported me and gave me everything she could, even when there was nothing left to give. She showed me the value of hard work and was always there for me whenever I needed her to be. She showed me the value of independence and strength in the face of perseverance. To my brother-in-law Konrad, who helped me financially through some trying times when he most certainly did not have to and has been a wonderful addition to this family that I am deeply grateful for. To my dad, Jeff, who may not have been there in my life the way I would have preferred, but was there nonetheless and raised me, treated me as his own son and gave me his unconditional love.

Finally, to Michelle, who has been my support system through the tribulations one may face in life. Every day I get to spend with you is a privilege I never thought I would have and your unwavering support is the reason that I am where I am today.

ACKNOWLEDGEMENTS

I would like to thank my advisor, Dr. Yassin Hassan, who provided me with this opportunity and financial support to be a part of this amazing laboratory and gain invaluable knowledge that I am sure will set me above the rest. I would also like to thank Dr. Gerald Morrison, whose vast knowledge he imparted on me in the classroom has inspired me to always work to the best of my ability and never overlook any detail, no matter how small. Next, I would like to thank Dr. Rodolfo Vaghetto for consistently providing me with guidance and technical knowledge during my graduate studies. Finally, my appreciation goes out to Dr. Maria King, who is an excellent academic and incredibly sweet person. I am grateful to the guidance you and the rest of my committee has provided me during my time here at Texas A&M University.

My appreciation also goes out to my fellow labmates: Ethan Kappes, Christopher Fullerton and Andrew Mills, who have worked incredibly hard each day to ensure that we were always where we needed to be and made coming to work an enjoyable experience. I also want to thank Matthew Marciniak and Stephen King, who were there to help along the way. Next, I would like to thank Saya Lee, who first gave me the chance to work here and provided me with technical guidance and his continual friendship during my time working here. Finally, I want to thank my good friend John Budd, who without him, I would not have the opportunity to be where I am today. You helped me out when I needed it the most and I can never say thank you enough.

Lastly, I want to thank my good friends Jean Lim and Sero Yang. Jean extended his friendship to me and reached out to me when I expressed interest in being a part of this research. Our ongoing friendship is a testament to the appreciation I have. Sero Yang has been an excellent co-worker and even better friend. His wealth of knowledge I am always in admiration of, but his kindness is what makes me privileged to have worked alongside him.

CONTRIBUTORS AND FUNDING SOURCES

This work was supervised by a thesis committee consisting of Professor Dr. Yassin Hassan and Dr. Maria King and Gerald Morrison of the Department of Mechanical Engineering.

The facility was constructed with the help of Sero Yang, Duy Thien Nguyen and Matthew Marciniak. Experiments were conducted and the data was analyzed with the assistance of Duy Thien Nguyen, Sero Yang, Christopher Fullerton, Ethan Kappes, Andrew Mills and Matthew Marciniak.

All other work conducted for the thesis was completed by the student independently.

This material is based upon work supported by the Department of Energy [National Nuclear Security Administration] under Award Number [DE-NE0008324] in cooperation with AREVA Federal Service LLC (AFS), Ultra Safe Nuclear Corporation (USNC) and AREVA Inc. The views and opinions of authors expressed herein do not necessarily state or reflect those of the United States Government or any agency thereof.

NOMENCLATURE

A_x	cross-sectional flow area
a	scale parameter
B	buoyancy flux
b	translation parameter
β	bulk coefficient of thermal expansion
C_ψ	admissible constant
C_D	discharge coefficient
CMOS	complementary metal-oxide semiconductor
CFD	computational fluid dynamics
CV	control volume
D	diameter of intrusion
DAQ	data acquisition system
DOE	Department of Energy
D_{AB}	diffusion coefficient for gas species A and B
$D_{a,he}$	diffusion coefficient of air into helium
erf	error function
Fr	Froude number
FS	full span
f_{scale}	geometric scaling factor
GT-MHR	Gas Turbine-Modular Helium Reactor

Gr	Grashof number
g_0'	effective gravity
HPB	helium pressure boundary
HTGR	high temperature gas-cooled reactor
I_f^0	rate of fluorescence without quencher
I_0	rate of fluorescence with quencher
k	ratio of specific heats
k_q	quencher rate coefficient
L_M	buoyancy transition length scale
L_R	characteristic length scale ratio
LED	light-emitting diode
LWR	light-Water Reactor
m	mass of a component
M	momentum flux
$\dot{m}$	mass flow rate
mf	mass fraction
MTV	molecular tagging velocimetry
N	mole number
NIST	National Institute of Standards and Technology
NI	National Instruments
NPT	national pipe thread
NGNP	Next Generation Nuclear Plant

Nd:YAG	neodymium-doped yttrium aluminium garnet
NBR	acrylonitrile-butadiene rubber
P_{cr}	critical pressure
P_R	reduced pressure
P_{o_2}	percent oxygen
PIV	particle image velocimetry
PTV	particle tracking velocimetry
PBMR	Pebble-Bed Modular Reactor
PFA	perfluoroalkoxy alkane
$P'_{cr,m}$	pseudocritical pressure
Q	volumetric flow rate
$[Q]$	quencher concentration
R	specific gas constant
R^2	coefficient of determination
RCCS	Reactor Cavity Cooling System
RPV	reactor pressure vessel
Re	Reynolds number
Ri	Richardson number
Sc	Schmidt number
SGV	steam generator vessel
t_R	characteristic time scale ratio
T_{cr}	critical temperature

T_R	reduced temperature
$T'_{cr,m}$	pseudocritical temperature
u_f	root mean square error
u_R	characteristic velocity ratio
w	characteristic jet width
$W(a,b)$	continuous wavelet function
X_a	mole fraction of air
$X_{a,he}$	interface mole fraction of air and helium
y_i	mole fraction
z	compressibility factor
Ψ	dimensionless parameter
ν	kinematic viscosity
μ	dynamic viscosity
τ_0	chemical species emissive excited state lifetime
τ	correlated decay lifetime
v_s	specific volume
v_{actual}	specific volume of gas species
v_{ideal}	ideal specific volume of gas species
λ	decay constant
σ_T	pressure transducer uncertainty
σ_{cv}	curve fit uncertainty
ρ_∞	density of ambient air

ρ_j	density of jet
ψ	mother wavelet
σ_f	frequency width
σ_t	time width

TABLE OF CONTENTS

Page

LIST OF FIGURES

Page

LIST OF TABLES

Page

I. INTRODUCTION

The Next Generation Nuclear Plant (NGNP) project was established under the Energy Policy Act of 2005 to develop, license, build and operate a prototype modular high temperature gas-cooled reactor (HTGR) plant and is being executed in collaboration with industry, the United States Department of Energy (DOE) national laboratories, and United States universities [1], [2]. The HTGR, as one of the first proposed commercialized Generation IV nuclear reactor concepts, will simultaneously generate high-temperature process heat for use in hydrogen production and other energy-intensive industries while generating electric power at the same time [1].

The HTGR is a graphite-moderated, helium-cooled reactor with a thermal neutron spectrum that can supply nuclear heat and electricity over a range of core outlet temperature between 700 and 950˚C [3]. Current HTGR concepts are designed to operate at power levels lower than current light-water reactors, for inherent safety reasons, and will utilize coated fuel particles arranged into graphite spherical compacts, assembled either in hexagonal fuel assemblies or placed in a critical configuration, inside of an annular core [4]. For the prismatic core configuration, hexagonal moderator and fuel blocks are arranged to form an inner and outer graphite reflector region and a center region of fuel blocks that form the active core as shown in Figure 1 [5]. Heat generated through nuclear reactions is transmitted radially through the fuel block assemblies and removed by helium that enters the reactor core through a series of

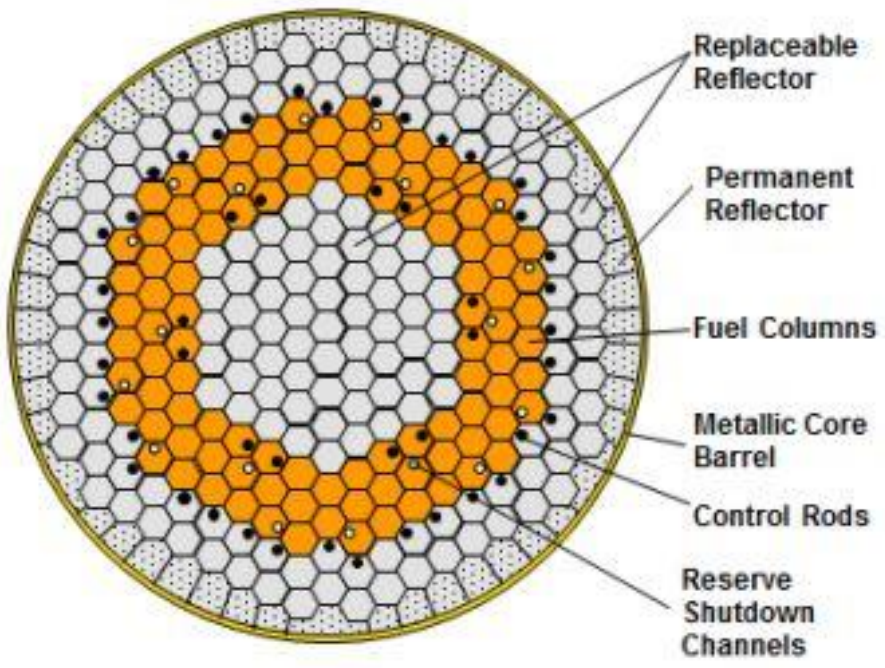

Figure 1. High temperature gas-cooled reactor prismatic core configuration [6].

integral coolant channels in the fuel assemblsies before being transferred to the power conversion system through the cross vessel and heat transport system [5].

Progress on HTGR technology in the United States is developing based on the prior work on the Pebble-Bed Modular Reactor (PBMR) Demonstration Pilot Plant, the General Atomics Gas Turbine-Modular Helium Reactor (GT-MHR) and Modular High Temperature Gas-Cooled Reactor (MHTGR) and the AREVA Antares design [7]. AREVA's 625 MWth steam cycle high temperature gas-cooled (SC-HTGR), based on the Antares concept, has been selected by the NGNP Industry Alliance as the reactor design concept of choice because it offers excellent inherent safety features including passive nuclear safety and unique high performance capabilities [6]. Among the

improved safety designs implemented in the SC-HTGR include an advanced fuel design that uses multiple ceram**ic** silicon carbide and pyrocarbide layers to prevent the release of metallic fission products, passive decay heat removal from the annular core without the need for electric power or operator intervention and a core with a large specific heat capacity [6]. Therefore, the remaining deployment challenges are largely commercial and regulatory as opposed to technological.

One of those challenges remaining for the near deployment of the HTGR is the confinement concept. For current light-water reactors (LWR) in operation, the containment is one of the three barriers to fission product release to the environment, the other being the fuel cladding and the reactor coolant pressure boundary that were part of the larger concept of defense-in-depth [8]. The confinement, on the other hand, refers to a vented low pressure containment that operates to limit positive pressure and is maintained at a slightly negative pressure during normal operation [8]. During a depressurization accident, the vent operates to limit pressure in the confinement to less than 7 kPa (1 psi) differential through a series of dampers that function similar to check valves and operate passively when the desired differential pressure is exceeded [8]. For a break size of 0.48 cm^2, depressurization takes place in 31 hours during which helium is released into the confinement continuously due to thermal expansion from core heat up and will last until the average core temperature has peaked [8]. However, the projected fission product release occurs long after the depressurization is completed, with no driving force to transport the fission products, and attempting to contain the helium can result in a higher fission product release rate than if the confinement has been vented [8].

Correspondingly, the fuel matrix is designed as a barrier to fission product escape up to temperatures of 1600˚C, lower than the projected operating fuel temperature of 1250˚C, and suggests that the vented confinement system is the more optimum approach to ensure public safety [8], [9].

The reactor confinement (building) for most conceptual HTGR designs are multi-celled, embedded structures constructed of cast-in-place reinforced concrete [10]. Most of the reactor building is situated below grade with an above grade portion of the east side of the reactor building serving as the Reactor Cavity Cooling System elevated inlet-outlet structure [10]. A similar but irregular above grade extension on the western end of the building encloses the main steam and feedwater lines and reactor building vent paths. The operating floor is set at site grade with the mechanical, electrical and instrumentation systems located two floors below grade [10]. The reactor building silo is configured into a cylinder and divided into a number of rooms and cells, the largest housing the reactor pressure vessel and is separated from the steam generator compartment by a 5-ft thick shield wall [10], [11]. A number of doors and pathways allow access to the cylindrical silo for piping, electrical services, personnel and venting from area to area [10], [11]. The reactor building silo is a reinforced concrete structure designed to transmit vertical loads and to resist horizontal loads due to soil and groundwater pressure [11]. Bearing walls are provided to resist load combinations and the outer walls of the reactor building are designed to withstand external threats including tornados, flooding, non-commercial aircraft crashes and missile-type events [8], [11].

A simplified HTGR building was constructed at Texas A&M University to evaluate and characterize the response of the facility to a postulated accident scenario where helium is discharged from the reactor pressure vessel through small or large size breaks in the helium pressure boundary. The facility was designed based on a set of scaling laws that are representative of anticipated flow behavior and preserve important characteristics of the test medium. A series of test instruments were outfitted to the facility to measure important aspects of the testing that include pressure, temperature and oxygen concentration. The oxygen concentration measurements were collected using a series of oxygen probes that measure the concentration based on the fluorescence time of a sensing material coated on the end of the probes and provided for the flexibility in measurements at different locations inside of the test facility.

The set of tests conducted were part of preliminary testing based on desired characteristics of the reactor building such as the amount of helium that would leak from the test facility and the performance of the test facility for different configurations. To supplement this testing, the velocity field in the region around the steam generator was collected using particle image velocimetry (PIV) to elucidate further features of the flow behavior by understanding more detailed flow structures that occur as a result of the mixing of helium and air and the effects of a stream of helium.

II. TEST FACILITY BACKGROUND

II.1 Simplified HTGR Building Model

The reactor building for both the prismatic and pebble bed HTGR designs is a vast network of compartments, instrumentation and mechanical and electrical systems that surround the reactor and associated systems that contain the helium coolant [8]. The cross sectional view of the reactor building in Figure 2 shows a number of these sections including the helium pressure boundary (HPB) that encompasses the reactor pressure vessel and steam generator vessel (SGV) that are connected by a welded cross vessel. The cross vessel provides flow paths for hot helium coolant leaving the RPV and flows concentrically to the cold helium entering the RPV that constitute the heat transport system [11]. From Figure 2, the other compartments also provide space for the Shutdown Cooling System and Reactor Cavity Cooling System (RCCS) that also remove heat from the core during normal operation and shutdown, although only the RCCS is passive and removes heat radiated from the RPV through the natural circulation of air [8], [10].

Given the complexity of the reactor building concept a complete analysis of normal or anomalous behavior, particularly depressurization accidents, would require a tremendous computational effort that may not be readily available or extremely time consuming. During the blowdown phase of a depressurization accident, hot helium from the HPB is injected into either the reactor or steam generator cavity over time scales

ranging from a few seconds to a day or more, depending on the break size. After the reactor building and HPB pressure equalize, further phenomena that can affect the confinement over time include natural convection, molecular diffusion, hydrostatic displacement, thermal expansion and contraction, building leakage enhanced by buoyancy effects, stratification and graphite oxidation occurring within the RPV.

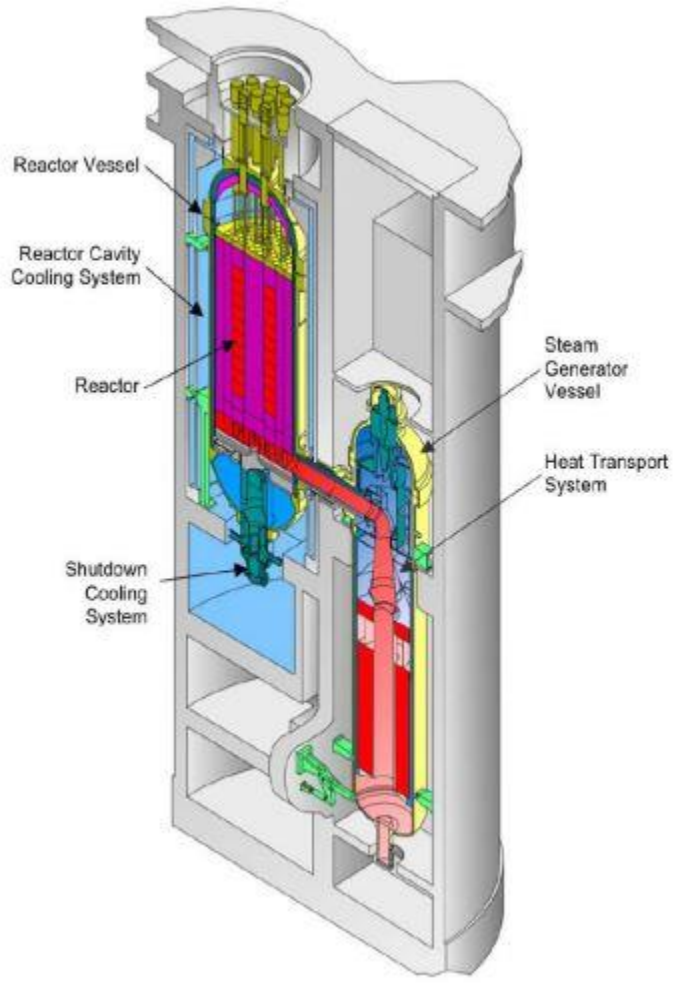

Figure 2. Cross-sectional view of an HTGR building [10].

To remove the complication involved with developing a full computational model of the reactor building and components, a simplified reactor building was proposed. The simplified model allows for a focus on characterizing the key phenomena that determine the reactor building atmospheric concentration over time without analyzing the subtle details of the flow discussed previously, although still significant. The simplicity of the model is dependent on a set of assumptions about the performance of the building during accident scenarios and of the intricacy of the geometry and distribution of helium inside the HPB.

The NGNP simplified reactor building model is not indicative of any current designs but will capture the relevant design features and phenomena that occur with an emphasis on depressurization accidents. The NGNP reactor building can be subdivided into five major components along the primary vent path during a pressure transient: 1.) reactor cavity with the RCCS, 2.) reactor cavity vent path to the steam generator cavity, 3.) steam generator cavity, 4.) equipment well vent compartment, 5.) louver vent compartment where the pressure relief valve module and gravity operated, fixed/hinged louvers are located and are indicated in Figure 3 for a similar General Atomics model. These five components form the basis of the simplified model that allows for an evaluation of the reactor building gas composition as a result of the expulsion of pressurized helium from the reactor pressure vessel and ingress of air into the reactor building. This simplification removes the geometric complexity of modeling the major features and components of the reactor building and allows for an emphasis on the underlying phenomena that are attributed to graphite oxidation when air chemically

reacts with the active core. Table 1 shows the design parameters for the simplified reactor building compartments, corresponding free volume, location on the general schematic shown in Figure 3 and a brief description of each compartment volume relative to the simplified model.

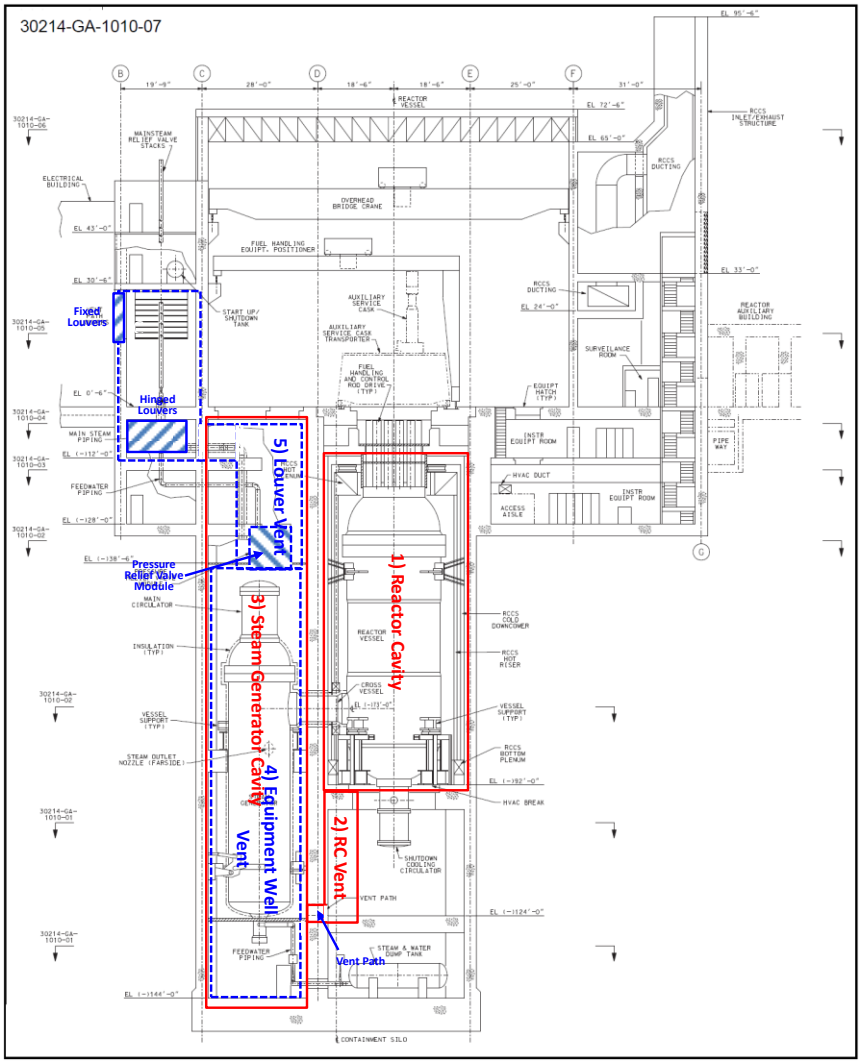

Figure 3. Primary components of the NGNP reactor building.

Table 1. Compartment/Cavity Design Parameters for Simplified Reactor Building Model.

Compartment/Cavity	Figure 4 Designation	Free Volume (cm^3)	Description
Reactor Cavity	CV1	$1.38 \cdot 10^9$	Houses the RPV. The RPV is approximated as a cylinder with a height of 80 ft., diameter of 22.4 ft. and volume of 31,530 ft^3. The free volume does not include an 10,000 ft^3 of space assumed to be occupied by other objects and are neglected in the simplified model.
Steam Generator Dump Tank Cavity	CV2	$4.56 \cdot 10^8$	Auxiliary storage for water/steam inventory during steam-generator rupture. May be neglected for simplified reactor building model.
Steam Generator Cavity	CV3	$1.44 \cdot 10^9$	Houses the SGV. The SGV is approximated as a cylinder with height of 81.5 ft., diameter of 14.8 ft. and volume of 14.020 ft^3. The free volume does not include an 10,000 ft^3 of space assumed to be occupied by other objects and are neglected in the simplified model.
Lower Vent Space	CV4	$2.38 \cdot 10^8$	Includes the one-way louvers represented by vent paths V34 or V64(a).
Upper Vent Space	CV5	$3.09 \cdot 10^8$	Includes the fixed louvers represented by vent path V5A.
Equipment Shaft	CV6	$1.28 \cdot 10^9$	Connections to steam generator cavity are represented by vent path V36 for analytical and scaling purposes. V34(a) represents an alternative path.

The complete schematic of the simplified HTGR building model with all characteristic vent and leak paths is shown in Figure 4. For completeness, the elevation relative to the ground is indicated with negative elevations signifying below grade and positive elevations above grade. The vent paths are indicated in Figure 4 with a "V" in front of two separate numbers, indicating the two compartments that are joined by the particular junction and leak paths are indicated by a "L" preceding a number and letter that designates the compartment where the leak is located. The "CV" indicates control volume, and from Table 1 there are six separate control volumes, each provided in the table with a brief description and simplifying assumptions. Therefore, L1A indicates a leak path in CV1, L3A a leak path in CV3 and L6A is a leak path in CV6. The vent path for relieving internal reactor building pressure is from V13 → V34 → V45 → V5A where V5A is the vent path from the upper vent space, CV5, to the environment. A separate vent path is provided that provides an alternative route through V36-1 that connects CV3 and CV6 out to the ambient environment through V64(a) that connects CV6 to CV4. The cross vessel that connects the reactor pressure vessel and steam generator vessel is assumed to provide direct communication between the two vessels, and consequently, L13 is not modeled as a flow path for relieving the reactor building internal pressure.

Vent paths V34(a) and V64(a) represent one-way louvers that open passively from a differential pressure and close passively by gravity. The one-way vent path V13 between CV1 and CV3 is modeled as both a one-way louver that operates similar to

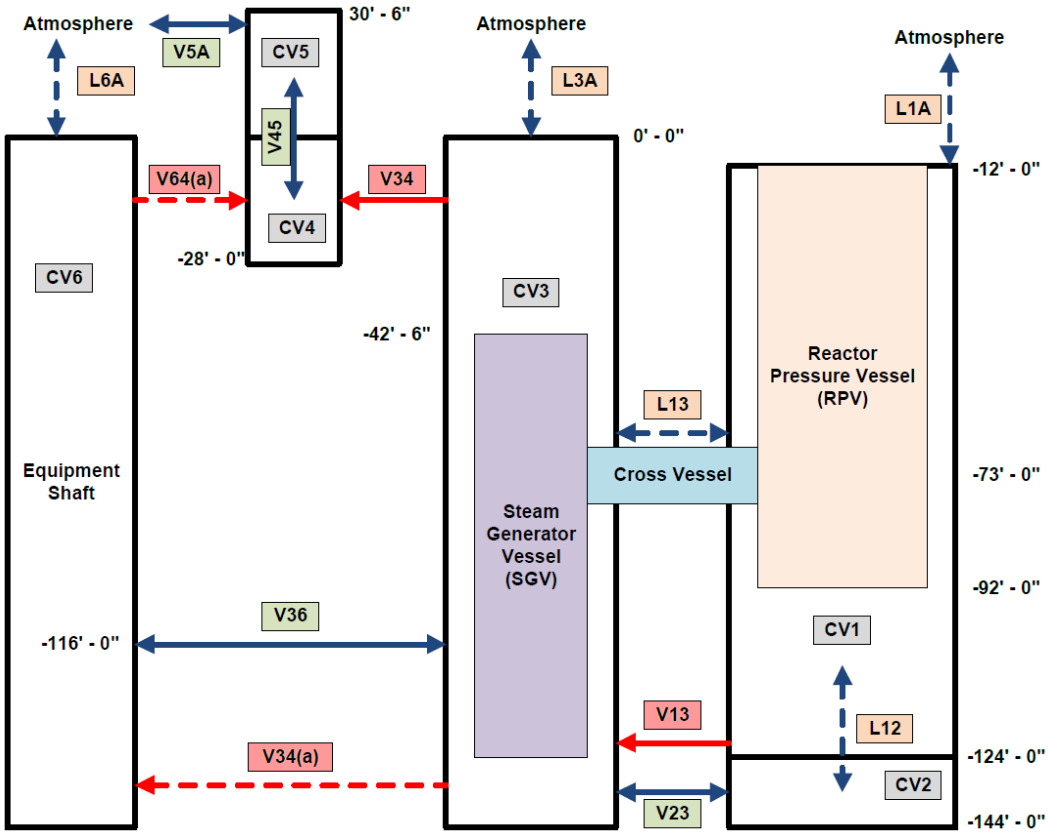

Figure 4. Schematic of the simplified reactor building model with vent and flow paths indicated.

a check valve when a differential pressure develops between the two compartments and a blow-out panel that will automatically fail and rupture at a predetermined pressure difference. V36, when activated is a lower pathway between the steam generator cavity, CV3, and the equipment shaft CV6. If CV6 is isolated from the system, then V34 represents the sole pressure relief vent path and is modeled similar to V34(a) or V64(a). V23 is a vent path from CV2 and CV3, but normally these two compartments are isolated from each other and remain separated for the simplified model considered.

Similarly, CV2 is normally isolated from CV1 except in the instances of a large-break primary helium depressurization event and may be modeled as a one-way louver or blow-out panel. For the present model CV1 and CV2 remain disconnected and L12 is inactive. The remaining vent paths in CV4 and CV5 represent one-way louvers that engage when the design differential pressure is exceeded and passively close by gravity. As an aside, in the event of a rapid pressurization of the reactor building, the discharge of helium from the helium pressure boundary could cause structural damage to critical vent path components such as the pressure relief valve or one way louvers. For this particular scenario vent paths V34(a), V34, V64(a) and V45 may be modeled as open channels that do not act to regulate the differential pressure between the reactor building and ambient environment.

Boundary conditions on the simplified model assume 100% air at ambient pressure inside of the reactor building and a prescribed temperature of 38˚C in every compartment except for the reactor cavity, or CV1, which maintains a constant temperature of 149˚C. Based on previous assessments, the reactor building is assumed to leak air from the building at a total of one building volume per day, the design limit through the leak paths L1A, L3A and L6A at the top of the reactor cavity (CV1), steam generator cavity (CV3) and equipment shaft (CV6), respectively. Although the leak paths are difficult to characterize for a prototypical reactor building, the leaks are not likely to be characterized by a single flow area and may or may not be visible to the naked eye. In fact, these leaks are more likely to be not readily visible but present as indistinguishable passages around the periphery of the floor or ceiling or penetrations

into the reactor building walls. Based on a previous assessment, 20% of the total reactor building leak rate is assumed to exit through L1A at the top of the reactor cavity, 30% through L3A at the top of the steam generator cavity and 50% through L6A at the top of the equipment shaft and are modeled, based on Equation (1), for flow through an orifice [12]

$$Q = C_D A_x \sqrt{\frac{2\Delta P}{\rho}} \quad (1)$$

where Q is the volumetric flow rate, A_x is the cross-sectional flow area of the leak, ΔP is the differential pressure and ρ is the density of air in the reactor building. C_D is the discharge coefficient, which is the ratio of the actual flow to theoretical flow derived from experimental data and is approximated to be 0.6 for the simplified model [12].

II.2 Scaling of a Simplified HTGR Building

The motivation for the scaling and design of the simplified experimental facility is derived from the scaling laws related to the major thermal hydraulic phenomena that is predicted to occur during a depressurization accident in the actual HTGR reactor building. The anticipated response of the reactor building to break in the helium pressure boundary that stimulates characterization of the relevant phenomena is dependent on the size of the break. The limiting scenario is a double-ended break of the cross vessel that

routes the helium between the reactor and heat transport system. A break at this location fully exposes the pressurized helium in the hot and cold legs to the reactor building atmosphere, leading to a rapid depressurization over a time period of about 3 seconds before equilibrium is reached between the helium pressure boundary and reactor building [13]. The blowdown phase also forces the initial air out of the reactor building to the atmosphere through the vent path but may later ingress back into the reactor building after equilibrium is reached by diffusion, referred to as density-driven flow, and form a helium/air mixture inside. A break in the cross vessel also provides a pathway for natural circulation through the core once air begins to ingress back into the reactor building. Natural circulation in the reactor cavity (CV1) driven by the temperature differences between the reactor pressure vessel and surrounding air may also influence the rate and characteristics of air ingress into the reactor cavity. Therefore, the primary thermal-hydraulic phenomena expected to occur in the reactor building after a depressurization incident when equilibrium is attained are [14]:

- Vertical stratification and mixing
- Horizontal stratification (gravity current)
- Gas thermal expansion and contraction
- Molecular diffusion of the binary gas mixture (air/helium)

The scaling methodology adopted for developing an experimental test facility that matches the prototype HTGR reactor building flow phenomena is based on the non-dimensional similarity approach previously employed in previous gas-cooled reactor research [15]. This analysis is carried out to evaluate the main dimensions of the

experimental test facility and emulate the flow characteristics of the reactor building prototype. Dimensionless parameters are selected based om the variables which govern thermal fluid transport and are identified from the length, velocity, temperature and time scales of the underlying flow behavior. In order to guarantee the dynamic similarity of the fluid flow of the *model* to that of the *prototype*, the ratio of the dimensionless numbers is established as unity by Equation (2) [16].

$$\Psi_R = \frac{\Psi_m}{\Psi_p} = 1 \tag{2}$$

where the subscripts *m*, *p* and *R* denote the model, prototype and the ratio of the two values, respectively.

Judicious selection of parameters that accurately capture the important flow phenomena that is expected to occur resulted in the following five dimensionless parameters shown below in Table 2. The identified dimensionless parameters were carefully applied through the scaling ratio in Equation (2) for the prototype facility characteristics and test facility characteristics. Matching the dimensionless numbers allows for the preservation of certain geometrical and dynamic properties through known conserved features. For example, dimensionless Schmidt number was considered when scaling down to the simplified test facility because it characterizes the molecular transport of momentum and species of gases. Material is transported due to the mean motion of the fluid through the process of *convection* and by random thermal motion of the molecules within the fluid through *diffusion*.

Table 2. Identified Dimensionless Parameters

Dimensionless Number	Description	Governing Parameters
Schmidt Number	$Sc = \frac{\nu}{D_{AB}}$	Ratio of momentum to mass diffusivity
Froude Number	$Fr = \frac{U^2}{gl\frac{\Delta\rho}{\rho}}$	Ratio of the flow inertia to the external gravitational field
Richardson Number	$Ri = \frac{g\beta\Delta TL}{U^2}$	Ratio of natural convection to forced convection
Grashof Number	$Gr = \frac{g\beta\Delta TL^3}{\nu^2}$	Ratio of buoyancy forces to viscous forces acting on the fluid
Reynolds Number	$Re = \frac{UL}{\nu}$	Ratio of inertial forces to viscous forces

Spatial variation in fluid density caused by temperature differences introduce buoyancy driven flows that can be evaluated through the Richardson number and Grashof number while the Froude number was selected because the facility is under the influence of gravitational forces.

The scaling factor resulted from matching the appropriate dimensionless numbers and manipulated based on the known similitude of certain parameters. The scaling factor was appropriately selected to avoid very small flow paths in the simplified facility, which may limit measurements capabilities if manufactured smaller than the available instruments, and the desired spatial resolution of the measurements to be obtained during

experiments [14]. Based on these considerations, the optimal length of the large volumes, or cavities, in the simplified test facility was determined to be approximately 1.6 m [14]. The largest cavities in the simplified reactor building design are the steam generator cavity and equipment shaft cavity and each have a total height of 43.89 m (144 feet) [11]. Therefore, geometric scaling factor, f_{scale}, is determined from Equation (3)

$$f_{scale} = \frac{L_p}{L_m} = \frac{43.89}{1.6} \approx 28 \tag{3}$$

Table 3 summarizes the scaling factors computed for the simplified experimental facility. The scaled reference velocity and time for diffusion were similarly derived from known conserved quantities and appropriate relation between the length scale that was derived from matching the dimensionless numbers.

Table 3. Scaling Factors for the Simplified HTGR Building Model

Scaling Factor	Description	Value
L_R (f_{scale})	Scaled Length	$1/28$
u_R	Scaled Reference Velocity	$1/5.3$
t_R	Scaled Time for Diffusion Process	$1/784$

III. TEST FACILITY OVERVIEW

III.1 Simplified HTGR Building Experiment Facility

The test facility shown in Figure 5 is a 1/28 geometrically scaled model of the prototype HTGR building and consists of six main volumes that mimic the simplified design proposed in Figure 4. The facility was design based on the scaling parameters defined in the previous section, practicality of manufacturing the facility and versatility in assessing different aspects of the flow performance with a variety of intrusive and non-intrusive measurement techniques. The six main volumes, labeled CV1 through CV6, sequentially, are indicated in Figure 5 by letters "**A**" through "**F**" and are connected by the junction and vent paths described in the previous section and indicated by letters "**a**" through "**g**." The six main volumes are: **A**.) CV1, **B**.) CV2, **C**.) CV3, **D**.) CV4, **E**.) CV5 and **F**.) CV6. The vent paths and connecting junctions are designated by: **a**.) L13, **b**.) V13, **c**.) V23, **d**.) V36, **e.**) V34 **f**.) V64(a) and **g**.) V45. Leak paths L1A, L3A and L6A are located at the top of CV1, CV3 and CV6 respectively but are not indicated on Figure 5. The leak paths at the top of the CV1, CV3 and CV6 are implemented by the installation of a series of needle valves that allow for precise control of the gas vented from the test facility.

The simplified HTGR test facility was fabricated out of polycarbonate sheets 1/2" thick and bonded together with a methylene chloride solvent to join the structure together and to prevent helium from leaking through the joined surfaces. Polycarbonate

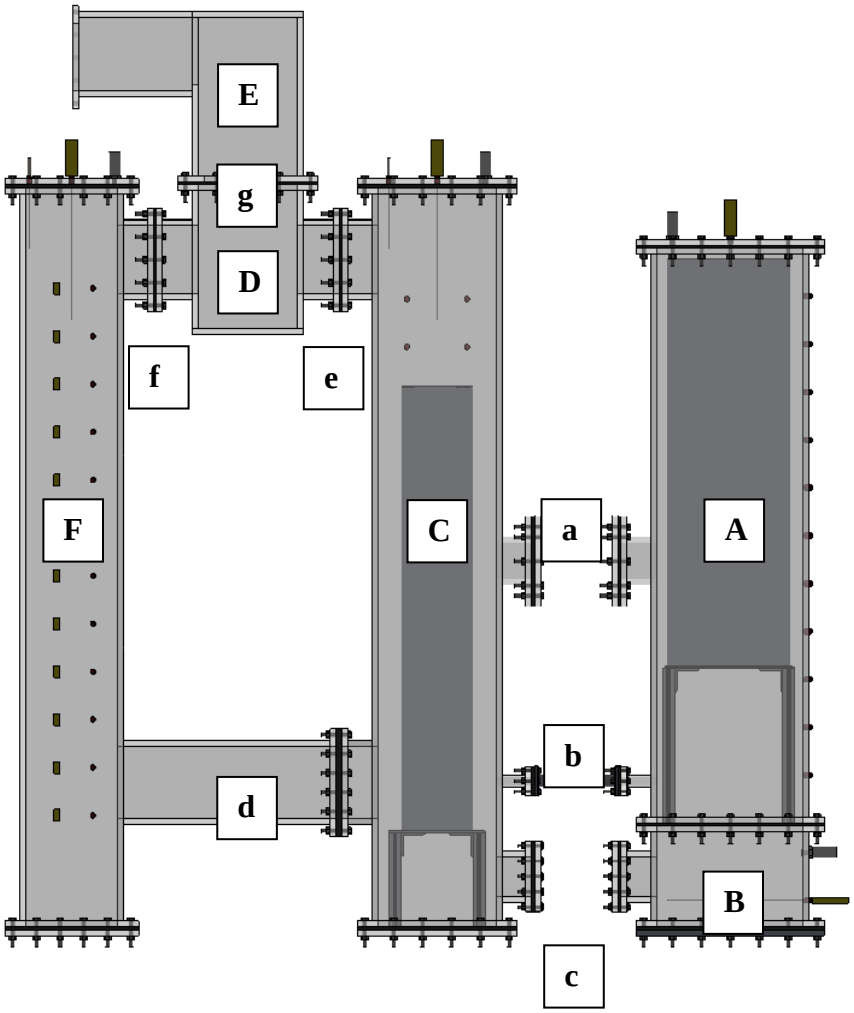

Figure 5. Simplified HTGR test facility with the main volumes and connecting junctions identified.

was selected for constructing the facility because it performs well at high temperatures up to around 150 ˚C, has high-impact resistance and low scratch resistance and can be penetrated easily for additional instrument installation [17]. Moreover, polycarbonate is highly transparent to light compared to other types of glass and plastic material that makes it suitable for non-intrusive and optical measurements including particle image

velocimetry (PIV), molecular tagging velocimetry (MTV) and particle tracking velocimetry (PTV).

The volumes are connected as described in Figure 5 by flanges at prescribed locations on each test volume with a neoprene gasket inserted between the two flanges as an additional barrier against the leakage of helium or pressurized air from the test facility. CV1 is connected to CV3 through the bypass system and check valve that is representative of V13 in Figure 4. CV1 is situated on top of CV2 with an aluminum sheet 1/16” thick placed between the gaskets and polycarbonate flanges bonded to the facilities that allows for support of the steel cylinder and aluminum stand. Main volumes CV1, CV2, CV3 and CV6 were manufactured with a series of 0.44” holes, situated in pairs along one of the walls of the chamber, for the installation of 1/4” NPT threaded instrumentation. Similar size intrusions were also drilled into the top of CV1, CV3 and CV6 for the installation of instrumentation, pressure relief valves, fittings for gas injection or other pertinent measurement devices. Two steel cylinders are situated inside of the test facility, one inside of CV1 that models the reactor pressure vessel and another inside of CV3 that represents the steam generator. Both steel cylinders are situated on top of an aluminum stand that both distributes the pressure applied to the floor of each test volume across the four legs and allows for easier accessibility. Figure 5 shows one configuration of the test facility with a pressure transducer and valve quick-disconnect fitting installed into the top of CV1, CV3 and CV6 and a series of 12 thermocouples along the front panel of CV6. There is also a quick-disconnect fitting and pressure transducer installed into the side panel of CV2 and multiple plastic plugs installed into

the side panel of CV1. It should be noted that Figure 5 is not indicative of the final instrument configuration and is modified depending on the experiment requirements and conditions. Any flow paths that are not in use are sealed with a solid polycarbonate panel 1/2" thick and bolted to the flange and gasket. The entire facility is housed in an anodized aluminum frame support structure to allow for greater mobility when manipulating each chamber and to protect it from outside disturbances. Test volumes CV1 and CV2, CV3 and CV6 are directly positioned on top of a second set of aluminum frame bars. The aluminum bars serve as a set of guide rails for moving the test volumes closer or further away from one another when disassembling or reassembling the facility or manipulating instrumentation. The current configuration of the simplified HTGR test facility is shown below in Figure 6 with all six test volumes connected together.

The two compartments of interest, CV1 and CV3, are those housing the reactor pressure vessel and steam generator vessel, respectively, and are approximated as rectangular prisms with square cross sections. CV2, CV4 and CV6 are also represented as rectangular prisms with the same symmetric cross section while CV5 is modeled as a combination of two rectangular prisms with symmetric cross section. The compartments are made to be removable from the entirety of the test facility and can be easily detached, replaced or reattached depending on the experiment requirements and conditions. CV6 was fabricated with a long polycarbonate channel that allows for cross communication between CV3 and CV6 that represents V36. A set of aluminum bars are

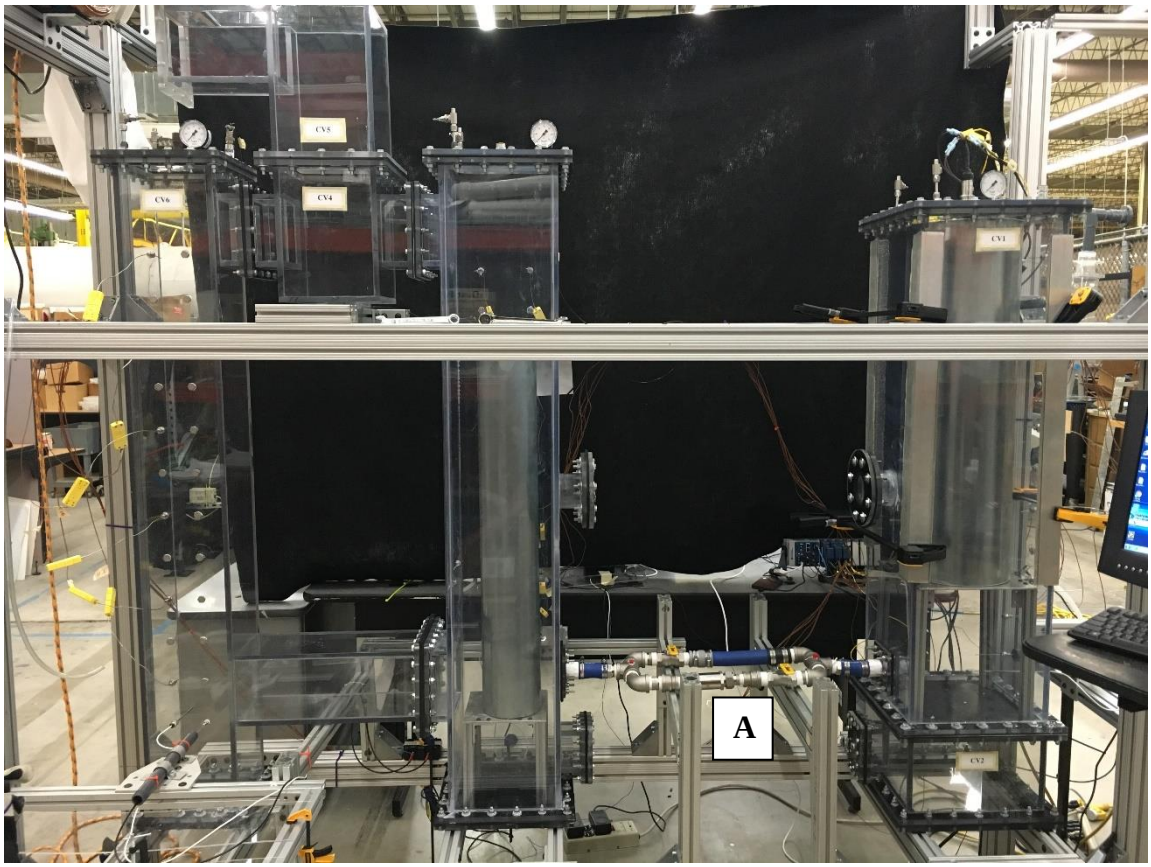

Figure 6. Fully assembled simplified HTGR building test facility. The bypass system is designated by the letter "**A**."

mounted to the aluminum frame structure adjacent to front panel of CV6 and behind CV3 to allow for the installation of an optical fiber oxygen sensor.

The main interior and exterior features of CV1 are presented as a cutaway in Figure 7 and is made transparent to show the relative position of the test volume to the entire test facility. The test volume is positioned on top of CV2 with a 1/16" thick aluminum plate bolted between the bottom flange of CV1 and the top flange of CV2. The dimensions of CV1 are 12.12" by 12.12" by 47", where the longest dimension is the

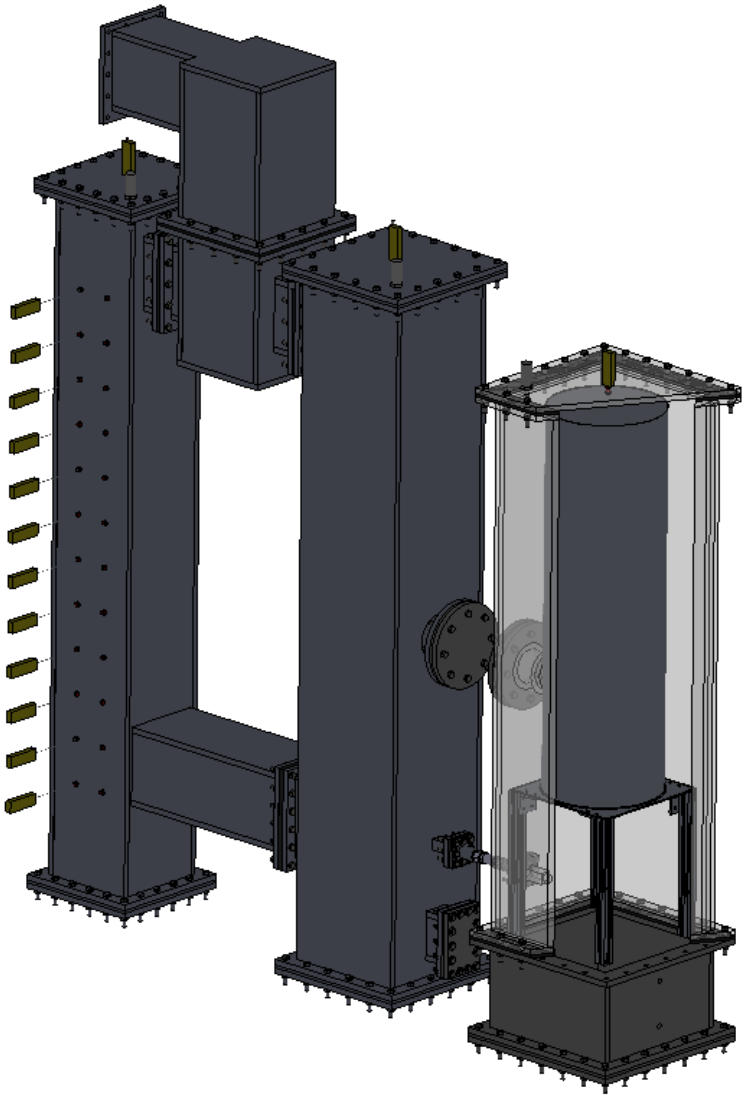

Figure 7. Test facility with a cutaway view of CV1.

height of the facility and 1/2” thick flanges 15.62” in length and 15.62” in width. The side panel that was removed in Figure 7 consists of a series of 0.44” bored through intrusions situated in 11 pairs from the bottom to the top of the side panel as displayed in Figure 8. All of the instrument ports except for the bottom and top pair are separated

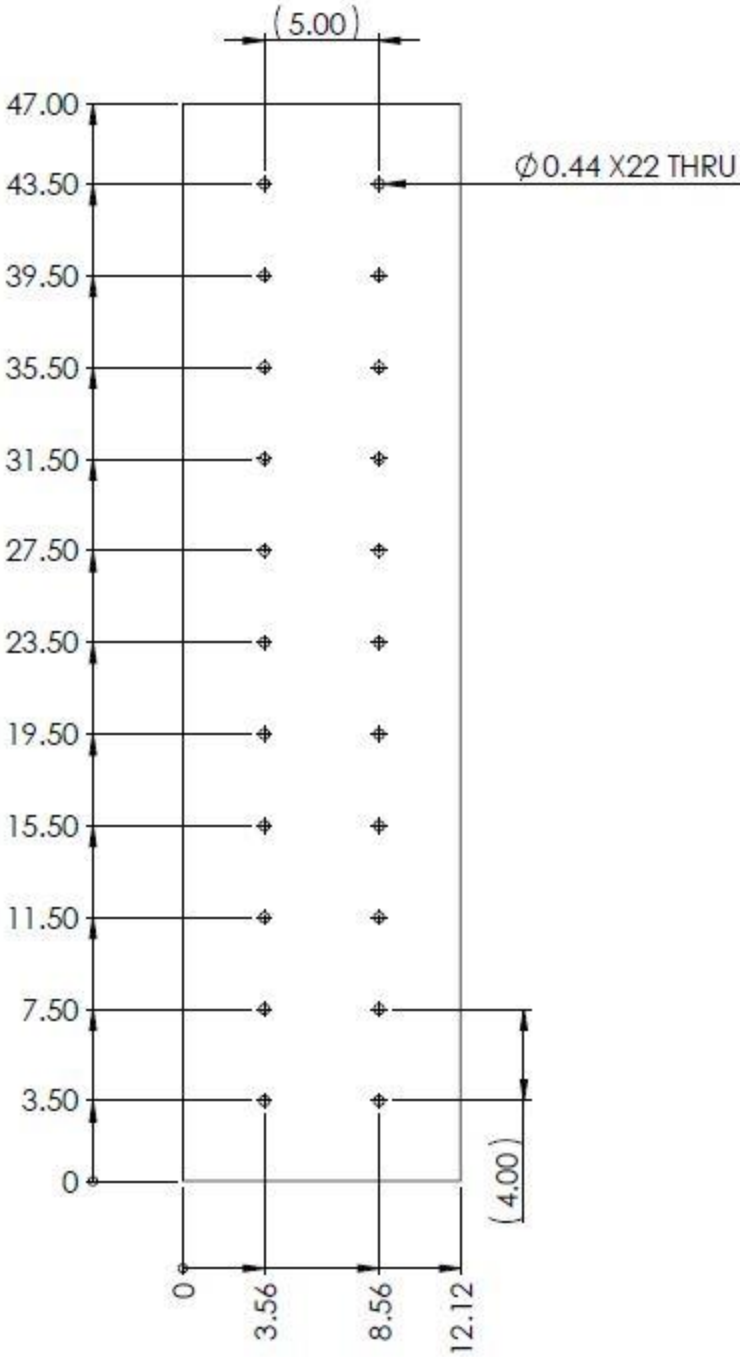

Figure 8. CV1 side panel with instrument ports and dimensions displayed.

by a 4” spacing and each pair of instrument ports is separated by a 5” clearing. The selected spacing was to allow for the installation or flexibility to install bulky or awkward instrumentation in the future and is not limited to thermocouples, oxygen sensors and inlet or outlet ports. The instrument ports were manually threaded with 1/4” NPT threading. Housed inside of CV1 is a hollow galvanized steel cylinder sealed at both ends with a steel lid that replicates the reactor pressure vessel inside of the reactor cavity. The steel cylinder has a diameter of 10.25” and a height of 34” for a total volume of around 2,805 in^3 and a side wall thickness of 0.05”. The empty space inside of the cylinder was filled with an insulating fireproof foam that insulates the heating pads attached to the inside walls and removes the void that pressurized helium or air might pervade during testing. The steel cylinder replicating the reactor pressure vessel is placed on top of an aluminum stand with legs 8.5” in length to reduce the pressure on the bottom polycarbonate panel of CV1 and to improve access to the cylinder.

CV2 is located directly below CV1 and at the base of the aluminum support structure and is shown as the transparent structure in Figure 9. The main dimensions of CV2 are 12.12” by 12.12” and a height of 7.40” with 1/2” thick flanges 15.62” in length and 15.62” in width. CV2 was manufactured with the same polycarbonate material as the other experiment volumes and has a 1.32” by 3.66” channel that serves as flow path V23 in the simplified HTGR model that the test facility is referenced from. Currently flow path V23 is not in direct communication with CV3 and is sealed closed for the current experiment phase with a solid polycarbonate flange cap roughly equal in dimensions to the channel flange. The side panel of CV2 opposite to the side panel with

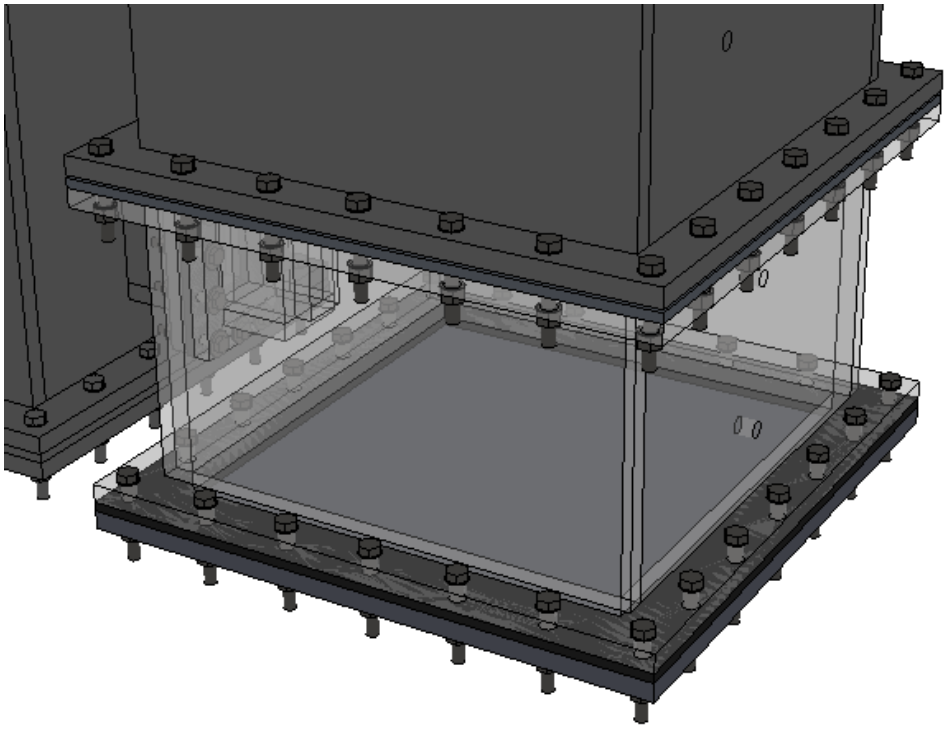

Figure 9. Transparent isometric view of CV2.

flow path V23 consists of two instrument ports equal in size to the instrument ports in CV1, spaced 4” apart, and is shown in Figure 10. Currently CV2 is isolated from the rest of the test facility but may be modified in future experiment phases to allow for direct communication between CV1 and or CV3. There are currently no instruments installed inside of CV2 but there is a quick-disconnect fitting connected to the lower instrument port for performing preliminary leak tests on the volume. It should be noted that CV2 is situated on top of a set of aluminum bars that act as guide rails for moving

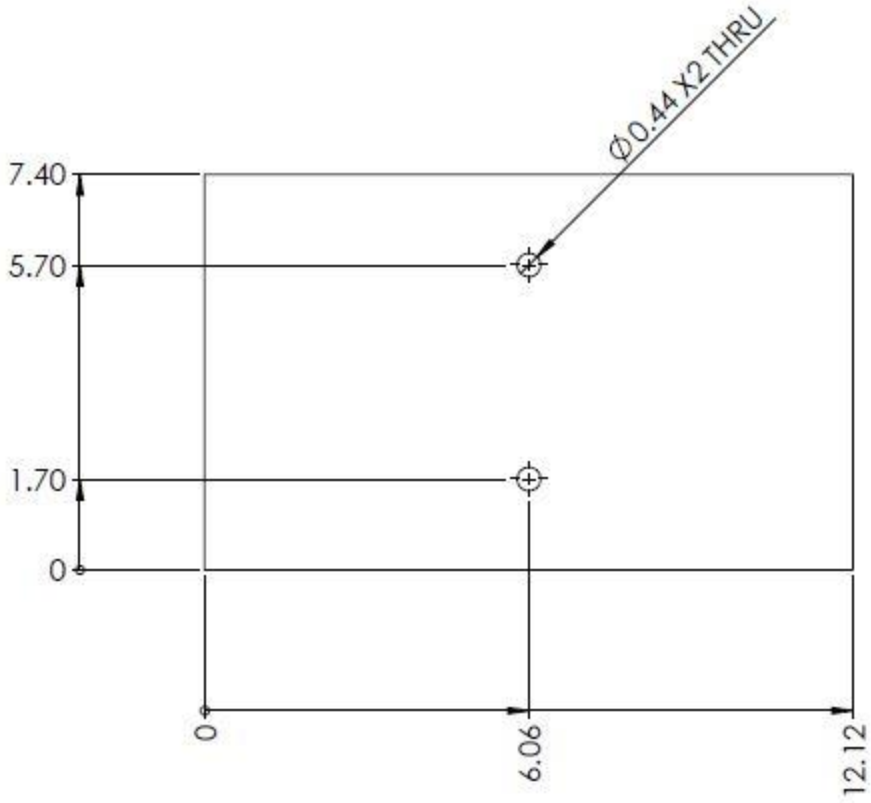

Figure 10. CV2 side panel with instrument ports and dimensions displayed.

both CV2 and CV1 in unison either closer or further away from the rest of the test facility when manipulation of the test facility is necessary.

CV3 is shown in Figure 11 relative to the simplified HTGR test section and is made transparent to display the internal as well as the external features. The facility stands at a height of 60.70” with base dimensions of 9.77” by 9.77” with a 1/2” thick square flange 13.27” in length. The facility has multiple flow path channels, as displayed in Figure 11. V34 is the flow path from CV3 to CV4 and the outer environment and has inner dimension of 5.64” in height and 4.32” in width. V36 is the flow path from

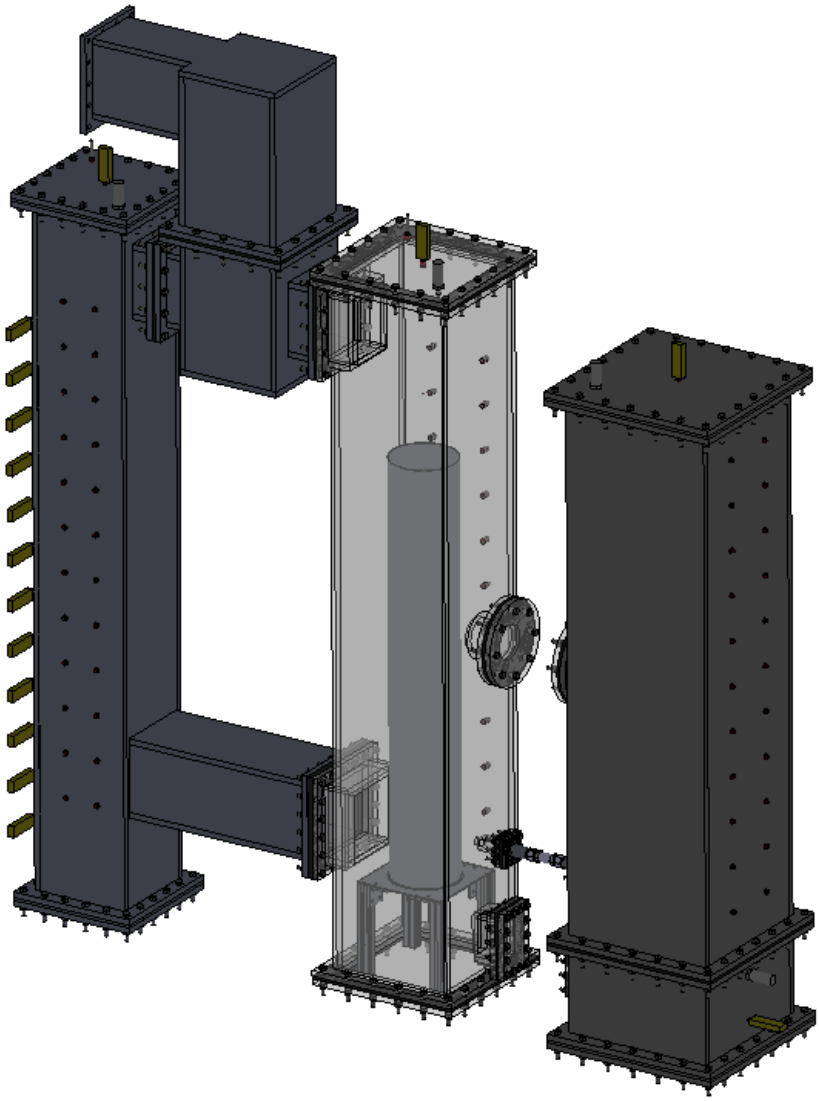

Figure 11. Transparent isometric view of CV3.

CV3 to CV6 and is shown in Figure 11 by the long channel 17.17” in length that leads directly to a secondary exhaust path through CV4 and CV5 to the ambient environment. As noted previously, V23 is currently not available and sealed with a polycarbonate flange equal in dimensions to the channel flange of CV3 and CV2. Future testing may

necessitate the direct communication of these two test volumes, which may be easily facilitated. The bypass system shown in Figure 6 and designated by the letter "**A**" is connected directly to CV1 and has an inner circular diameter of 0.68." The bypass system represents flow path V13 in the simplified model described in the previous section and is indicated in Figure 11 by a check valve that connects CV1 and CV3. The variance in the connection from CV1 and CV3 is due to a modification of the facility that allowed for more flexibility in manipulating the system without damaging the small channels when removing and connecting the check valve to the test facility. Therefore, the small flanges and channels were removed and replaced by the bypass system shown in Figure 6. Flow path L13 that represents the cross vessel has an inner diameter 3," but is currently not in service and closed off on both CV3 and CV1 with a circular polycarbonate flange caps to prevent pressurized air or helium leakage. The side panel with the instrument ports is shown in Figure 12 for CV3 and is located on the back of the test volume. The 11 pairs of instrument ports are spaced 4" apart except for the top and bottom instrument ports, which are spaced 8.80" and 11.90" from the top and bottom, respectively. Each pair of instrument ports is spaced 5" apart and are 0.44" in diameter. The instrument ports were threaded with 1/4" NPT threading and is the standardized thread size through the entire test facility.

The steel cylinder residing inside of CV3 is situated on top of an aluminum stand similar to the one in CV1 and has a height of 12". The galvanized steel cylinder has a similar thickness as that in CV1 with a height of 37.06" and an outer diameter of 5.88"

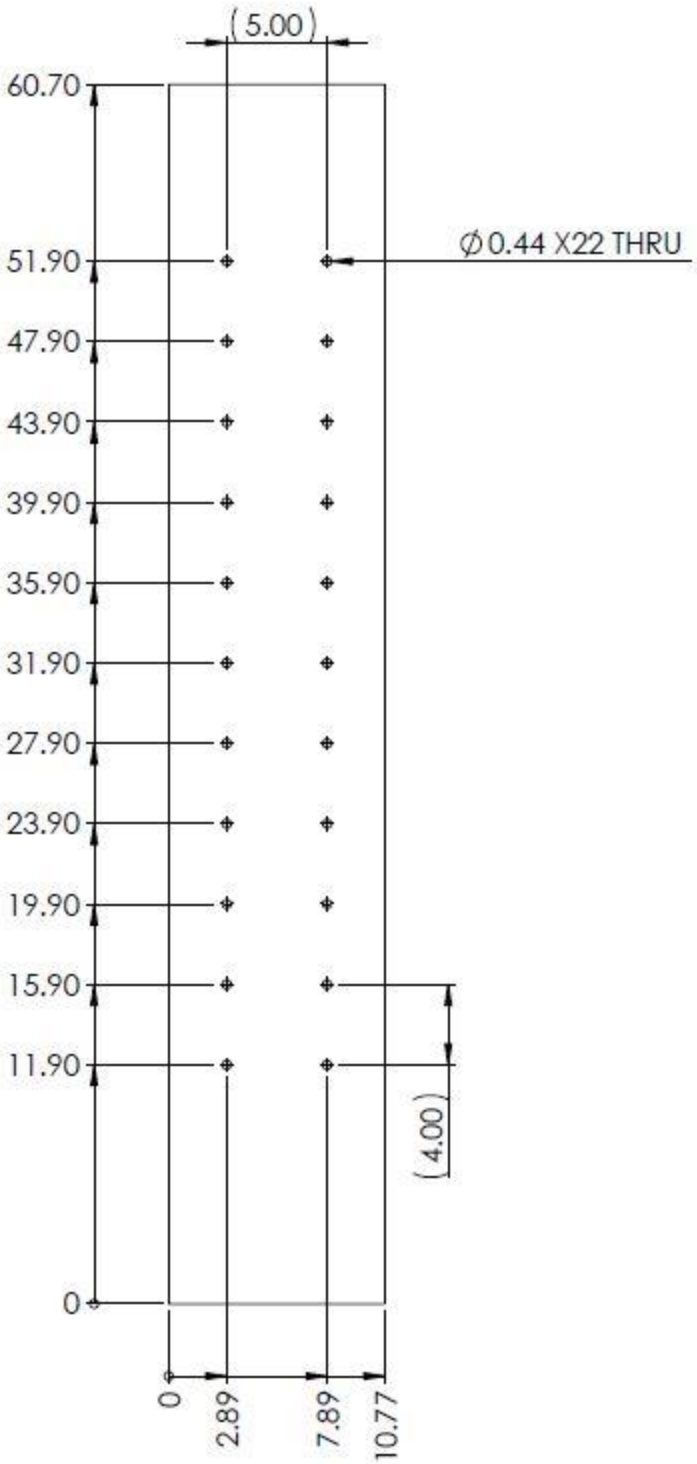

Figure 12. CV3 side panel with instrument ports and dimensions displayed.

for a total volume of around 1006 in^3. The steel cylinder represents the simplified steam generator model and was also filled with the same insulating foam for the cylinder in CV1 to prevent air or helium from migrating inside. As an aside, there are no heating pads inside of the cylinder located inside of CV3, as opposed to the cylinder situated inside of CV1. The cutaway view of CV3 in Figure 13 gives a detailed view of the interior of CV3; including the position of the aluminum test stand balancing the steel cylinder.

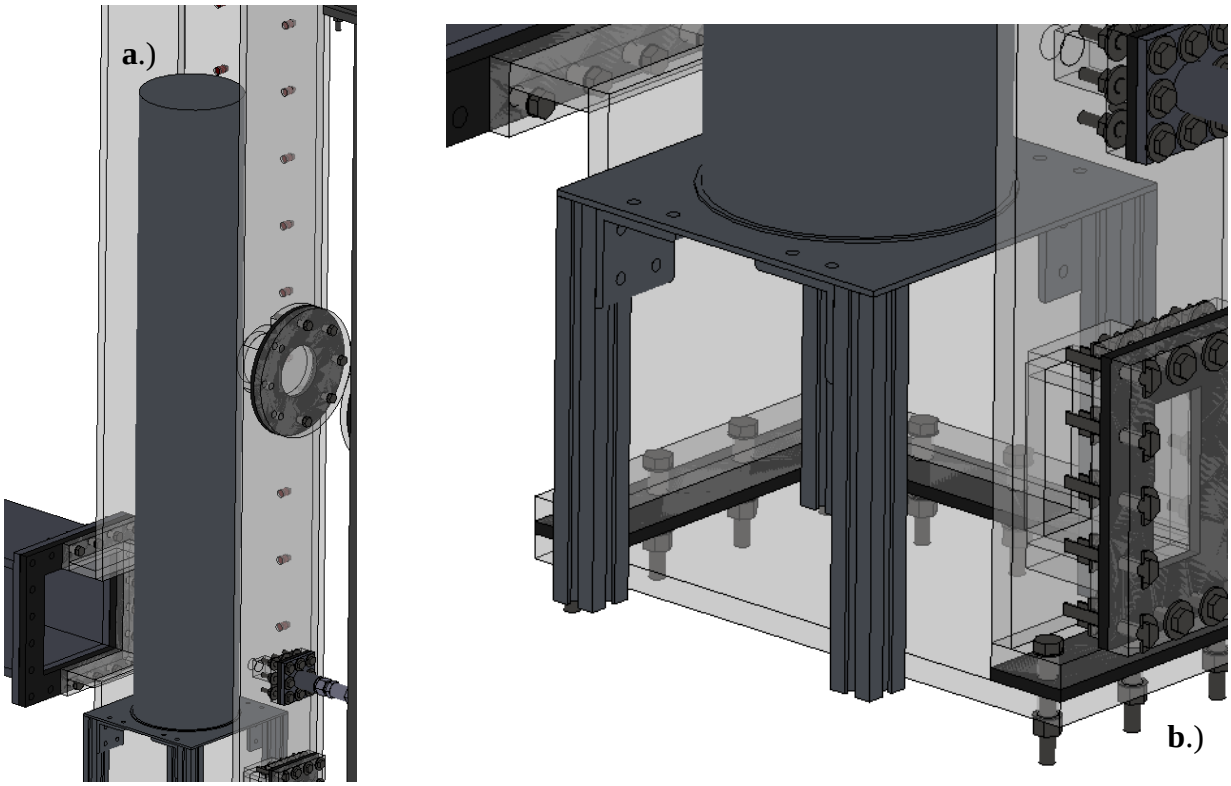

Figure 13. a**)** Cutaway view of CV3 with steam generator model and aluminum test stand shown**, b.)** Improved view of the steam generator model aluminum stand.

CV4 and CV5 are located at the top of the aluminum support structure directly between CV3 and CV6 and are indicated below in Figure 14 as the transparent assemblies.

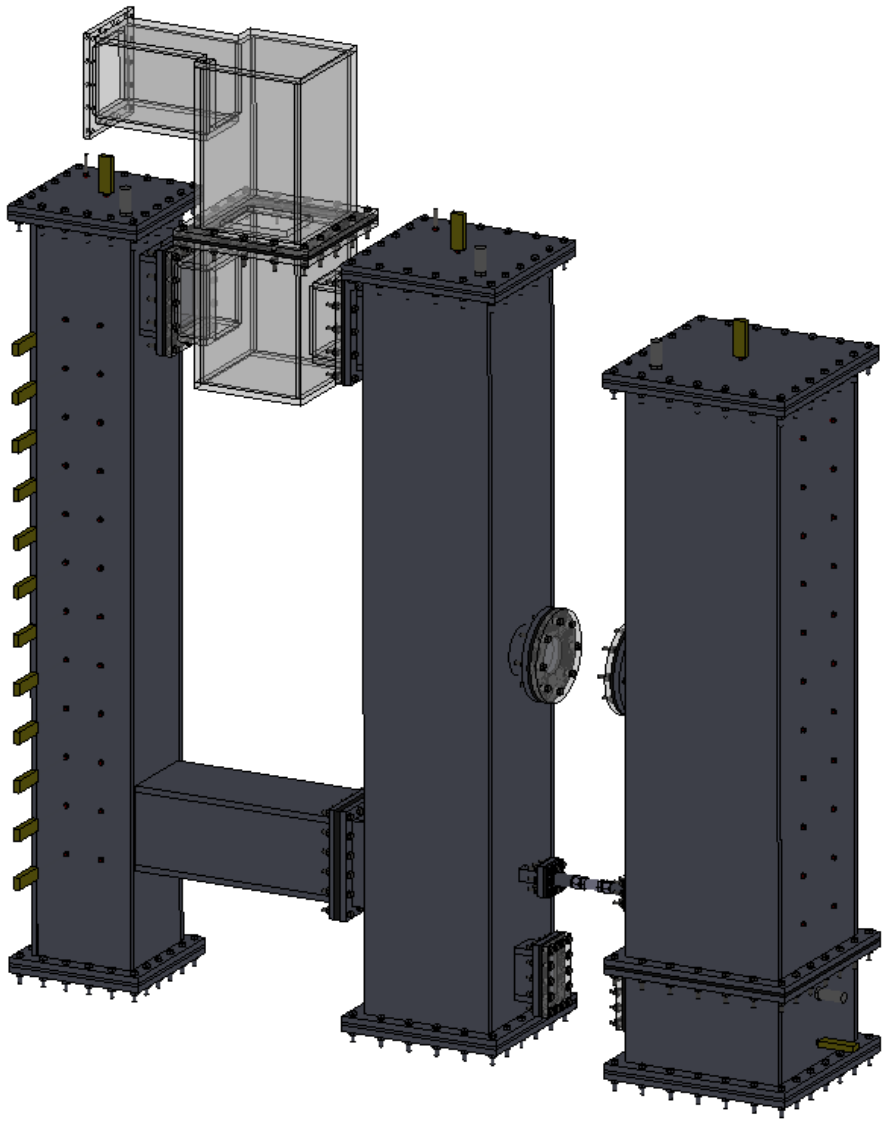

Figure 14. Transparent isometric view of CV4 and CV5.

CV4 is bolted to CV3 and CV6 at the channel flanges, each having the same inner dimensions of 5.64” in height and 4.32” in width. CV4 has a height of 11.50” and a square base 8.16” in length. Flow path V34 is the connecting junction between CV3 and CV4 and V64(a) is the flow path between CV4 and CV6, both representative of the flow paths in the simplified HTGR building model described previously. The channel openings are located both 2.93” from the top and bottom of the facility on both sides of CV4. The square flange connecting CV4 and CV5 has square dimensions 11.66” in length. Depending on the experiment conditions, either or both flow paths can be removed from the rest of the test facility by placing a thin solid aluminum plate between the flanges connecting either or both CV3 and CV6 to CV4.

CV5 is situated directly on top of CV4 with a 1/8” neoprene gasket placed between the flanges of both facilities to prevent leakage of pressurized air or helium through the small clearance. CV5 has the same inner square dimensions as CV4 where the two test volumes meet and height of 13.20.” However, unlike the previous control volumes, CV5 has an irregular shape with a 90˚ bend into a second rectangular channel with a length from where the first rectangular section ends of 9.50” and a width of 4.32.” The exhaust channel where gas is discharged from the facility has inner dimensions of 5.64” in height and 4.32” wide. The vent path V45 is represented by the opening where CV4 and CV5 are bolted together. Flow path V45 may be left completely open or the area may be reduced by inserting a polycarbonate plate with an extruded region of a desired area size between the two control volumes. There are no intrusions into either CV4 or CV5 for the installation of instrumentation or measuring devices.

Figure 15 shows a transparent view of CV6 with thermocouples in the instrument ports on the front panel of the facility to illustrate how instrumentation may be installed into the facility. From Figure 15, CV6 is located on the far left side of the facility and stands at a height of 60.70” with a square base 8.08” in length.

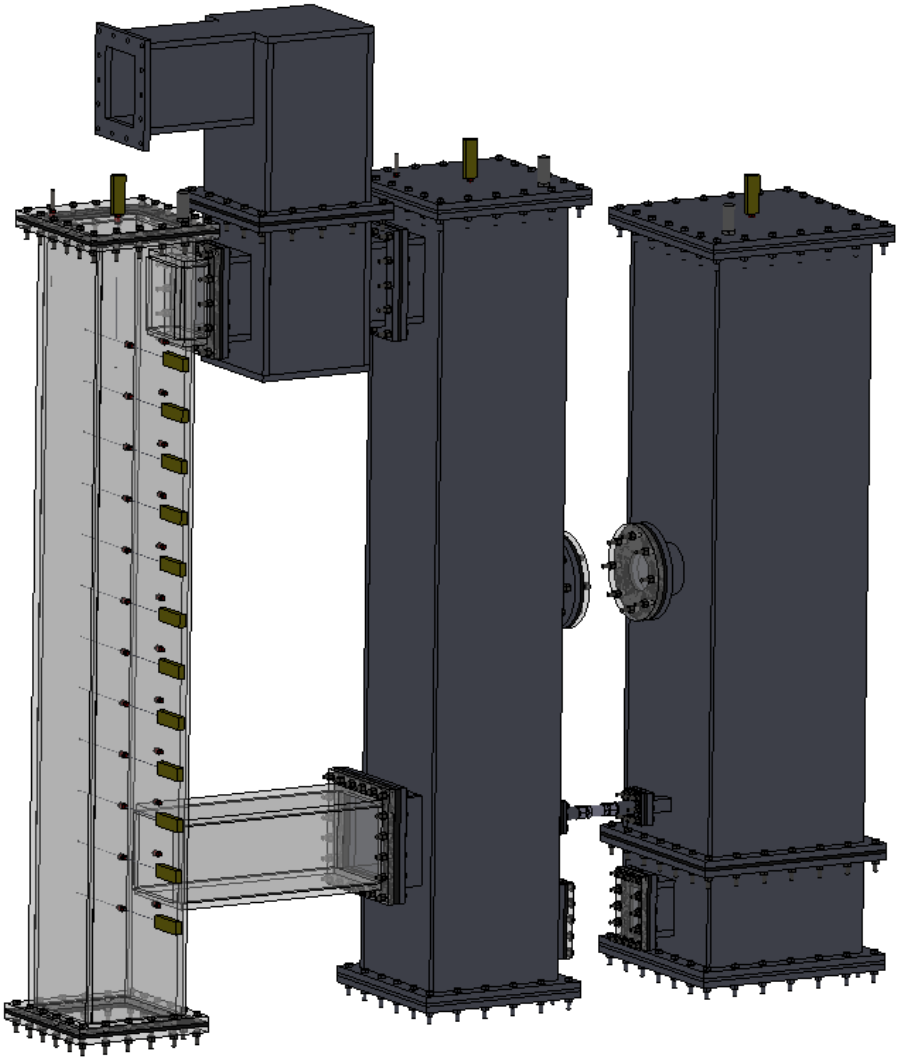

Figure 15. Transparent isometric view of CV6.

CV6 is situated directly on the bottom of the aluminum support structure and a set of aluminum bars that serve as guide rails for moving the facility away or towards the rest of the test facility for cases where CV6 may need to be isolated. The bottom and top flanges have a length and width of 11.08.” Similar to CV1 and CV3, five 0.44” inch intrusions are located in the top flange for instrumentation or quick-disconnect fittings for gas hose lines. The long channel connecting CV6 and CV3 models flow path V36 and has a length of 17.17” and a height of 7” with inner dimensions of 6” by 6.” The front panel of CV6, shown in Figure 16, has 12 pairs of 0.44” intrusions spaced 4” apart and a clearance of 3” between each pair of intrusions. The penetrations were threaded to facilitate the installation of instrumentation or purge valves.

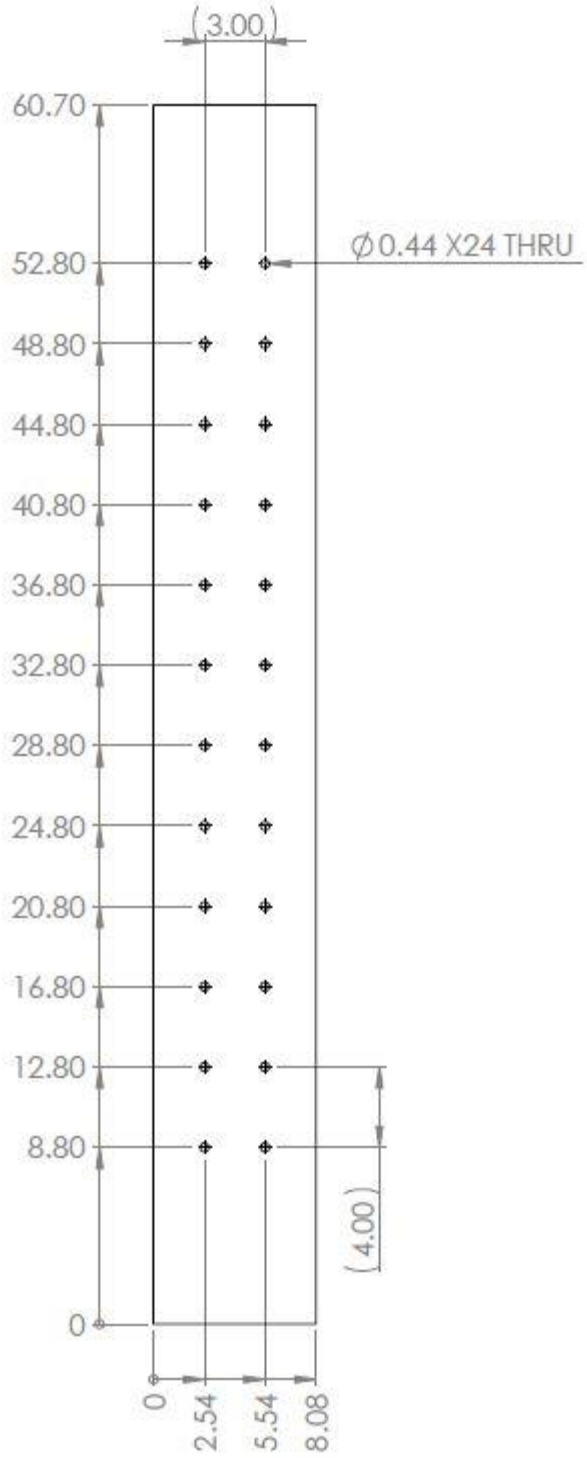

Figure 16. CV6 side panel with instrument ports and dimensions displayed.

III.2 Instrumentation and Measurement Devices

Various instruments were utilized during the course of the analysis described in later sections to collect spatial temperature, pressure and oxygen concentration measurements. Most of the instruments have 1/4" NPT tapered threads for direct installation into one of the many instrument ports located throughout the facility and allow for spatial and temporal measurements. The capability to remove and mount the instruments in different configurations throughout the facility also provides the flexibility to collect a set of data in a variety of arrangements or isolate specific regions for measurement. Further instruments were added to the facility as deemed necessary, including mechanical devices to supplement the analog and digital devices in situations where they are not available or have failed.

Temperature measurements are collected using a series of 20 quick disconnect, k-type thermocouples with a 1/16" diameter PFA coated stainless steel probe 12" in length as shown below in Figure 17. The thermocouple probes are manufactured by Omega® and consist of nickel-chromium thermocouple wire that is rated for up to 1250˚C with a standard error on each thermocouple of ±2.2˚C. The thermocouple probes were wired to the data acquisition system using 24-gauge k-type thermocouple wiring.

The pressure was recorded using Omega® high performance pressure transducers with a twist-lock connection and are shown below in Figure 18. The pressure transducers use silicon strain gages bonded to the stainless steel diaphragm and have an accuracy of 0.25% FS (full span), high stability with low drift. The pressure

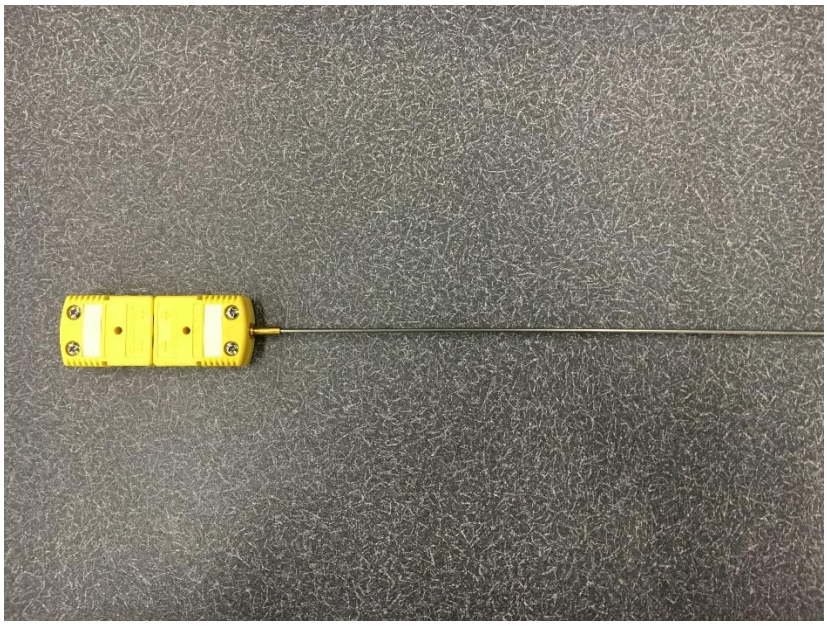

Figure 17. K-type thermocouple probe.

Figure 18. Pressure transducer.

transducers have a 5 psi gage (psig) pressure range and a 0 to 5Vdc output that requires a 10Vdc excitation signal. The excitation signal is provided by an external Mastech® HY3003D extremal DC power supply. CV1, CV3 and CV6 currently have a pressure transducer installed in the top flange for a total of three pressure transducers in the test facility and each pressure transducer was provided with a 5-point NIST traceable calibration.

Oxygen concentration measurements were recorded using an Ocean Optics R-Series oxygen sensor probe connected to a NeoFox-GT small footprint phase fluorimeter. The oxygen sensor are stainless steel probes 6” in length with a 1/16” diameter. The oxygen probe emits a 450 nm blue LED excitation light signal that is transmitted to a sensing material through a fiber optic cable 0.04” in diameter. The sensing material is a ruthenium compound integrated into a silicone matrix and applied to the end of the oxygen probe tip and has good thermal mechanical stability, is resistant to chemical corrosion in harsh environments and has a rapid response [18]. The sensing material at the end of the probe absorbs the emitted blue LED light and fluoresces within the red region of the spectrum. Diffusion of oxygen into the sensor coating quenches the fluorescence and reduces the fluorescence intensity as well as the time the fluorescent material spends in an excited state before returning to the ground state through photon emission [18]. The quenching happens because an excited indicator molecule has come into contact with an oxygen molecule, transferring its excess energy to the oxygen molecule in a non-radiative transfer [18]. The degree of fluorescence quenching depends

on the frequency of collisions, and therefore on the oxygen concentration of the sample, as well as its pressure and temperature [18]. One key advantage of this technique is that oxygen is not consumed during the measurement process. The phase shift and lifetime of the fluorescence is related to the oxygen partial pressure and can be calibrated to determine the oxygen concentration.

Once the phase shift is measured, it can be related to the oxygen concentration or partial pressure using the Stern-Volmer relationship in Equation (4)

$$\frac{I_f^0}{I_f} = 1 + k_q \tau_0 \cdot [Q] \tag{4}$$

where I_f^0 and I_0 is the intensity, or rate of fluorescence without and with a quencher, respectively, k_q is the quencher rate coefficient, τ_0 is the lifetime of the emissive excited state of a chemical species and $[Q]$ is the concentration of the quencher [19].

The oxygen probes are connected through an optical fiber cable to the USB port of the NeoFox-GT fluorimeter. The NeoFox unit is self-contained and is invariant to fiber bending and stray light and has a wide dynamic range of optical intensity as well as low optical and electronic crosstalk, and low drift and phase noise [20]. The device has a data logging rate of 10 Hz with an accuracy of ±160 μA in the 4-20 mA (milliamp) range and ±50 mV (millivolt) in the 0-50 V range [18]. The NeoFox-GT optically stimulates and measures the fluorescent decay rate of the probe's sensing material according to the luminescent phase shift. The output of the hardware's measurement of

the decay rate is a variable referred to in the sensor's literature as τ, and although it is correlated to the decay lifetime it is not the actual measurement of the lifetime itself [18]. The relationship between τ and the sensing material's response to the partial pressure of oxygen and temperature can then be used to calculate the partial pressure as a percentage of 1 atm (atmosphere) of oxygen from known values of τ and temperature. The partial pressure may then be converted to different units of oxygen concentration measurement including dissolved oxygen concentration and "converted oxygen."

If pressure and temperature cannot be controlled and kept constant from calibration to measurement, they must also be factored into the calculations and can be compensated for through the NeoFox-GT unit's internal pressure transducer, external temperature thermistor and independent calibration curves. More specifically, if the environment is not held within ±1˚C, then temperature compensation is required because temperature affects the excited state lifetime of the indicator complex, decreasing its fluorescence energy quantum efficiency as temperature increases [19]. To account for temperature variations in the experiment setting a NEOFOX-TP thermistor was installed into the facility within the vicinity of where an oxygen sensor was located and connected to the NeoFox-GT sensor. For calibrating the NeoFox-GT unit and oxygen sensor two different methods apply: 1.) two-point conversion and 2.) multi-point conversion. The two-point conversion uses two samples of oxygen-τ pairs to approximate a linear relationship between the reciprocal of τ and oxygen and is described in Equation (5)

$$P_{o_2} = A + B + \frac{\tau_0}{\tau} \tag{5}$$

where P_{o_2} is the "percent oxygen," which was described previously as the partial pressure expressed as a percent of 1 atm, A is the two point calibration offset, B is the two point calibration slope, τ_0 is the decay constant expressed at a known condition and τ is the value produced at a secondary reference point [20]. Generally, ambient air is used as one of the two reference points, since the percent oxygen can be reliably assumed to be 20.9% and the second reference point must be a second sample taken at 0% oxygen. This method less involved than the multi-point calibration method but is less accurate does not consider temperature when calculating the partial pressure of oxygen from τ. The multi-point calibration method is more arduous compared with the two-point method but account for the effects of temperature on τ. Essentially, many samples are taken over the applicable measurement range, each with a known τ, temperature and oxygen percent. The samples are then curve fit with second order polynomial approximations to produce the conversion in Equation (6)

$$\begin{aligned} AA &= T \cdot T \cdot A_0 + T \cdot A_1 \cdot A_2 \\ BB &= T \cdot T \cdot A_0 + T \cdot B_1 \cdot B_2 \\ CC &= T \cdot T \cdot C_0 + T \cdot C_1 \cdot C_2 \\ TT &= T \cdot T \cdot A_0 + T \cdot T_1 \cdot T_2 \end{aligned} \tag{6}$$

where A_0, A_1, A_2, B_0, B_1, B_2, C_0, C_1, C_2, T_0, T_1, T_2 are constants for the temperature dependent coefficient equations, T is the temperature in Kelvin, and AA, BB, CC and TT are the temperature dependent coefficients for the final oxygen conversion equation. The percent oxygen is then computed as follows in Equation (7)

$$P_{0_2} = \frac{TT}{\tau} \cdot \frac{TT}{\tau} \cdot AA + \frac{TT}{\tau} \cdot BB \cdot CC \tag{7}$$

Because of the high level of sensitivity to the surrounding conditions, the oxygen probes and NeoFox units were carefully calibrated in a controlled environment by the manufacturer. The calibration curves were provided as separate files that were downloaded onto the NeoFox Viewer software that was provided with the complete oxygen sensor unit. Three separate oxygen probe and NeoFox units were installed in the facility: one in CV1, one in CV3 and one in CV6 and are shown below in Figure 19

Temperature and pressure data measurements are collected using a National Instruments cDAQ-9137 CompactIDAQ eight-slot controller. The data acquisition system (DAQ) houses an integrated 1.91 GHz quad-core Intel Atom E3845 process, 32 GB nonvolatile hard drive, 2 GB DDR3 RAM and more than 60 sensor-specific I/O modules with signal conditioning. The integrated processing capabilities removes the necessity for connecting the system to an external computer and directs the analog signals directly to the external modules. Thermocouples were connected to an NI 9214 16-channel isothermal terminal block with cold-junction compensation sensors.

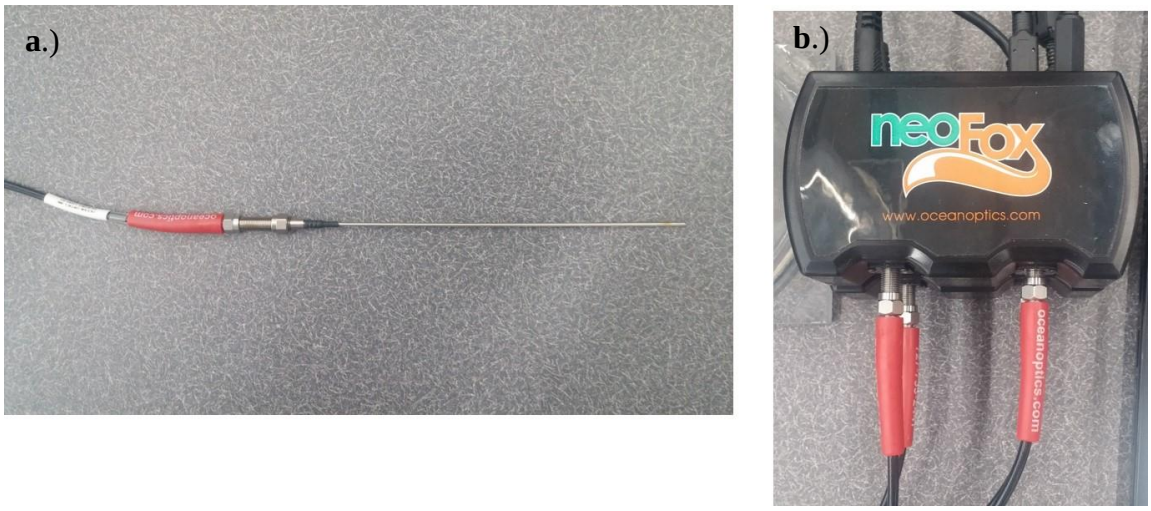

Figure 19. **a.)** Oxygen sensor probe and **b.)** NeoFox fluorimeter.

The module has a sample rate of 68 samples per second with a maximum accuracy of ±1.24˚C. The pressure transducers are connected to an NI 9923 terminal block.

Electro-Flex silicone rubber Heating pads were installed inside of the reactor pressure vessel cylinder in CV1 and are shown in Figure 20. The rubber heating pads have wire-wound heating circuits and are rated for a maximum of 115V and maximum temperature of 232˚C.

To regulate the leak rate in CV1, CV3 and CV6, two stainless steel HAM-LET H300U bonnet needle valves with Let-Lok® tube fittings were installed into the top flange of each test volume as presented in Figure 21. The needle valves have 1/4" NPT threading and a metal bar handling for precise control of the flow rate through the needle valve orifice. From Figure 21, the needle valves have the handles removed to

Figure 20. Silicone rubber heating pads.

prevent the manipulation and accidental contact of the handles that might alter the leak rates from the desired set point.

Figure 21. Needle valve.

III.3 Bypass System

The bypass system shown in Figure 22 was installed to improve the flexibility of the connection between CV1 and CV3 when manipulating the test facility and when changing the test parameters may exclude either or both CV1 and CV3. The small channel and flange on CV1 and CV3 in leak path V13 were removed completely and 1" inch intrusions were drilled into the side panels of CV1 and CV3. The complete bypass system was then installed in the position where the check valve was located. The check valve was integrated into the bypass system and indicated in Figure 22 by the letter "**A**". The check valve is a Swagelok stainless steel poppet check valve with a 1" tube fitting and a cracking pressure, or pressure at which the check valve operates, of 1 psig. The flow through the check valve is one-way and is spring loaded to close the valve once the differential pressure is less than 1 psig, preventing flow reversal or backflow.

Two 1" inch inner diameter ball valves are installed in the bypass system to inhibit flow between CV1 and CV3 in cases where fluid should only flow through the check valve network, straight pipe or should not be in communication. Two 1/4" NPT threaded holes were installed in the bypass system for future installation of instrumentation, particularly a differential pressure transducer to measure the pressure drop through the bypass system because of bends, elbows and friction losses. Currently the holes are sealed with plastic plugs.

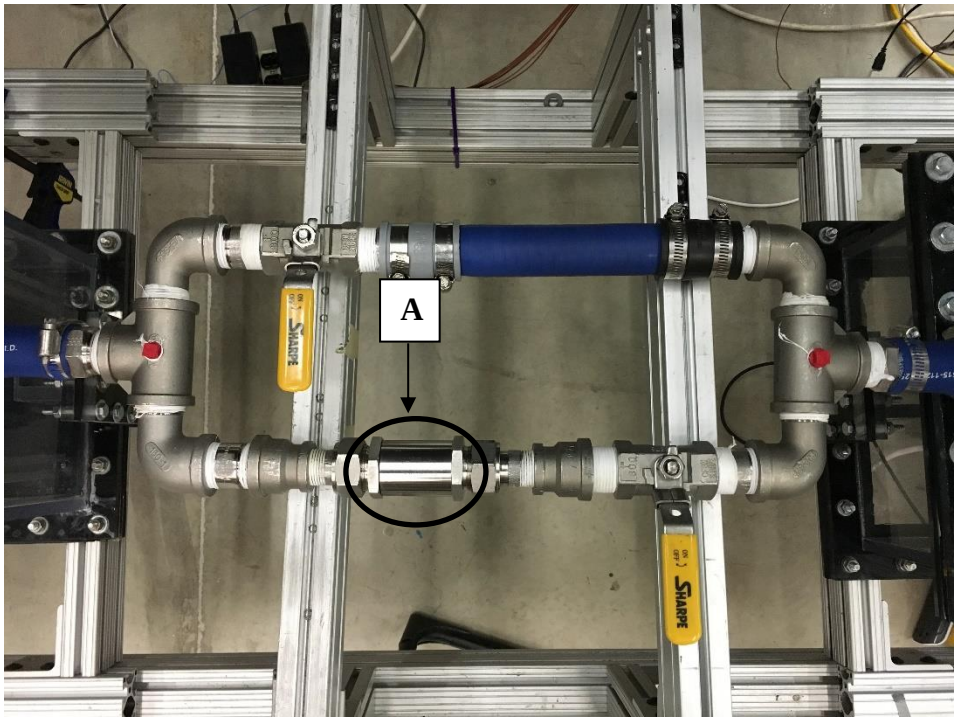

Figure 22. Bypass system with check valve indicated.

III.4 Reactor Pressure Vessel Test Facility Model

The reactor pressure vessel test facility model was manufactured from a 1/16" thick galvanized steel sheet rolled into a cylinder and capped at both ends with steel cylinder caps. The reactor pressure vessel model stands at a height of 34" and an inner diameter of 10.25" for a total volume of 2,805 in^3. The inside of the reactor pressure vessel was lined with three rows of four heating pads as shown in Figure 23 for heating the gas inside of CV1 to a desired temperature and replicate the prototype reactor building conditions during normal operation or accident scenarios. The heating pads were then connected to a Staco Energy Products Co. Model 3PN1010B variable

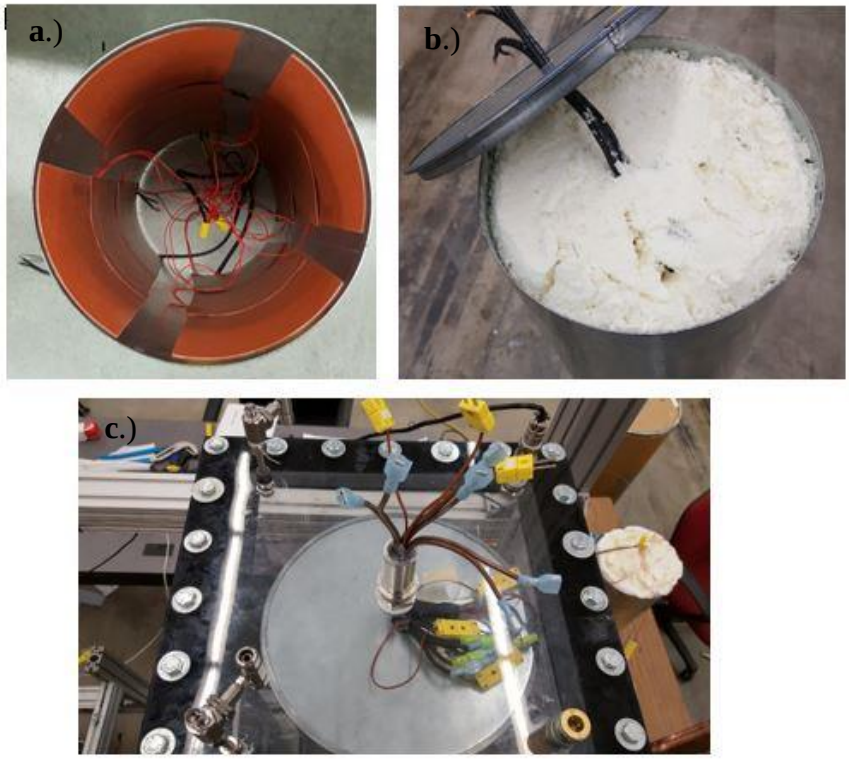

Figure 23. a**.)** Reactor pressure vessel with heating pads, b**.)** reactor pressure vessel with insulating foam and c**.)** CV1 top flange with power line outlet.

transformer for the voltage input. Each set of four heating pads were connected to a variable transformer for a total of three variable transformers and were appropriately labeled “top,” “middle” and “bottom.” The input voltage at each variable transformer are monitored with a Commercial Electric^{TM} MAS830B digital multimeter. Each set of four heating pads is monitored with one k-type thermocouple connected to the data acquisition system. After installation of the heating pads the inside of the reactor pressure vessel was completely filled with Handi-Foam® E84 Class 1(A) polyurethane

foam for insulation and to remove the void that air or helium might otherwise migrate into. A small hole was drilled into the top flange of CV1 and a 1” barbed hose fitting was installed for passing the thermocouple and power lines through as shown in Figure 23. The remaining area inside of the hose fitting was completely sealed with a two-part epoxy.

IV. LITERATURE REVIEW

IV.1 Depressurization Accident Event Progression

Any break in the helium pressure boundary will result in a depressurization accident referred to as a depressurization conduction cooldown event. During normal operation the helium pressure boundary is isolated from the reactor building and contains 100% helium at high pressure, usually 7 MPa. Following a break in the helium pressure boundary, helium will blowdown and rapidly depressurize in the reactor building atmosphere. The louvers vent a significant portion of the helium to the environment until the pressure in the reactor building is reduced to near atmospheric pressure, at which time the louvers close [21]. This results in a mixture of air and helium in the reactor building, and for sufficiently large breaks will activate the reactor building vent path. The accident progression tends to progress in three separate phases: 1.) the blowdown phase, 2.) the air-refill phase and 3.) the air-ingress phase and are each identified in Figure 24 in terms of the reactor building pressure, oxygen concentration and fuel temperature [22]. Although the focus of this study is on the air-refill phase, it is important to introduce the other separate phases and highlight key phenomena that impacts the accident progression.

The blowdown is the initial phase as the result of a penetration in the helium pressure boundary that results in a rapid and accelerated release of pressurized helium into the reactor cavity over time scales ranging from a few seconds to a day or more,

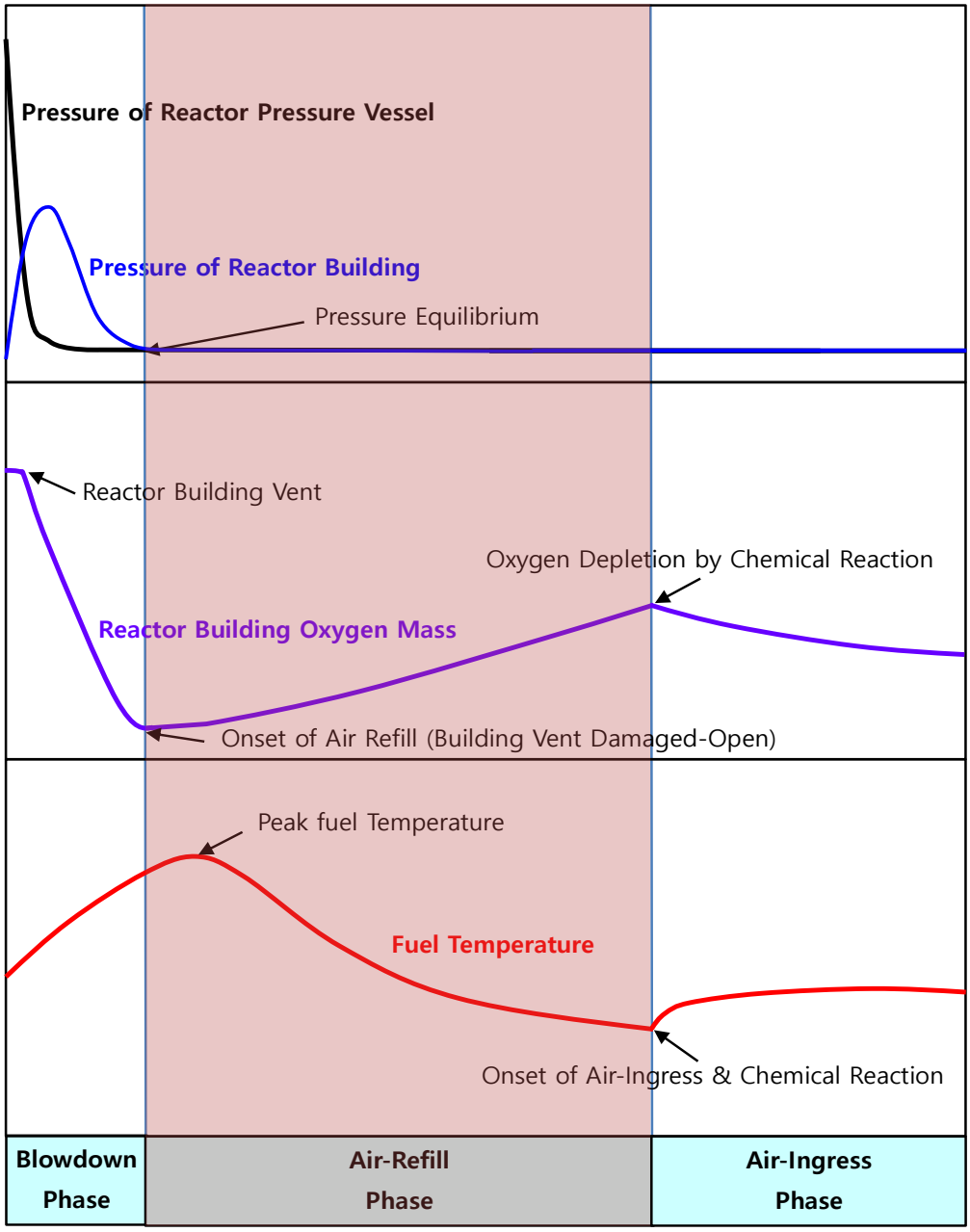

Figure 24. Phase identification of depressurized conduction cooldown event and response of the reactor building pressure, oxygen mass and fuel temperature. The air-refill phase is indicated by the pink region.

depending on the break size. The severity of the initial depressurization and ensuing phenomena is dependent on the break size and location inside of the reactor building. Previous assessments of small-size breaks in the helium pressure boundary resulting from a breakage in an instrumentation or electrical penetration with an area of 0.32 cm^2 showed that the depressurization occurs over about 22 hours. Breaks of this size may not actually supply helium mass/energy to the reactor building atmosphere at a sufficient rate to the active the reactor building vent path. For moderate break flow areas of 78.5 cm^2 that results from a breakage of a 10 cm diameter pressure relief line connected to the top of the steam generator vessel, depressurization occurs over about 5.5 minutes after which the pressure in the helium pressure boundary and reactor building equilibrate at the reactor building vent path set point, typically 1 pressure differential (1 psid).

A more severe event may ensue from the instantaneous double-ended rupture of the cross vessel and cross duct. Pressurized helium is rapidly discharged into the reactor cavity over a time frame of around 3 seconds and provide a pathway for natural circulation through the core [13]. The catastrophic failure of the reactor cross vessel will introduce a break area of 20,430 cm^2 and may lead to an ingress of an air-helium mixture into the reactor pressure vessel. The results from a simplified analytical model have estimated the time for depressurization during a double-ended break of the cross vessel to take 0.4 seconds [23]. Since oxygen chemically reacts with high-temperature graphite, this could result in the damage of in-core graphite structures and fuel, release of carbon monoxide and carbon dioxide, core heat up, failure of the structural integrity of the system, and eventually the release of radionuclides to the environment [23]. An event of

this magnitude is classified as a beyond design basis accident with an estimate event frequency of $4 \cdot 10^{-9}$ per-plant year and is used as a limiting scenario when demonstrating the safety and performance of high temperature gas-cooled reactors [23].

After the postulated break and depressurization phase, the air and helium pressures equalize and air enters the reactor core from the breach due to molecular diffusion and natural convection of a multicomponent gas mixture induced by the distribution of gas temperature and the resulting concentrations in the reactor [23]. The air entering the reactor pressure vessel reacts with high temperature graphite structures and causes a temperature increase of the reactor core and corrosion of graphite components [23]. The air-ingress stage has been the most extensively studied phase of the depressurization accident because of the severity of the damage and potential for radionuclide release from the reactor core to the surrounding environment.

Previous analysis has estimated that the onset of global circulation in the reactor pressure vessel takes on the order of 100 hours to occur, assuming the mechanism is governed by molecular diffusion [23]. However, more recent studies have shown that the air ingress process is dominated by density-driven stratified flow, significantly reducing the time frame for the onset of global natural circulation to around 100 seconds [24]. However, in all analysis the time scale for density-driven flow was several orders of magnitude lower than the time scale for molecular diffusion [15], [23]. Accordingly, comparisons between experiment results revealed by Lowe et. all and a computation fluid dynamics (CFD) simulation showed that the time scale for the onset of density-driven air stratified flow varied between 0.24 seconds and 1.85 seconds for the analytical

and CFD model, respectively. Comparison between the two results showed that the geometry influenced the computed time scales [13]. The geometry from Lowe's experiment was a rectangular channel while the CFD results were obtained in a right circular cylinder with additional pressure and expansion losses from flow resistances due to the supported internal geometry [13]. Therefore, the internal geometry and structure played a significant role in replicating the time scales for the relevant flow dynamics after depressurization.

IV.2 Dynamics of Ideal Gases

An ideal gas is an *imaginary* substance and is defined as a gas whose molecules are spaced far apart so that the behavior of a molecule is not influenced by the presence of other molecules [25]. Real gases have been shown to approximate this behavior when they are at a low pressure or high temperature relative to their critical-point values. Experimental observations have shown that ideal gas obey the simple relationship in Equation (8) called the *ideal-gas equation of state*.

$$P v_s = RT \tag{8}$$

Where P is the characteristic pressure, T is the characteristic temperature, v_s is the specific volume and R is the specific gas constant and is different for each gas. However, for engineering purposes the universal gas constant is often used exclusively in problems

dealing with gases at low pressure or high temperature relative to their critical-point values. When two or more ideal gases are mixed, the behavior of a molecule is normally not influenced by the presence of other similar or dissimilar molecules, and therefore a nonreacting mixture of ideal gases also behaves as an ideal gas [25]. The prediction of ideal gas behavior is often based on either *Dalton's law of additive pressures* or *Amagat's law of additive volumes* and are described by Equation (9) and Equation (10), respectively

$$P_m = \sum_{i=1}^{k} P_i(T_m, V_m) \tag{9}$$

$$V_m = \sum_{i=1}^{k} V_i(T_m, P_m) \tag{10}$$

in these relationships P_i is called the component pressure and V_i is called the component volume [25]. Dalton's law of partial pressures states that the pressure of a gas mixture is equal to the sum of the pressures each gas would exert if it existed alone at the mixture temperature and pressure and, similarly for Amagat's law, the volume of gas mixture is equal to the sum of the volume each gas would occupy if it existed alone at the mixture temperature and pressure [25]. Both Dalton's law and Amagat's law are illustrated below in Figure 25 and Figure 26, respectively, for a mixture of two gases *A* and *B.* These relationships hold exactly for ideal-gas mixtures but only approximately for real

gases due to the intermolecular forces that may be significant for real gases at high densitites [25].

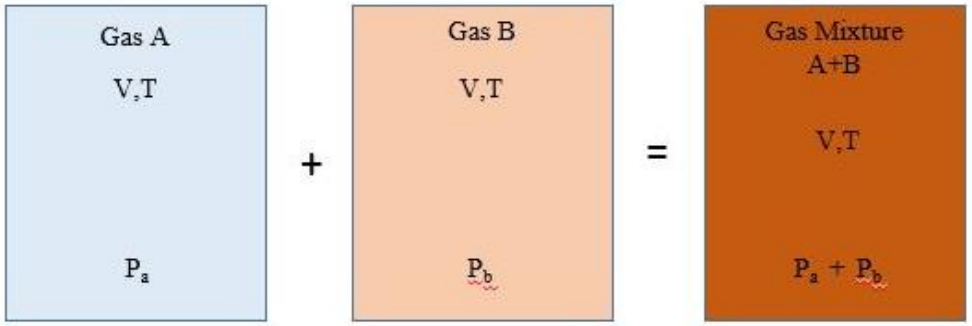

Figure 25. Dalton's law of additive pressures for gas *A* and *B*.

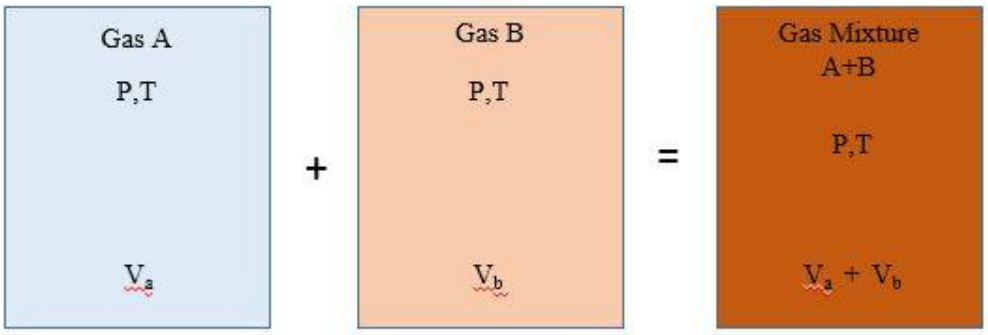

Figure 26. Amagat's law of additive volumes for gas *A* and *B*.

Defining the mole fraction as the ratio of the mole number of a composition to the mole number of the mixture as y_i in Equation (11)

$$y_i = \frac{N_i}{N_m} \tag{11}$$

where the sum of the mole fractions for a mixture is equal to one. A similar relationship is shown in Equation (12) derived for the mass of a component to the mass of the mixture.

$$mf_i = \frac{m_i}{m_m} \tag{12}$$

The mass and mole fractions of a mixture are related by Equation (13)

$$mf_i = \frac{m_i}{m_m} = \frac{N_i M_i}{N_m M_m} = y_i \frac{M_i}{M_m} \tag{13}$$

where M_i is the molar mass of the i_{th} substance and can be expressed as the ratio of the mass of the i_{th} substance to the mole number of the i_{th} substance, $M_i = \frac{m_i}{N_i}$.

A relationship between the partial pressure of the i_{th} gas component and mole fraction can be determined from the ideal-gas relation as follows in Equation (14)

$$\frac{P_i(T_m, V_m)}{P_m} = \frac{N_i R T_m / V_m}{N_m R T_m / V_m} = \frac{N_i}{N_m} = y_i \tag{14}$$

and can be similarly derived for the mass fraction when the ideal-gas assumption is valid [25]. Note that knowledge of the mixture pressure and the partial pressure of each

component in the gas mixture may be employed to determine the corresponding mole fraction in the mixture, either or both spatially and temporally.

The amount of deviation of a real gas from ideal-gas behavior at a given pressure and temperature can be accurately accounted for by the introduction of a correction factor called the compressibility factor Z defined by Equation (15)

$$Z = \frac{P\nu_s}{RT} \tag{15}$$

The compressibility factor can also be expressed as a ratio of the specific volume of the actual gas to the specific volume of the gas for the ideal assumption as shown in Equation (16)

$$Z = \frac{\nu_{actual}}{\nu_{ideal}} \tag{16}$$

where $\nu_{ideal} = \frac{RT}{P}$. For ideal gases the compressibility factor is approximately equal to one. The compressibility factor may be more or less than one as real gas deviates from ideal gas behavior. In general, deviation from ideal gas behavior becomes more significant as the temperature of a substance is decreased or the pressure increased. The amount of deviation from ideal gas behavior can be quantified with respect to the *critical temperature* and *critical pressure* of the gas. The *reduced pressure* and *reduced temperature* is computed from Equation (17) and Equation (18), respectively by

normalizing the given temperature and pressure of a gas with the respective critical temperature and pressure since nearly all gases behave the same when normalized [25]

$$P_R = \frac{P}{P_{cr}} \tag{17}$$

$$T_R = \frac{T}{T_{cr}} \tag{18}$$

where P_R and T_R are the respective reduced pressure and temperature and P_{Cr} and T_{Cr} are the corresponding critical pressure and temperature. According to the *principle of corresponding states* the Z factor for all gases is approximately the same at the same reduced pressure and temperature. A compressibility chart may be used for all gases to determine their deviation from ideal behavior. However general observations show that if the reduced pressure P_R is much less than one and the reduced temperature T_R is greater than 2 then ideal gas behavior may be assumed independent of pressure and temperature [25]. Table 4 lists the critical pressure and temperature of helium and air in MPa and degrees Celsius and Kelvin and the reduced pressure and temperature at standard temperature and pressure for ambient conditions. According to Table 4, for a gas at standard temperature and pressure for ambient conditions (around 100 kPa and

Table 4. Critical and Reduced Pressure and Temperature for Helium and Air at 100 kPa and 25˚C.

	$P_{cr}\ (MPa)$	$T_{cr}\ (°C/K)$	$P_R(MPa)$	$T_R(°C/K)$
Helium	0.23	5.3	0.43	56.25
Air	3.77	132.5	0.03	2.25

298.15 K/25˚C), P_R and T_R were determined from Equation (17) and Equation (18) to be around 0.43 and 56.25 for helium and 0.03 and 2.25 for air. Therefore, any further increases in temperature without a drastic deviation in pressure from the computed values in Table 4 allow for the ideal gas assumption.

For a mixture the compressibility factor can be expressed in terms of the compressibility factors of the individual gases, Z_i by applying Equation (15) to both sides of Equation (33) and simplifying to obtain Equation (19)

$$Z_m = \sum_{i=1}^{k} y_i Z_i \tag{19}$$

However, Equation (19) does not account for the influence of dissimilar molecules on each other and a value predicted by this approach may be considerably different from the experimentally determined value [25]. One way to correct involves the

use of a *pseudocritical pressure* $P'_{cr,m}$ and *pseudocritical temperature* $T'_{cr,m}$ through Equation (20) and Equation (21), respectively, and is known as *Kay's rule* [25]

$$P'_{cr,m} = \sum_{i=1}^{k} y_i P_{cr,i} \tag{20}$$

$$T'_{cr,m} = \sum_{i=1}^{k} y_i T_{cr,i} \tag{21}$$

Results from using Kay's rule to determine the mixture compressibility factor is accurate to within about ten percent over a wide range of temperature and pressures and is suitable for experiments where the ideal gas approximation is valid [25].

The pressure inside of the test facility is assumed to follow an exponential trend described by Equation (22)

$$\frac{dP(t)}{dt} = e^{-\lambda t} \tag{22}$$

where λ is some decay constant characteristic of the controlled experiment conditions with units of s^{-1} and facility geometry and t is the time. The pressure loss in the facility can then be modeled according to Equation (23)

$$P(t) = P_0(1 - e^{-\lambda t}) \tag{23}$$

where for the pressure inside of the facility, P_0 is the initial pressure and $P(t)$ is the final pressure as a function of time. For pressure loss, λ controls how fast the facility loses pressure as a result of leakage. Assuming the ideal gas approximation is valid, from Equation (12) the pressure inside of the facility can be related to the amount of moles of air in the facility for a known temperature according to Equation (24)

$$PV = NRT \tag{24}$$

The volume of the facility and mole number were substituted into Equation (24) from the relationship $\nu = \frac{V}{N}$. Assuming a constant temperature and volume and employing the universal gas constant in terms of moles, Equation (24) can be rearranged to the form shown in Equation (25)

$$P(t) = CN(t) \tag{25}$$

where $C = RT/V$ and can be assumed as a constant for small temperature deviations from the ambient temperature and the value of the universal gas constant R is $8.206 \cdot 10^{-2}$ $L \cdot atm \cdot K^{-1} \cdot mol^{-1}$. To determine the rate of gas leakage from the facility, the number of moles of the gas mixture N_m leaking out of the facility can be determine from Equation (26)

$$N_m(t) = \frac{P_m(t)}{C} \tag{26}$$

where the number of moles and pressure of the gas mixture are evaluated; for a single gas inside of the facility this relationship still holds true. Substituting Equation (23) into Equation (50) and taking the derivative results in Equation (27)

$$\frac{dN_m(t)}{dt} = \frac{1}{C}\frac{d\left(1 - P_0 e^{-\lambda t}\right)}{dt} \tag{27}$$

Resulting in Equation (28)

$$\frac{dN_m(t)}{dt} = \frac{P_0}{C}\lambda e^{-\lambda t} \tag{28}$$

where λ is to be determined experimentally. Substituting $N_m = \frac{m_m}{M_m}$ into Equation (28) results in Equation (29) in terms of rate of loss of mass

$$\frac{dm_m(t)}{dt} = \frac{MP_0}{C}\lambda e^{-\lambda t} \tag{29}$$

The mass flow rate as a function of time can be determined from Equation (29) with knowledge of the initial pressure and the experimentally determined decay constant.

IV.3 Horizontal Buoyant Round Jet

Buoyant jet flows are often described as a fast flowing fluid discharged in an ambient or slow moving reservoir where a density difference exists between the two fluids. High velocity gradients at the interface between the jet and the ambient fluid create instabilities that cause the jet fluid to rotate and induce turbulent vortices that entrain the ambient fluid into the jet [26]. The turbulent motion produces mixing processes and the dissipation of energy from the discharged fluid [26]. All buoyant jets, including horizontal jets can be characterized by three regimes: 1.) *zone of flow establishment*, 2.) *zone of established flow* and 3.) *field zone* [27]. The zone of flow establishment is the region in which the velocity profile transitions to a free turbulent flow and mixing begins with the ambient fluid [27]. The zone of established flow begins when turbulent mixing has reached the center line and the jet dynamics are governed by the jet's momentum and buoyancy and the ambient conditions while the field zone is when the jet momentum has reached zero and the fluid is convected by buoyancy forces and ambient turbulence [27]. In the region where the flow is buoyancy driven the flow starts to rise or fall depending on the relative densities of the two fluids and have a similar Gaussian velocity profile as that in the region of established flow [28]. Discharged flows in the zone of establishment are dominated by the initial momentum flux and independent of the initial angle.

Horizontal jets formed from a round orifice of density ρ_0 is discharged into an ambient fluid of density of ρ_a as shown in Figure 27 as described by J. Xiao et. al [29].

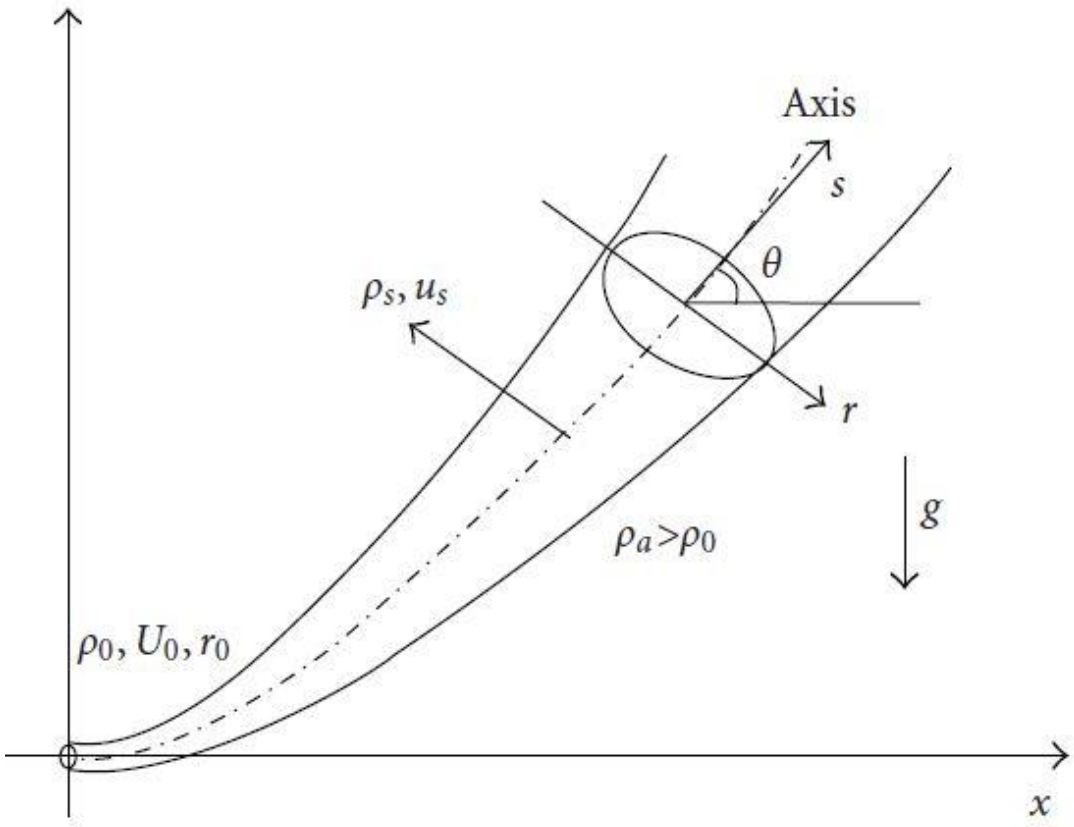

Figure 27. Diagram for horizontal buoyant jet discarged from a round orifice with initial velocity $\boldsymbol{U_0}$ and density $\boldsymbol{\rho_0}$ into a fluid of density $\boldsymbol{\rho_a}$ **[29]**.

The initial density, velocity and radius of the buoyant jet are indicated by ρ_0, U_0 and r_0 respectively. The density of the ambient fluid is assumed to be greater than the density of the intruding jet and the density of entrained jet is signified in Figure 27 by ρ_s and the velocity along the jet is taken to be u_s. The axis of the jet is taken as a parametrical coordinate s, and the coordinate n is taken to be the normal to the axis s [29]. The horizontal buoyant jet can be located along the path coordinates s and n from knowledge of the angle θ and can be found from either Equation (30) and Equation (31) [29], [30]

$$\frac{dx}{ds} = cos\theta \tag{30}$$

$$\frac{dz}{ds} = sin\theta \tag{31}$$

where the Cartesian coordinate z is along the vertical axis.

The initial horizontal jet is assumed to be dominated by momentum and the momentum and buoyancy flux can be defined in Equation (32) and Equation (33), respectively, as follows

$$M = QU_0 \tag{32}$$

$$B = g_0'Q \tag{33}$$

where the term Q is the volumetric flow rate and is defined as $Q = \frac{\pi D^2}{4} U_0$ for a circular orifice and g_0' is the effective gravity term defined as $g_0' = \frac{\rho_a - \rho_0}{\rho_a} g\theta$ [29]. The length scale L_M from the transition of a horizontal buoyant round jet to plume can be computed from Equation (34)

$$L_M = \frac{M^{3/4}}{B^{1/2}} \tag{34}$$

Previous studies have been undertaken for horizontal jets when the Boussinesq approximation is valid and density differences can be ignored in all but the gravitational body force term of the compressible Navier-Stokes equations. For large density differences, however, the Boussinesq approximation is no longer acceptable for accurate engineering calculations and requires modification of the governing equations for the horizontal buoyant jet. Jirka developed an integral model for the conservation of mass, momentum, buoyancy and scalar quantities in a turbulent jet flow that accurately predicts the buoyant jet physics under highly general flow conditions [31]. A more recent study developed a non-Boussinesq integral model for horizontal buoyant jets to obtain numerical solutions in the transition region from jet to plume [29]. The governing equations consist of the compressible mass, momentum, energy and concentration equations but neglect dissipation and turbulent transport in comparison with the mean flow [29]. The velocity profile is assumed to be a Gaussian distribution of the form shown in Equation (35)

$$u = u_s e^{-r^2/w^2} \tag{35}$$

where w is a characteristic jet width [29]. The CFD code GASFLOW was used to validate the non-Boussinesq integral model for large density difference since there was not enough experimental data available [29]. A helium jet at 300 K and 1 bar (14.5 psia) was injected into air at 300 K and 1 bar and an orifice diameter of 0.0845 m [29]. The results of the simulation agreed well with the CFD simulation results except in the zone

of flow establishment where the flow lacks self-similarity and accurately tracked the horizontal buoyant jet trajectory, velocity decay and concentration decay for three separate jets with initial velocities of 10 m/s, 20 m/s and 30 m/s [29].

V. METHODOLOGY AND RESULTS

V.1 Determination of Target Leak Rates

To compare with previously determined results for the simplified HTGR model based on the simplifying assumptions of 20% of the total reactor building leak rate of helium from the top of the reactor cavity, 30% through the top of the steam generator cavity and 50% through the top of the equipment shaft the desired leak rate was scaled down to the test facility. The specified design leak rate was the amount of helium equivalent to the total volume of the prototype facility leaked in one day. The scaling factor for the prototype facility down to the simplified test facility was previously defined as f_{scale} equal to 1/28. To determine the characteristic time of the test facility t_m that would be equal to one day for the prototype facility, t_p, the Reynolds number was preserved as unity as defined in Equation (36)

$$Re_R = \frac{Re_m}{Re_p} = \left(\frac{UL}{\nu}\right)_m \left(\frac{UL}{\nu}\right)_p^{-1} = 1 \tag{36}$$

or rearranging results in Equation (37)

$$\left(\frac{UL}{\nu}\right)_m = \left(\frac{UL}{\nu}\right)_p \tag{37}$$

The ratio of the kinematic viscosity of the test facility model to the prototype facility is defined as $(L_m/L_p)^{3/2}$ from dimensionless number matching. Rearranging Equation (37) and substituting $(L_m/L_p)^{3/2}$ results in Equation (38)

$$\frac{U_m L_m}{U_p L_p} = \left(\frac{L_m}{L_p}\right)^{3/2} \tag{38}$$

Substituting $U_m = L_m/t_p$ results in Equation (39)

$$\frac{L_m^2 t_p}{L_p^2 t_m} = \left(\frac{L_m}{L_p}\right)^{3/2} \tag{39}$$

Cancelling terms by making the previous substitution again results in Equation (40)

$$\frac{t_p}{t_m} = \left(\frac{L_m}{L_p}\right)^{-1/2} \tag{40}$$

and can also be defined by the equivalent statement in Equation (41)

$$\frac{t_p}{\left(\frac{L_m}{L_p}\right)^{-1/2}} = t_m \tag{41}$$

Substituting $L_m/L_p = 1/28$ in Equation (41) results in Equation (42)

$$t_p \cdot \left(\frac{1}{\sqrt{28}}\right) = t_m \tag{42}$$

For the desired time frame of one day, the equivalent time to leak one volume per day in the test facility is equal to around $1.633 \cdot 10^4$ seconds, or roughly 4 ½ hours. The scaled leak rate of one volume per day at a constant rate from the prototype facility was determined by dividing the total volume of the simplified HTGR facility by the scaled time determined by Equation (42). The volume of each chamber in the simplified test facility and the total volume is shown below in Table 5

Table 5. Volume of Individual Compartments in the Simplified HTGR Test Facility

Compartment	Volume (ft^3)
CV1	2.468
CV2	0.645
CV3	2.961
CV4	0.443
CV5	0.643
CV6	2.012
Total	9.536

From the design specifications, at a constant leak rate the total leak rate of helium from the facility equivalent to one volume per day for the prototype facility is equal to 7.31 ft^3. To convert this value to mass the volume was converted to 0.207 m^3 multiplied by the density of air, 1.225 kg/m^3, and resulted in a value of 0.253 kg, or 253.05 g. To get the scaled leakage of one volume per day at a constant rate the computed mass was divided by $1.633 \cdot 10^4$ that produced the desired leak rate as shown in Equation (43)

$$\dot{m} = \frac{253.05g}{1.633 \cdot 10^4\ s} = 0.0155\ \frac{g}{s} \tag{43}$$

where $\dot{m}$ is the mass flow rate in g/s. Finally, the desired leak rate in CV1, CV3 and CV6 through leak paths L1A, L3A and L6A, respectively, were computed and are shown below in Table 6. The volume for CV1 and CV3 in Table 6 does not account for the volume of the reactor pressure vessel and steam generator vessel and is the free volume after the subtracting the volume of the two structures.

Table 6. Total Free Volume of CV1, CV3 and CV6 and Computed Target Leak Rates

Compartment	Volume (m^3)	Target Leak Rate (g/s)
CV1	$6.938 \cdot 10^{-2}$	$3.103 \cdot 10^{-3}$
CV3	$8.042 \cdot 10^{-2}$	$4.655 \cdot 10^{-3}$
CV6	$5.720 \cdot 10^{-2}$	$7.759 \cdot 10^{-3}$

The leak rates computed above in Table 6 were determined, however, assuming a constant leak rate from the facility, which was desired from the design specifications. However, because of the inconsistencies and difficulties with attaining a perfectly constant leak rate even with continuous injection of helium. Therefore, the characteristic leak rate for CV1, CV3 and CV6 were implemented to be the values in Table 6 only at the beginning of each test, or time zero. This desired leak rate was achieved by adjusting the needle valves designated as leak paths L1A, L3A and L6A at the top of CV1, CV3 and CV6.

Before proceeding with the implementation of the desired leak rates the intrinsic leak rates in CV1, CV3 and CV6 were observed by pressurizing each test volume up to around 1.2 psig and allowing the helium to vent from the facility through defects in the facility including at edges were solvent was applied, instrumentation ports, gas injection port at the top of each volume etc. It is noted that the intrinsic leak rates are not by design but are characteristic to the facility based on intrusions that are difficult to completely seal or unattainable leak prevention in other facets of the test volumes. If any sources of leakage were present in the facility that exceeded the desired leak rate by a large margin, then the facility would need to be inspected for large sources of gas expulsion and resealed. The intrinsic leak rates were determined in each volume separately by isolating the one of interest and closing off the flow paths with solid polycarbonate flanges. Air was used as the medium to characterize the intrinsic leak rates. Each intrinsic leak test began by installing all of the instrumentation into the test compartment of interest including thermocouples, oxygen probe and the pressure

transducer. Any purge valves or sources of venting were subsequently closed so that no air could escape through controllable orifices in the compartment. A gas hose connected to a source of ambient air was connected to the top of the facility by a quick-disconnect hose fitting. The pressure and temperature in the compartment were monitored with a LabVIEW program that output the measurements collected by the National Instruments DAQ system. A secondary Noshok® mechanical pressure gauge with a range of 1 to 3 psig was retrofitted to the top of CV1, CV3 and CV6 to have a secondary check on the pressure inside of the test facility. After ensuring that the compartment of interest was leak tight from a qualitative inspection the gas line was open, allowing air to flow into the facility at a pressure of around 15 psig. The gas line also had a male quick-disconnect adapter with a handle for regulating the gas flow. After allowing the air to slowly fill the compartment to 1.2 psig, the line was closed and the gas hose was disconnected from the facility.

The results of the intrinsic leak tests are shown below in Figure 28 for CV1, CV3 and CV6. The intrinsic leak rate tests were conducted with all instrumentation ports sealed with either a measurement device or a 1/4” plastic plug and all purge ports closed. Figure 28 shows the pressure measurement in the three compartments over a time period of around 8100 seconds, roughly half of the computed scaled time to leak one volume per day, or 2 hours and 15 minutes. From Figure 28, CV6 was determined to leak at the slowest rate between CV1, CV3 and CV6 and CV1 leaking at a much faster rate than the other two control volumes. The leak rate of CV3 and CV6 appear to follow

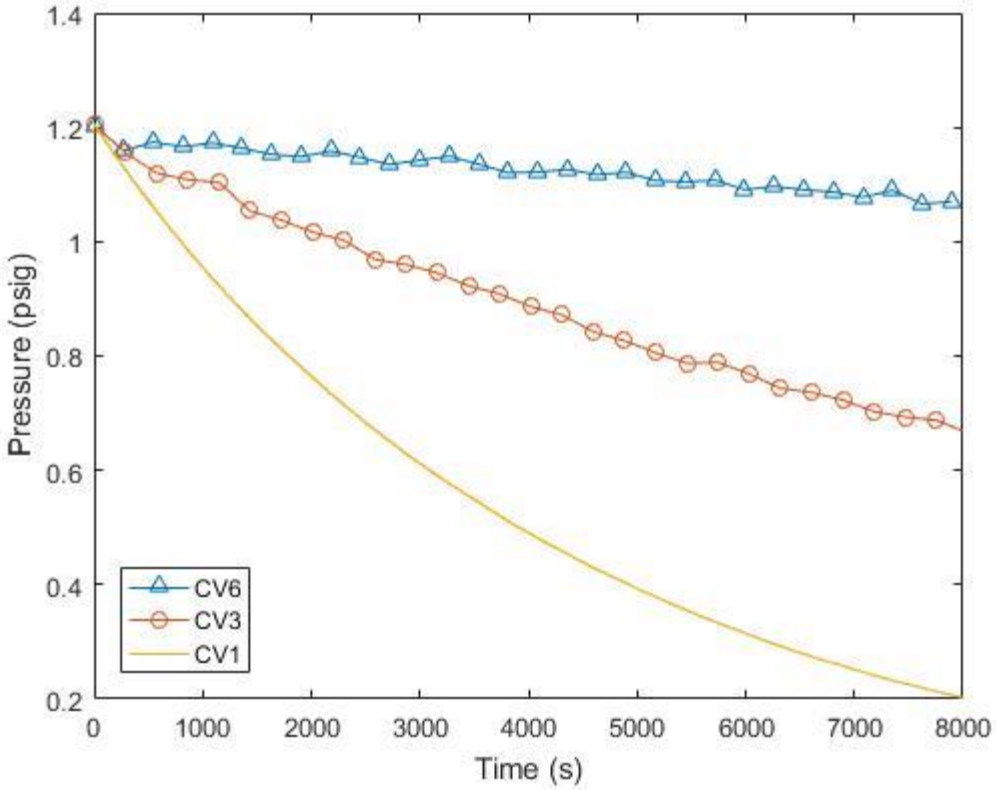

Figure 28. Intrinsic leak rates for CV1, CV3 and CV6 over a time period of 8100 seconds.

a linear trend while CV1 follows an exponential trend as determined previously for ideal gas behavior. Table 7 shows the equation CV1, CV3 and CV6 determined from a curve fit along with the decay constant λ for each compartment. Both an exponential and linear curve fit were created for each characteristic leak profile in Figure 28 and the R^2 value is given for each curve fit to determine the variance from the predicted leak rate profile.

Table 7. Characteristic exponential and linear leak rate curve fit.

Compartment	Curve Fit (Exponential) $Y = Ae^{-bx}$	λ_e (s^{-1})	R^2	Curve Fit (Linear) $Y = Ax + b$	λ_l (s^{-1})	R^2
CV1	$A = 1.197$ $b = 2.230 \cdot 10^{-4}$	$-2.230 \cdot 10^{-4}$	0.9999	$A = -1.164 \cdot 10^{-4}$ $b = 1.146$	$-1.164 \cdot 10^{-4}$	0.9474
CV3	$A = 1.175$ $b = 7.062 \cdot 10^{-5}$	$-7.062 \cdot 10^{-5}$	0.9975	$A = -6.179 \cdot 10^{-5}$ $b = 1.146$	$-6.179 \cdot 10^{-5}$	0.9919
CV6	$A = 1.183$ $b = 1.258 \cdot 10^{-5}$	$-1.258 \cdot 10^{-5}$	0.9466	$A = -1.413 \cdot 10^{-5}$ $b = 1.182$	$-1.413 \cdot 10^{-5}$	0.9475

Table 7 shows that for CV1, an exponential fit to the leak profile in Figure 28 fits the curve almost precisely with an R^2 value of 0.9999 while the R^2 value for a linear fit is around 0.9474. The leak rate profile for CV1 in Figure 28 does appear to follow an exponential trend and matches the theoretical curve as shown in Figure 29. The leak rate profiles in Figure 29 overlap almost completely and agrees with the computed R^2 value in Table 7. The error was computed from the root mean square error shown in Equation (68)

$$u_f(\sigma_T, \sigma_{cv}) = \sqrt{\sigma_T^2 + \sigma_{cv}^2} \tag{68}$$

where σ_T is the uncertainty in the pressure transducers and σ_{cv} is the uncertainty in the curve fit to the experimental data. The pressure transducer error was computed by taking the full-span value of the maximum pressure measurement of the pressure transducer, or 5 psig, and the uncertainty was computed from the root mean square error between the predicted and experimental data with 95% confidence bounds. The pressure transducer uncertainty was determined to be 0.0125 and the root mean square error between the

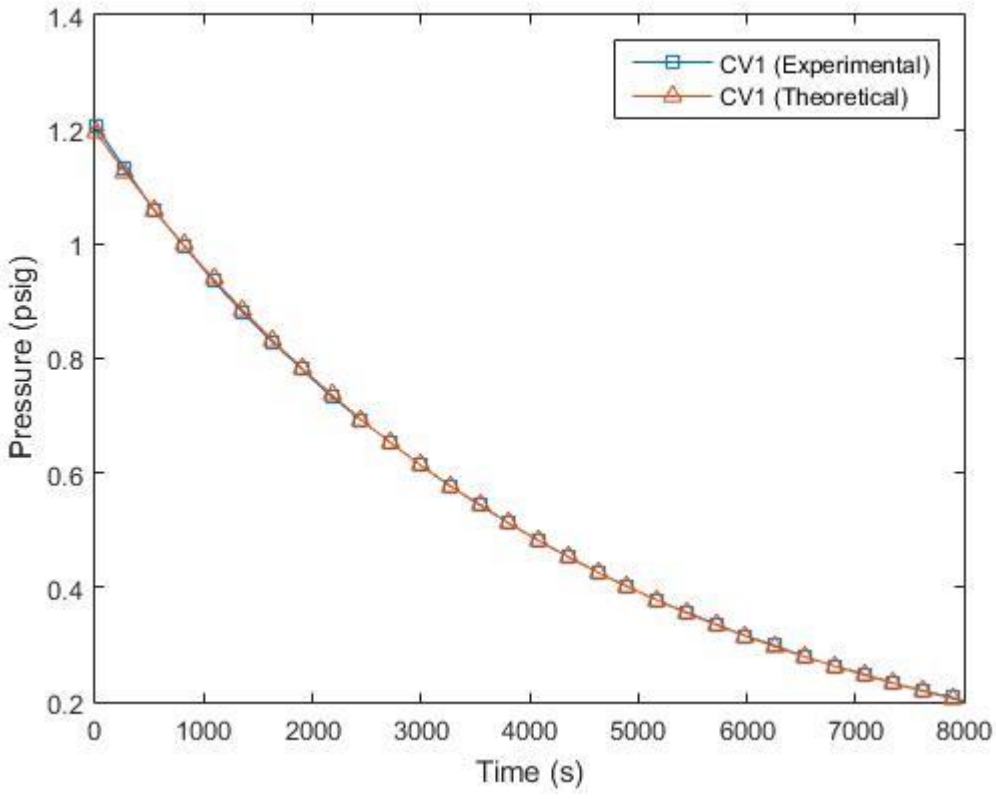

Figure 29. Experimental and theoretical leak rate for CV1.

theory and experimental data was 0.0020 and the resulting root mean square error of the measurements were ±0.0127. For CV3 the exponential curve fit agrees better than the linear fit according to the R^2 values for the two curve fits. However, both R^2 are well within unity and differ by around 0.0056. Observation of Figure 28 shows that the trend of CV3 does appear to be more linear than exponential as proposed in Equation (22) for a theoretical ideal gas. This is more than likely due to the capability of CV3 to contain air inside without leaking a significant portion in the time frame established above. Comparing the two decay constants for the exponential fit, λ_e, from Table 7 CV3 leaks at a rate about 31% less than CV1. Therefore, although the linear fit appears to agree better with the leak rate profile in Figure 28 for CV3, the established time frame for evaluating the intrinsic leak rate was not long enough for CV3 to display the exponential trend for the theoretical model and an exponential fit is still valid for a large span of time scales. On the other hand, the leak rate profile for CV6 agrees better with the linear fit than with the exponential fit from the computed R^2 value in Table 7. Evaluation of Figure 28 shows that the leak rate profile of CV6 appears much flatter with a constant slope compared with the other two compartment's characteristic profiles. The flatter profile lends credibility to the capability of CV6 for containing most of the initial gas present in the facility without leaking a significant portion during the desired experiment time frame. Extending the time scale for evaluating the intrinsic leak rate for each compartment should result in CV6, and correspondingly CV3 displaying the exponential trend similar to that of CV1.

Another point of interest is that to be able to conduct the subsequent tests in the facility the characteristic leak rates must be much lower than the desired leak rates that are established by manipulating the needle valves on the top of CV1, CV3 and CV6. Therefore, a slower leak rate and, accordingly, a flat leak rate profile is desired to ensure that the facility has the flexibility to maintain the target leak rate within a certain tolerance. For instance, if the target leak rate is already a low value, say 90% of the intrinsic leak rate then small perturbations to the test facility that result from cracks, leakage through instrumentation ports or changes to the facility can make it entirely difficult to accurately set the target leak rate or even make the target set points achievable. Nonetheless, as will be seen the intrinsic leak rates were well below the target leak rates and did not hinder achieving the target leak rate.

The signals for the pressure in CV3 and CV6 in Figure 28 are noisier than the signal for the pressure measurement in CV1 and fluctuate much more frequently. The reason for the signal fluctuations was because the National Instruments 9923 terminal block that the pressure transducers are connected to have a separate grounding that must be connected to a shielded grounding, such as the one provided on the front of the NI DAQ system. Because this shielded grounding was not initially utilized extraneous signals from the building's common grounding disturbed the millivolt to voltage output of the pressure transducers and resulted in the noisy signals shown above. This issue was later resolved and the signal outputs were then the smooth signals as seen in Figure 28 for the pressure in CV1. Unfortunately, this was resolved after the initial leak rates were obtained from the pressure measurements in CV3 and CV6. However, confidence in the

pressure signals dictated that the intrinsic leak rates did not need to be reacquired for CV3 and CV6.

To ensure repeatability and consistency in the measurements the intrinsic leak rates tests were conducted on two separate days to account for small changes in ambient conditions such as barometric pressure, temperature and relative humidity. For one select case, the intrinsic leak rate inside of CV6, determined from the measured pressure of air inside of the compartment, is displayed in Figure 30. Again, because of

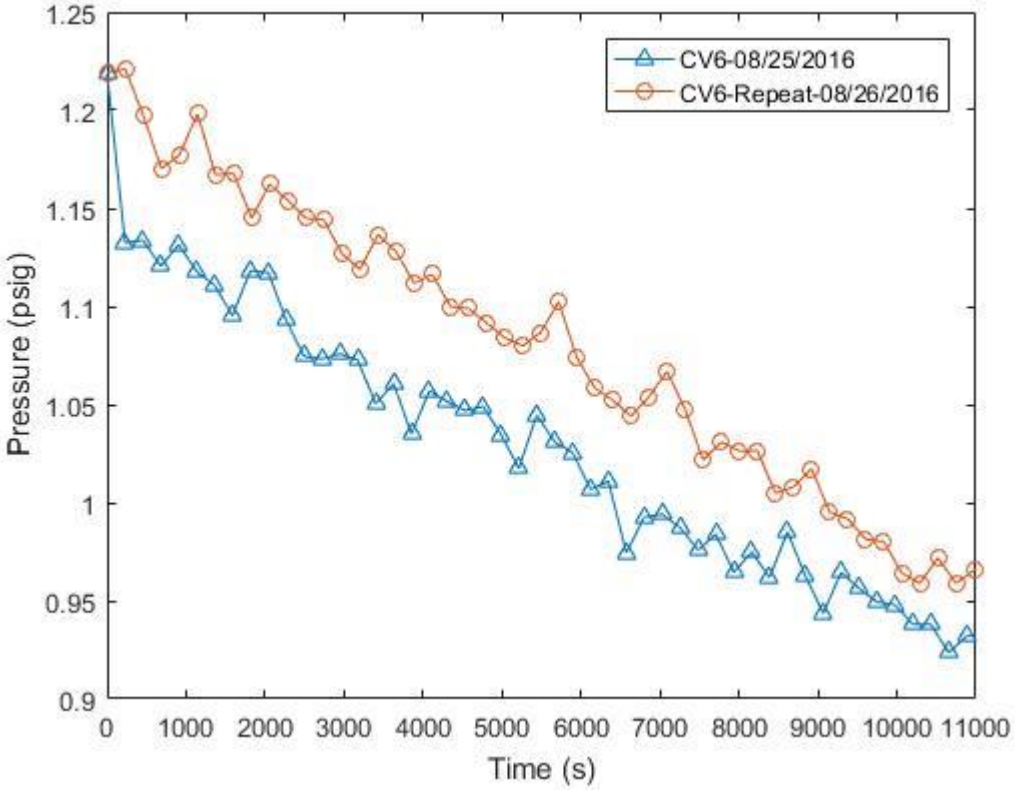

Figure 30. Intrinsic leak rate inside of CV6 conducted three separate times for repeatability benchmarking.

the unresolved grounding issue the signals appear noisy, but confidence in the pressure output allowed for the acceptance of the pressure curves as indicative of the actual trend in the leak rate with values fluctuating around the true pressure. Three separate sets of pressure data were collected inside of CV6. The first set of data was collected with the same set of initial conditions and instrumentation and were obtained within one day of each other. The time frame for collecting pressure data inside of CV6 was determined arbitrarily and there was no specific day or set of days that was deemed more or less suitable. Since it was determined experimentally that an exponential fit could accurately predict the trend of the pressure loss inside of the test facility, Table 8 shows the decay constant, λ_e, for CV6 computed only from a best fit exponential curve. The corresponding R^2 value was also computed for each intrinsic leak rate test and is also given below in Table 8.

The two pressure, or leak rate, profiles all display a relative linear trend over the 11,800 second time frame. All the measurements were collected starting at a pressure close to 1.2 psig and continuously monitored. The two repeated tests in Figure 30 approximately display the same behavior but were separated by a value of 0.05 psig. Beginning at around 10,000 seconds the two leak (pressure) profiles begin to overlap at the same values. However, the pressure at the beginning of the first repeated test quickly drops from the desired starting pressure of 1.2 psig down to 1.14 psig in around 35 seconds while the first test and second repeated test leak at a constant, linear rate throughout the duration of the experiments. This could be attributed to a number of trivial issues such as leaving the hose connected to the facility after injecting the air

Table 8. Characteristic exponential and linear leak rate curve fit for repeatability experiments inside of CV6.

CV6 Trial	Curve Fit (Exponential) $Y = Ae^{-bx}$	λ_e (s^{-1})	R^2
08/25/2016	A = 1.138 $b = 1.894 \cdot 10^{-5}$	$-1.894 \cdot 10^{-5}$	0.9709
08/26/2016	A = 1.21 $b = 2.035 \cdot 10^{-5}$	$-2.035 \cdot 10^{-5}$	0.9802

since the quick-disconnect fittings have been shown to leak a significant amount of gas, which typically use acrylonitrile-butadiene rubber (NBR) internal O-rings and a spring loaded sleeve to allow for the flow of gas into the system through the gas line. Typical wear from constant use or deformation of the spring loaded sleeve can allow for a small or significant amount of fluid loss through the quick-disconnect fitting or damage to the locking elements of the coupling from pressure spikes inside of the test facility. Other sources of sudden gas loss can be through instrument ports or small deformations in the bonded surfaces of the facility. The first leak rate test and the first repeated test overlap at the beginning but almost immediately with the second repeated test having a higher leak rate. This could be from the same sources of extraneous gas leakage as the first leak rate test or manipulation of the instrumentation installed in CV6 between tests. Small

changes in the facility or test procedure such as from not disconnecting the air hose at the exact desired pressure can alter the characteristic leak rate of CV6.

Nonetheless, Table 8 shows that the exponential curve matches the first leak rate test and the second leak rate test with R^2 values close 0.98 and roughly matches the first leak rate test with an R^2 value of 0.9709. The deviation in the predicted curve and actual trend is attributed to the sudden drop in the pressure at the beginning of the test that deviates from exponential behavior and the computed error from Equation (44) was ±0.0205. Figure 31 shows the experimental data of the first test with the theoretical model plotted for comparison. The comparison between the theoretical and experimental curves show a large deviation at the beginning of the measurements and at the end where a large spike in the pressure occurs. This sudden peak in the pressure measurement was not accounted for because the facility was allowed to leak gas without interference and was not continuously monitored over the almost 4 hour time period. The deviations at the beginning and middle contribute to the somewhat lower R^2 value compared with the other two tests. The values of the decay constant fell between $-1.896 \cdot 10^{-5}$ and $-1.893 \cdot 10^{-5}$ within 95% confidence bounds while for the last test 95% of the measurements were almost exactly the value shown above in Table 8 and were between $-2.036 \cdot 10^{-5}$ and $-2.033 \cdot 10^{-5}$ for the prescribed confidence bounds.

Overall, the leak rate constant λ_e for each test in CV6 within a relative degree of accuracy despite some deviations in the pressure loss behavior. A comparison between

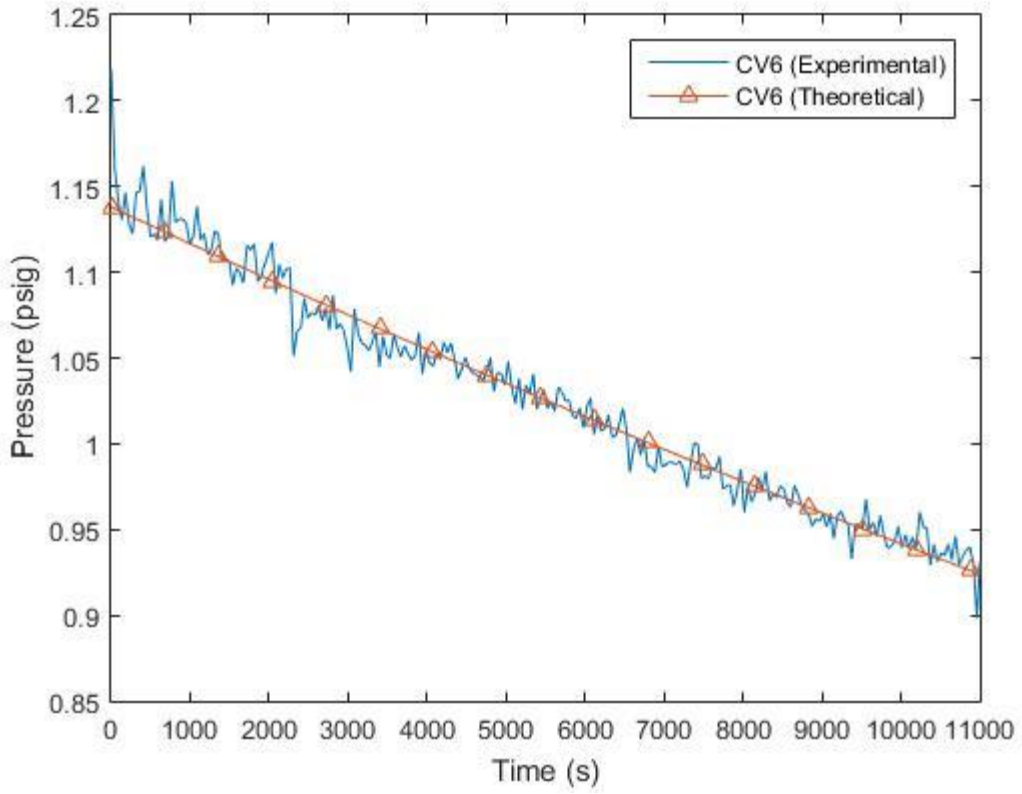

Figure 31. Experimental and theoretical leak rate for CV1.

any two leak constants and the percent deviation can be determined from Equation (69)

$$\%_{difference} = \frac{|\dot{\lambda_{e1}} - \lambda_{e2}|}{\frac{\lambda_{e1} + \lambda_{e2}}{2}} \cdot 100\% \tag{69}$$

The percent error between each of the three leak rate constants λ_e were computed and are displayed in Table 9. The computed errors show the difference between the first test and the repeated test at around 7.177% and is apparent from Figure 30 by the steepness

Table 9. Percent error for the CV6 repeatability tests.

λ_{e1}, λ_{e2} (s^{-1})	$\%_{difference}$
08/25/2016, 08/26/2016	7.177

of the two slopes and magnitude between corresponding pressure measurements. The small difference between the pressure (leak test) measurements from the two repeated tests is verified by the similarity in the slope of the pressure trend between the measurements and is not necessarily influenced by the difference in the pressure magnitude measurements for a corresponding point in time. Nevertheless, the largest difference is less than an order of magnitude between the two separate leak tests and the amount of air leaked from CV6 should remain consistent and stable.

After establishing repeatability and stability in the intrinsic leak rate of CV1, CV3 and CV6 the target leak rates were established inside of the three compartments separately. The design specific target leak rates defined in Table 6, however, assume a constant leak rate over time from the prototype facility as opposed to the exponential leak rates from ideal gas behavior. The prototype facility reference achieved a constant leak rate by assuming the same amount of gas is exactly injected into the facility as is leaked from the facility, resulting in a square leak rate profile as opposed to the leak rate behavior previously observed for the intrinsic leak rate tests. Therefore, the design parameters were modified to only match the target leak rate at time zero from knowledge of the mass flow rate of gas from compartments CV1, CV3 and CV6. From Equation

(29), knowledge of the parameters at time zero allows for determination of the leak rate. Rearranging Equation (29) results in Equation (46)

$$\frac{C}{P_0 M}\frac{dm_m(t)}{dt} = \lambda e^{-\lambda t} \tag{46}$$

where C was assumed to be relatively constant and defined as $C = RT/V$. The mass flow rate were determined previously from the target leak rate in each compartment and M is the molecular mass of the gas in question. For air, M is approximately 29 g·mol^{-1}. Substituting time t equal to zero results in Equation (47)

$$\frac{C}{P_0 M}\frac{dm_m(t=0)}{dt} = \lambda_{target} \tag{47}$$

The exponential term equals one when the time equals zero. Setting the initial pressure P_0 equal to 1.2 psig, the universal gas law R to 8.31446·10^{-2} J ·K^{-1}·mol^{-1} and the initial temperature to 22.13˚C, roughly atmospheric temperature the characteristic leak rate constant can be computed for some volume determined from the geometry of each compartment. Table 10 gives the computed target leak rate constant values at time zero from the prototype design specifications and values given in Table 6.

Table 10. Target leak rate values inside the scaled test facility at time zero for CV1, CV3 and CV6.

Compartment	λ_{target} (s^{-1})
CV1	0.00055
CV3	0.00071
CV6	0.00167

The values for λ_{target} computed above are the target leak rate constants for each of the compartments dependent on the design criteria, but the mass flow rates desired are only valid at time zero. The tests performed on the facility do not utilize a constant injection of gas into the facility, resulting in the exponential trend in the pressure described previously for the intrinsic leak rates. The target leak rate constants in Table 10 were calculated assuming that air was the only gas present inside of the facility with the error dependent on the actual temperature inside of each compartment and how much it deviated from 22.13˚C, which are in turn dependent on the error of the thermocouple measurements. Typical thermocouple measurement errors at low temperature ranges are around ±2.2%, and therefore, for a gas that is only pressurized to 1.2 psig the change in temperature should be negligible. Assuming a constant specific heat relation for air, which are nearly constant at temperatures near atmospheric, the isentropic relation between temperature and pressure at two separate instances of ideal gas can be realized by Equation (48) [25]

$$\left(\frac{T_2}{T_1}\right) = \left(\frac{P_2}{P_1}\right)^{\frac{(k-1)}{k}} \tag{48}$$

which is derived from Gibbs equation assuming negligible heat or work input and k is the ratio of specific heats. For air, k is equal to 1.40 at low temperatures. From Equation (48), for an initial pressure P_1 equal to ambient pressure, P_2 equal to 1.2 psig and a final temperature T_2 equal to 22.13˚C the initial temperature T_1 is approximately 21.640 ˚C, and as a result the temperature difference is only negligible from the experiment initial and final pressures. This agrees with average temperature measurements that were collected for various leak tests at 1.2 psig and fall within the range of accuracy of the thermocouples. As a result, the values calculated in Table 10 were used without any significant motives to doubt the validity of the leak rate constants.

To ensure that the intrinsic leak rates did not exceed and were much lower than the target leak rates, the computed λ_{target} and λ_e for CV1, CV3 and CV6 are compared below in Table 11. Equation (49) was used to find the ratio between the two leak rate constants as a percentage and are given in Table 11 by $\lambda_{\%}$

$$\lambda_{\%} = \frac{\lambda_e}{\lambda_{target}} \cdot 100\% \tag{49}$$

The relative magnitude of the ratios between the intrinsic and target leak rate for CV1, CV3 and CV6 vary significantly. For CV6 the intrinsic leak rate is less than one

Table 11. Comparison between intrinsic and target leak rate constants in CV1, CV3 and CV6.

Compartment	λ_{target} (s^{-1})	λ_e (s^{-1})	$\lambda_{\%}$ (%)
CV1	0.00055	$2.230 \cdot 10^{-4}$	40.55
CV3	0.00071	$7.062 \cdot 10^{-5}$	9.95
CV6	0.00167	$1.258 \cdot 10^{-5}$	0.75

percent of the target leak rate and leaves flexibility in future modifications or natural void formation in the solvent from constant pressurization and depressurization of the compartment. Also, manipulation of the needle valves to achieve the target leak rate is made easier by the relatively low gas leakage from CV6 relative to the desired gas leakage. For CV1 the intrinsic leak rate is nearly half that of the target leak rate leaves little room for error when manipulating instruments inside of CV1 or adjustment of the needle valve situated on top of the volume. The relative difference in the leak rate constants is also a function of the amount of gas desired to leak from each compartment, with the most amount coming from CV6 and the least amount of CV1. The design specification requires the least amount of gas to come from CV1 because of the position of the most critical components of the HTGR system where the most harmful substances reside including radionuclides produced during fission. Conversely, the entirety of the test facility was manufactured from polycarbonate and maintain the same physical features and geometry. To conserve the target leak rate more attention and care was

given to CV1 because of the restriction on the amount of gas that is allowed to leak from the compartment. The intrinsic leak rate of CV3 is around 10% and in a moderate range where immediate changes to the instrumentation configuration should not have a huge impact on the ability to readily achieve the target leak rate.

The target leak rates for CV1, CV3 and CV6 were each determined individually by isolating the compartment of interest from the remainder of the test facility and pressurizing the compartment to around 1.2 psig and manually adjusting the needle valve situated on top of each control volume, designated as leak path L1A, L3A and L6A for CV1, CV3 and CV6 respectively. After adjusting the needle valve arbitrarily, the compartment of interest was allowed to vent air through the open needle valve for 5 minutes and the pressure continuously monitored. Prior to testing the target leak rate constant computed analytically was used to determine the theoretical pressure remaining in the test facility after 5 minutes from Equation (23), where the initial pressure P_0 is equal to 1.2 psig and the time t equal to 300 seconds. Resolving the final pressure, $P(t)$, after 5 minutes allows for a comparison when experimentally determining the approximate needle valve orifice size to achieve the target leak rate. After 5 minutes, if the pressure has not reached or overshot the desired pressure the facility was pressurized again and the needle valve adjusted until a new characteristic leak rate is achieved. This was repeated until the pressure inside of the compartment after 5 minutes was approximately the same as the analytically determined final pressure. Extrapolating the curve provides the leak rate profile beyond 5 minutes. The selection of 5 minutes was to expedite constant testing if the target leak rate was not achieved for a particular needle

valve orifice size, and furthermore, the behavior of leak rate, or pressure decay, of the air inside of the facility for a short time period after time zero displays approximately linear behavior. After achieving the desired leak rate of air from the facility the procedure was repeated multiple time to ensure repeatability and stability in the pressure measurements.

Figure 32 shows the target leak rate plots from CV3 determined experimentally along with the theoretical leak rate profile for an initial pressure of 1.2

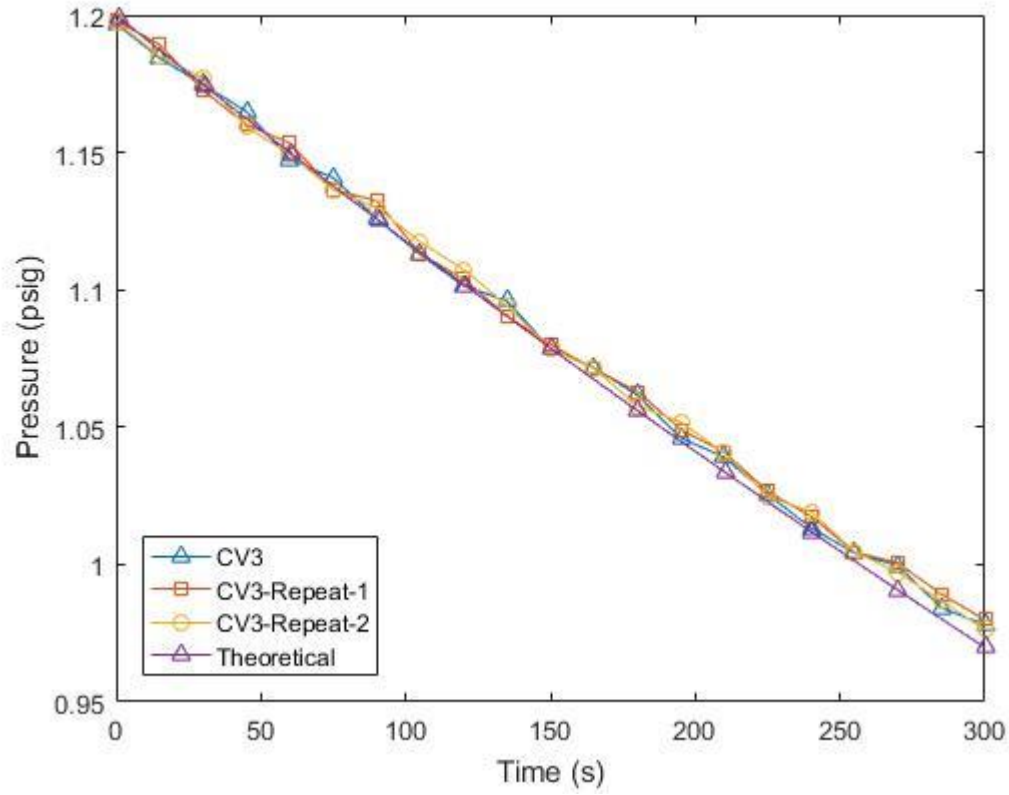

Figure 32. Target leak rate plots for CV3 compared against the theoretical profile.

psig over 300 seconds, or 5 minutes. The target leak rate experiment was repeated three consecutive times to ensure repeatability in the results. Obviously the pressure decay profile for the three separate trials in Figure 32 are almost exactly aligned, indicating repeatability in the process and stability of CV3 in maintaining the same leak rate during future testing. Table 12 shows the characteristic equation determined from an exponential curve fit and target leak rate decay constant $\lambda_{target,exp}$ for the three separate leak rate trials. The percent difference of the experimentally determined target leak decay constant $\lambda_{target,exp}$ and the analytically computed target leak rate decay constant from Table 9 is also shown in Table 12 and calculated from Equation (50)

$$\%_{difference} = \left| \frac{\lambda_{target} - \lambda_{target,exp}}{\lambda_{target}} \right| \cdot 100\% \tag{50}$$

where the percent difference is defined differently from Equation (45). The resulting exponential decay constants in Table 12 agree with the results in Figure 32 for the three separate leak test experiments in CV3, namely that the pressure decay (leak rate) profiles almost exactly match the theoretically predicted leak rate profile for the analytically computed decay constant. The R^2 value for all three curves are above 0.998 and are nearly unity, indicating once again that the needle valves were adjusted to a high degree of precision and the facility leaks air at a rate nearly identical to the analytically

Table 12. Characteristic exponential and linear leak rate curve fit for CV3.

Trial	Curve Fit (Exponential) $Y = Ae^{-bx}$	λ_e (s^{-1})	R^2	$\%_{difference}$
CV3	A = 1.197 b = 0.0006817	-0.0006817	0.9984	3.98
CV3-Repeat-1	A = 1.199 b = 0.0006839	-0.0006839	0.9985	3.67
CV3-Repeat-2	A = 1.199 b = 0.0006882	-0.0006882	0.9986	3.07

calculated leak rate constant and corresponding pressure decay profile. The percent difference between all three trials are under 4%, where CV3-Repeat-2 shows the lowest difference from the analytically derived leak rate decay constant but differs from the other two trials by less a percentage point. All three trials are well within the range of each other and precisely follow the analytical pressure decay curve shown in Figure 32. The experimentally determined leak rate constant λ_e for a 95% confidence bound was between -0.0006817 and -0.0006814 for the first trial, differing by less than 10^{-6} and a root mean square error of ±0.0025 psig. For the first repeat the experimentally determined leak rate constant λ_e for a 95% confidence bound was between -0.0006842 and -0.0006837 and between -0.0006885 and -0.0006879 for the last repeat bounded by

a 95% confidence interval. The root mean square error of the last two repeats was also ±0.0025 psig.

Figure 33 shows the target leak rate plots from CV6 for three separate repeats of the target leak rate test determined experimentally along with the theoretical leak rate profile for an initial pressure of 1.2 psig over a 300 second duration. The results of the plot show that the three separate trials follow the theoretical pressure decay curve approximately but oscillate more frequently, most likely from the extraneous noise in the system that was not corrected at the time of the target leak rate characterization inside of

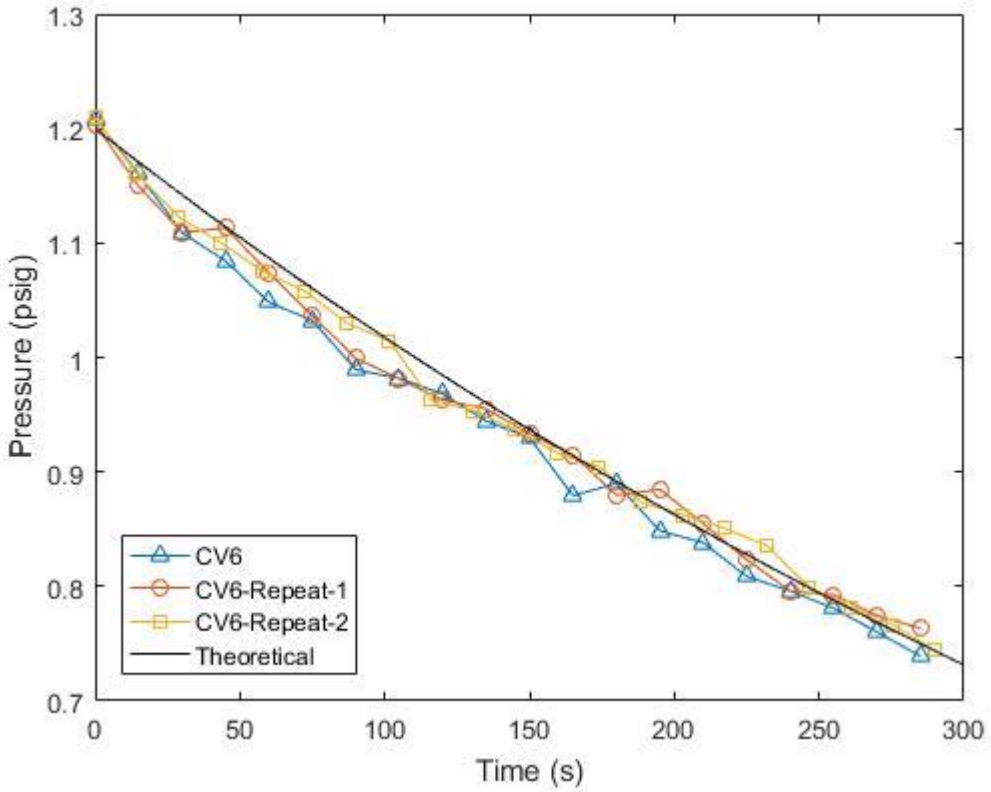

Figure 33. Target leak rate plots for CV6 compared against the theoretical profile.

CV6. Table 13 shows the characteristic equation determined from an exponential curve fit and target leak rate decay constant $\lambda_{target,exp}$ for the three separate leak rate trials and the percent difference from the analytically computed target leak rate coefficient.

Again, the results of the three separate trials agree well with the theoretically estimated leak rate decay constant with all of the R^2 values above 0.995. The first trial, designated CV6, has the largest R^2 value, almost unity. However, from Figure 33 the curve appears to reside the farthest away from the theoretical pressure decay profile. The agreement of the trial with the analytically determined pressure decay profile could be

Table 13. Characteristic exponential and linear leak rate curve fit for CV6.

Trial	Curve Fit (Exponential) $Y = Ae^{-bx}$	λ_e (s^{-1})	R^2	$\%_{difference}$
CV6	A = 1.168 b = 0.001607	-0.001607	0.9921	3.77
CV6-Repeat-1	A = 1.174 b = 0.00153	-0.00153	0.9950	8.38
CV6-Repeat-2	A = 1.184 b = 0.001573	-0.0006882	0.9956	5.81

from the overall shape of the curve following the same trend as the analytical profile compared with the other two trials. Also, significant noise is present in the signals that could actually produce further errors as the separate trials oscillate around the analytically fitted curve. The first repeated trial has the lowest R^2 value and diverges significantly at the tail end of the pressure decay profile above where the hump in the signal is present. The percent difference between the analytically computed leak rate constant is also largest for the first repeated trial, CV6-Repeat-1, and is indicative of the lower coefficient of determination. The second trial is only slightly improved in terms of accuracy with a difference of 5.81% and an R^2 0.9956 but appears to follow the analytically computed curve more closely compared with the other two trials. The presence of noise, however, might actually have perturbed the results and produced oscillations in the signal greater in magnitude than the other two trials that served to move the signal further away from the analytical pressure trend.

The experimentally determined leak rate constant λ_e for a 95% confidence bound was between -0.001609 and -0.001606 for the first trial with a root mean square error of ±0.0115 psig. For the first repeat the coefficient with 95% confidence bounds were between -0.001531 and -0.001529 and between -0.001574 and -0.001572 for both of the repeated trials. All three trials display about the same precision for the estimated range in which the decay constant is expected to reside. The root mean square for the first repeated is ±0.0088 psig and ±0.0083 psig for the second repeat. The root mean square error for the two repeated trials are about 75% of the root mean square error for the first trial, indicating that there is more agreement between the computed and experimental

values compared with the first trial. This is revealed from Figure 33 where the two repeated trials follow the analytically computed pressure decay profile compared with the first trial, and accordingly, there is more overlap of the final two tests with the analytical curve.

The target leak rate test was conducted inside of CV1 and repeated 4 times over a time frame of 300 seconds to ensure reliability in the pressure decay rate since the intrinsic leak rate is only around half of the desired target leak rate. The results of the target leak tests for 5 separate trials is shown in Figure 34 and compared with the

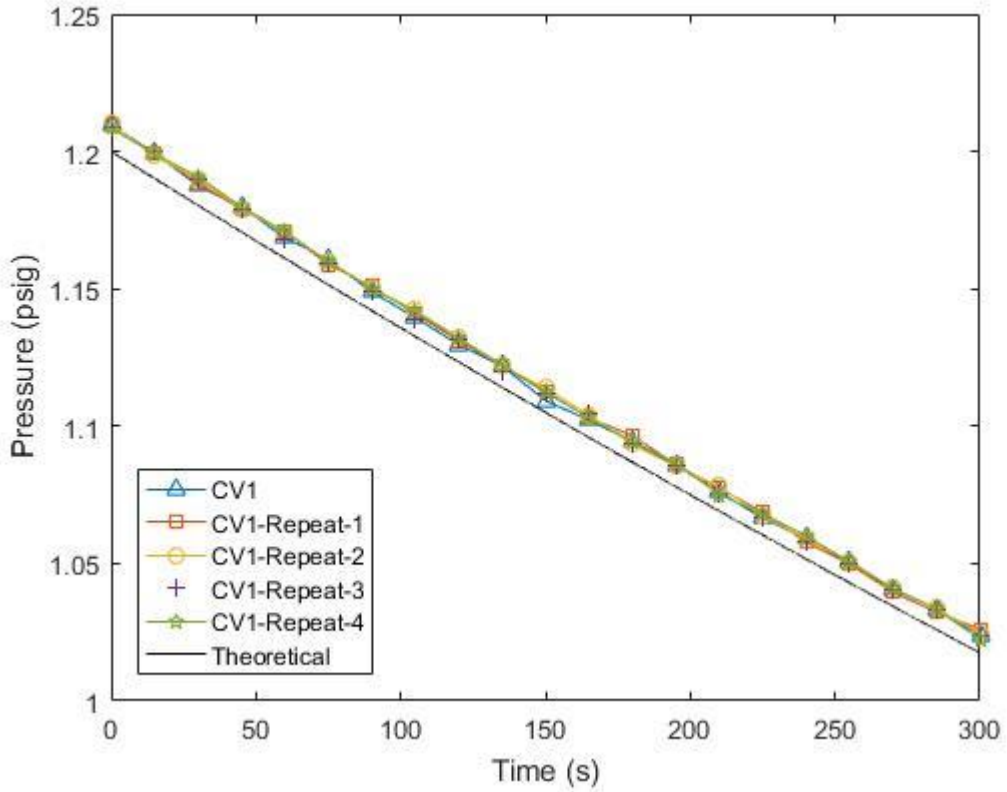

Figure 34. Target leak rate plots for CV1 compared against the theoretical profile.

theoretically determined pressure decay profile. The results show significant repeatability in the target leak rate tests for all 5 trials and precisely follow the analytical pressure decay curve behavior. The reason for the curves not overlapping is simply because the initial pressure measurements were collected at a slightly higher value than 1.2 psig, closer to 1.209 psig, but the difference is negligible and the leak rate decay profiles obtained are consistent with the analytical solution. Table 14 shows the characteristic equation determined from an exponential curve fit and target leak rate decay constant $\lambda_{target,exp}$ for the 5 separate leak rate trials and the percent difference from the analytically computed target leak rate coefficient. All 5 trials agree with the analytical pressure decay profile, as indicated by all of the R^2 values close to unity. The proximity of experimentally determined target leak rate constant to the desired target leak rate constant, as previously mentioned, for all 5 trials is 0.9996, which may indicate some round-off error when computing the R^2 since all of the experimental decay constants λ_e are the same as the target decay constant λ_{target} to 5 decimal places. Furthermore, the percent difference for the four repeated trials is less than a percentage point while being close to one for the first trial. All 5 trials in Figure 34 and display of similarity to the analytical model, and therefore, are consistent with the results presented in Table 14.

The experimentally determined leak rate constant λ_e for a 95% confidence bound was between -0.0005563 and -0.0005559 for the first trial with a root mean square error of ±0.0011 psig. For the second trial the coefficient was bounded in a 95% confidence interval between -0.0005524 and -0.0005521 with a root mean square error between the

Table 14. Characteristic exponential and linear leak rate curve fit for CV1.

Trial	Curve Fit (Exponential) $Y = Ae^{-bx}$	λ_e (s^{-1})	R^2	$\%_{difference}$
CV1	A = 1.209 b = 0.0005561	-0. 0005561	0.9996	1.11
CV1-Repeat-1	A = 1.209 b = 0.0005523	-0.0005523	0.9996	0.42
CV1-Repeat-2	A = 1.209 b = 0.0005536	-0.0005536	0.9996	0.65
CV1-Repeat-3	A = 1.209 b = 0.0005547	-0.0005547	0.9996	0.85
CV1-Repeat-4	A = 1.209 b = 0.0005528	-0.0005528	0.9996	0.51

analytical and experimental solution of ±0.0011 psig. For the third, fourth and fifth trial the coefficients were bounded in a 95% confidence interval between -0.0005538 and -0.0005535 for trial three, -0.0005548 and -0.0005545 for trial four and -0.000553 and -0.0005526 for the fifth trial. The root mean square errors were ±0.0010 psig, ±0.0011 psig, ±0.0011 psig and ±0.0011 psig for the third, fourth and fifth trial respectively. Again, round-off error may have contributed to the likeness in the statistical uncertainty

computations but overall the 5 separate trials agree, to a high degree of accuracy, with the desired analytical target leak rate curve and corresponding decay constant, as indicated in Figure 34 by the sameness of the pressure decay plots.

V.2 Combined Leak Rate Test Inside of CV3 and CV6 with Rapid Depressurization

One of the first tests performed after establishing the target leak rate was to evaluate the leakage of helium from CV3 and CV6 through flow path V34 and V45 and the two needle valves designated L3A and L6A. The two compartments were connected at flow path V36 and isolated from the rest of the facility by installing polycarbonate flanges connecting CV1 and CV3. The test was conducted by installing a polycarbonate flange at the outlet of CV5 that was connected by a long nylon rope as shown below in Figure 35. CV3 and CV6 were then purged of air by injecting helium at a constant rate into CV3 and opening the ball valve opposite of the check valve in the bypass system to provide a venting path for the heavier fluid through CV1. The helium regulator was adjusted to 15 psig at the outlet. While injecting helium and purging CV3 and CV6 of air the pressure was consistently monitored to ensure that the compartments were not over pressurized. The oxygen concentration in CV3 and CV6 were also monitored by each of the oxygen probes installed in CV3 and CV6 respectively since the desired initial oxygen concentration requirement for each compartment was zero or approximately zero, and corresponding filled with helium only. Once the oxygen probes had saturated at an acceptable concentration, the ball valve connected in the bypass

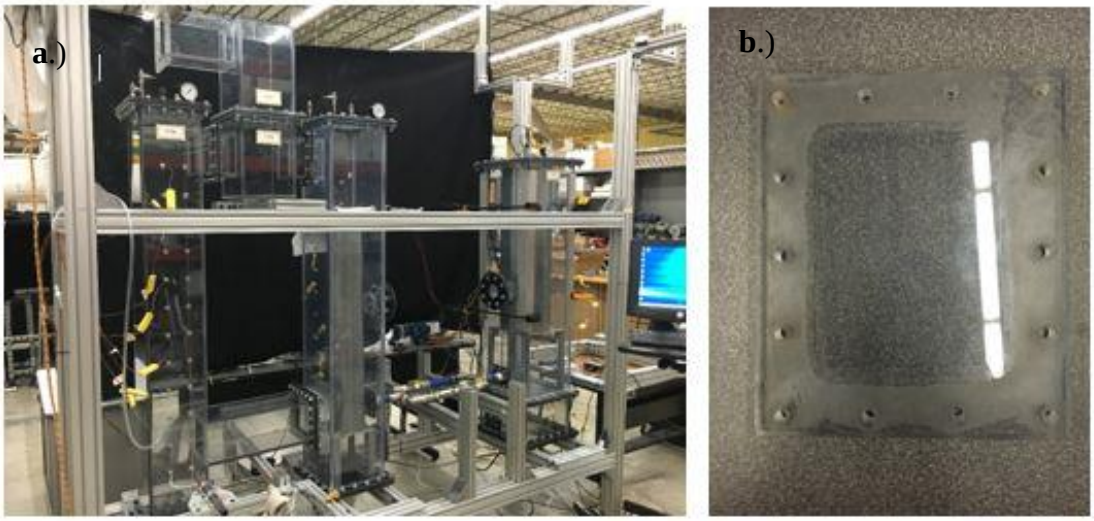

Figure 35. **a.)** Test facility setup for helium leak test through CV3 and CV6 and **b.)** polycarbonate flange/door.

system was closed, isolating CV6 from CV3, and helium was continuously injected into the facility through the top of CV3 until the facility was pressurized to around 1.2 psig. After achieving the desired pressure, the injection was stopped and the helium injection line was disconnected from CV3. Previous experience with using the oxygen probes showed that any concentration that reads below 1% for an extended period of time and saturates on a particular value for two to three minutes is an acceptable criterion for establishing close to 100% helium inside of the test facility.

After disconnecting the helium line from CV3 the pressure inside of the compartment was further monitored until it reached approximately 1 psig. Once the desired pressure inside of CV3 was attained the polycarbonate flange was manually operated by quickly releasing four Irwin 4-1/4” deep throat bar clamps from each corner

of the polycarbonate flange while simultaneously pulling on the door with the nylon rope connected to the door. This sudden opening of the door resulted in a rapid depressurization as indicated below in Figure 36. The pressure in Figure 36 is plotted for both CV3 and CV6 over a 5 minute time interval. The facility rapidly depressurizes, as indicated in Figure 36 by the steep drop in the pressure profile of CV3 and CV6, and both compartments depressurize at the same moment.

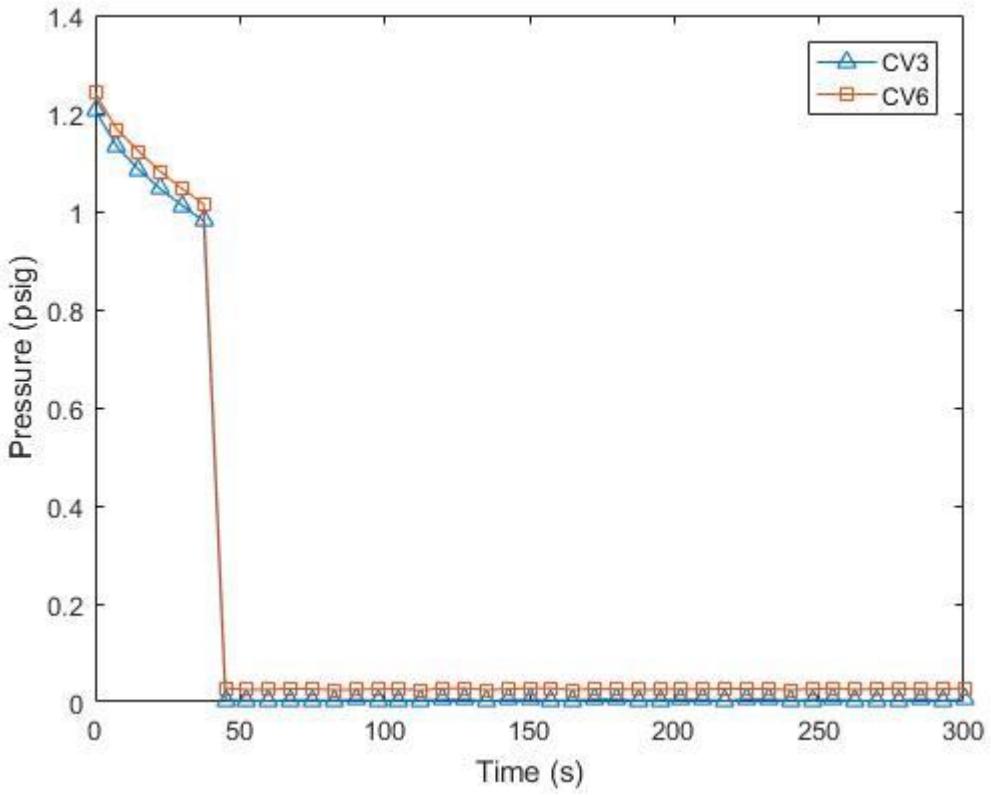

Figure 36. Leak rate plots for CV3 and CV6 during rapid depressurization at 1 psig.

The reason for the slightly higher pressure in CV6 at the moment that the facility was depressurized was that only the pressure in CV3 was monitored to determine when to manually operate the polycarbonate flange and induce a rapid depressurization in CV3 and CV6. Furthermore, the intrinsic leak rate of CV6 is about 1/6 of that in CV3, leading to a higher retention of helium inside of CV6 for the short time period before the facility was discharged of helium.

From the plots of the depressurization inside of CV3 and CV6, after the initial drop the pressure remains relatively constant for about a tenth of a second before again decreasing again to ambient pressure. The sudden stability in the pressure could have been caused by human error by allowing the door to block the flow path since the speed of the fluid is, most likely, not high enough to develop compression or Taylor waves that bring the flow to rest by isentropic expansion and a drop in the downstream pressure. Additionally, for a shock to occur the flow much change from subsonic to supersonic [32].

A deeper understanding of the flow dynamics after the depressurization can be acquired from an analysis of the helium (oxygen) concentration measurements inside of CV3 and CV6. Figure 37 show the CV3 and CV6 oxygen concentration as a function of time during the depressurization for a duration of around 22 minutes. The results of the oxygen concentration measurements in Figure 37 show that, after the initial depressurization at 1 psig, air rapidly begins to refill CV3 and CV6 and after about 10 minutes has approximately reached the saturation concentration, or ambient concentrations, of the oxygen sensors. The dynamics of the refilling period appear to be

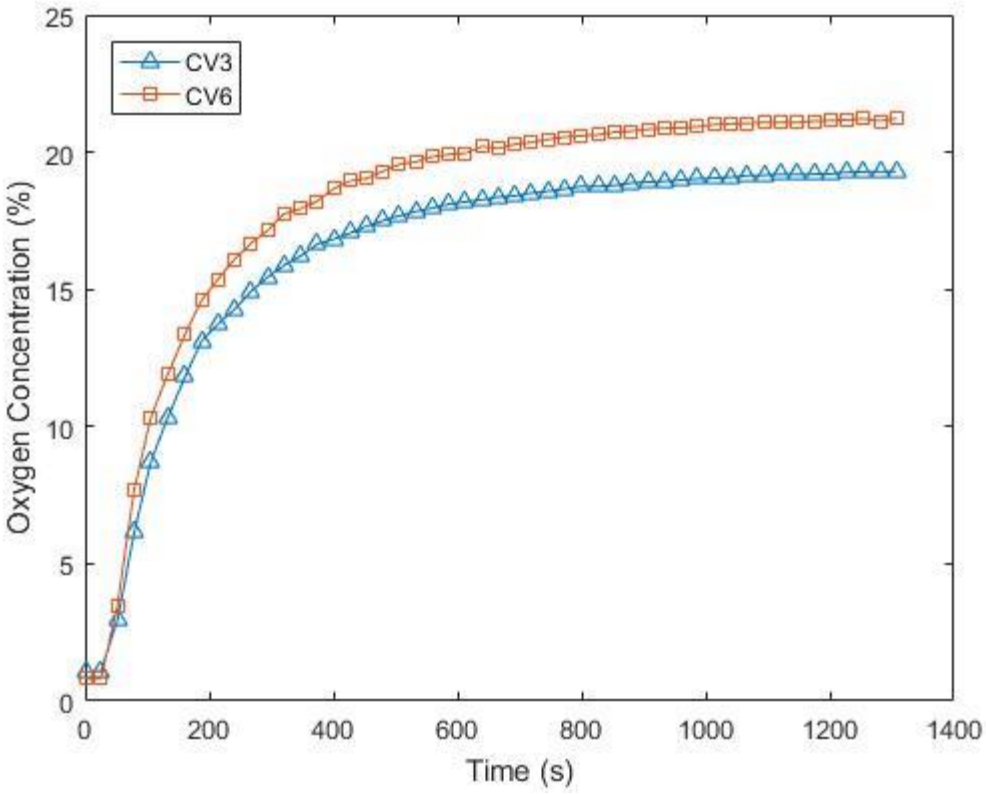

Figure 37. CV3 and CV6 oxygen concentration after depressurization.

dominated mainly by inertia throughout the initial depressurization up to around 2 minutes where the slope of the oxygen concentration profiles is steep and non-zero. The flow is then dominated mainly by diffusion due to concentration gradients from around 8 minutes up to the end of observation.

For the test two oxygen probes were used: one located at the bottom of CV3 and the other inside of CV6 located at the bottom of the compartment. The oxygen probe inside of CV3 was located near the center of the inlet to flow path V36 and is indicated in Figure 38 by the green circle around the instrument port where it was installed. The

oxygen probe was located in close proximity to the steam generator vessel and installed about one inch into the compartment through a 1/4” bored through compression fitting. The other oxygen probe was installed inside of CV6 in the bottom instrumentation port as indicated in Figure 39 by the green circle.

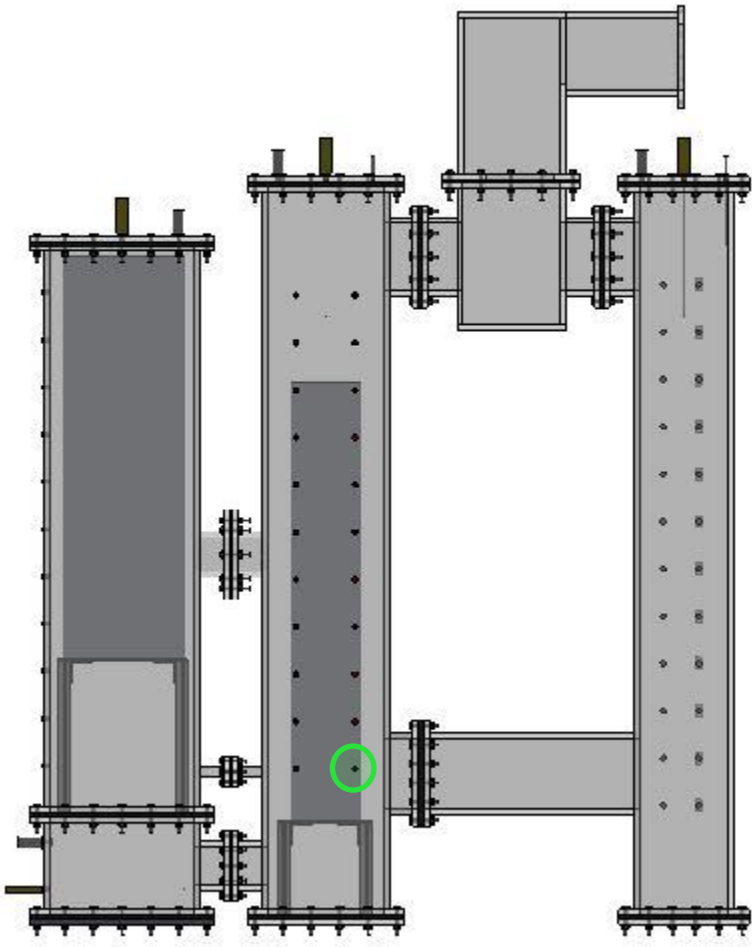

Figure 38. Simplified HTGR test facility with location of oxygen sensor indicated.

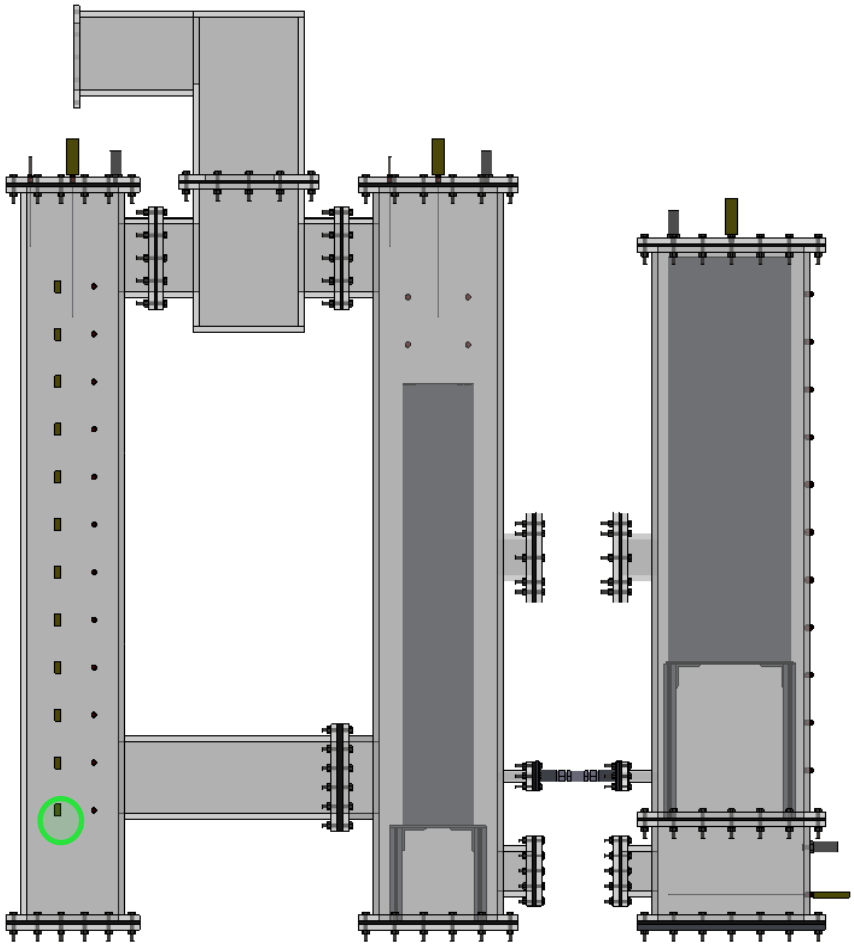

Figure 39. Simplified HTGR test facility with location of oxygen sensor indicated.

The locations of each oxygen sensor were strategically located to accurately capture the flow dynamics at pivotal locations during the depressurization and subsequent air refill of CV3 and CV6.

During the inertial phase of the depressurization the helium and air are driven by a gravity current driven by the density difference between the two gases. This flow regime has been investigated through numerous studies and is described as a lighter fluid

propagating at constant speed along the upper surface of the bounding region into the heavier fluid while the heavier fluid travels in the opposite direction along the lower bounding region also at a constant speed [33]. Yih proposed that the two gravity currents should travel at the same speed and the depth of each current should be half of the channel height [34]. However, this was considered only for the Boussinesq case where the fluids only have slightly different densities. However, the density of helium is roughly a seventh of the density of air and the Boussinesq approximation is no longer considered valid. Lowe et. al found that for non-Boussinesq flows, the heavy current propagates faster than the light current and conservation of volume requires that the interface depth is not the same [33]. Therefore, the pressure inside of CV3 and CV6 could have been increased slightly due to the heavier air intruding faster into the facility than helium exiting, which may have resulted in the sudden flat pressure profile at around 40 seconds described previously inside CV3 and CV6 from Figure 36. Simpson described the difference in the helium and air front where the upper front of the helium is smooth while denser air front has a raised head and following billows that develop from instabilities at the interface [35]. This phenomenon was described in a review by Reyes et al. on the progression of air ingress after a postulated loss of forced cooling accident inside of a HTGR reactor pressure vessel, where the lock-exchange phenomena occurred but was further driven by a temperature gradient as a result of the hot helium escaping from the core [15]. For the current experiment instabilities may still develop at the exit of CV5 where the two fluids are initially exchanged or in flow path V36 where

the long channel may allow the air and helium to stratify. This may induce further mixing of the fluids but further complicate the flow dynamics.

Figure 40 shows the oxygen concentration inside of CV3 shortly before the and directly after the immediate depressurization. After purging both test volumes of oxygen with helium until the oxygen probes detected a concentration close to zero, the volumes were further pressurized to around 1.2 psig, shown previously in Figure 36. Once the volumes were purged and pressurized the facility was allowed to leak helium slowly through the needle valves situated on top of CV3 and CV6 until the pressure

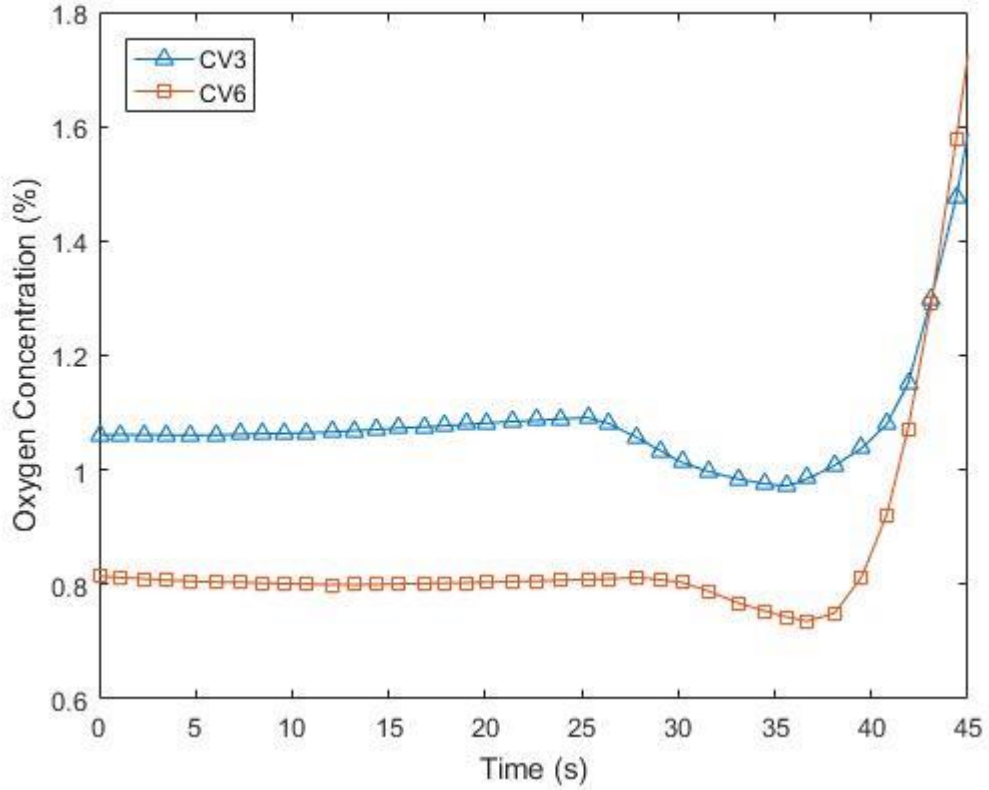

Figure 40. Oxygen concentration inside CV3 and CV6 before and immediately after initial depressurization.

inside of CV3 and CV6 were both close to 1 psig. The facility was then rapidly relieved of helium by ejecting the polycarbonate flange on the outside of CV5 and allowed to refill with oxygen. From Figure 40 the time from when the facility was pressurized to 1.2 psig to the initial depressurization was around 35.1 seconds, indicated by the minimum concentration value for CV3. Because flow path V64 was closed with an aluminum flange, the inflow of air and exhaustion of helium from the facility was only through CV3 to the ambient environment. Therefore, as expected the oxygen probe in CV3 responded first to the change in the gas concentration after depressurization. The minimum oxygen concentration occurred at around 11.4 seconds inside of CV6 after the first peak. As a result, by taking the time difference between the oxygen probe responses a rough estimate of the time for air to traverse through CV3 to CV6 may be determined. The time for the oxygen probes to respond, or for the air to move from CV3, through flow path V36 to CV6 was around 1.1 seconds. The distance between the two oxygen probes was 30.5" (0.7747 m). Taking the characteristic distance between the two oxygen probes and dividing by the time, the velocity of the gravity current through flow path V36 was computed to be 2.31 $ft \cdot s^{-1}$ (0.704 $m \cdot s^{-1}$).

Figure 41 shows the refill phase of the depressurization from 45 seconds after the initial pressurization to 1.2 psig to around 2 minutes. The oxygen concentration profiles of CV3 and CV6, determined from the oxygen probes at their designated positions, appears to follow a linear trend. From a fitted regression curve to each oxygen concentration profile, the R^2 value for a linear fit to the CV3 profile was 0.9810 with a root mean squared error in the concentration of ±0.4135. The R^2 value for a linear curve

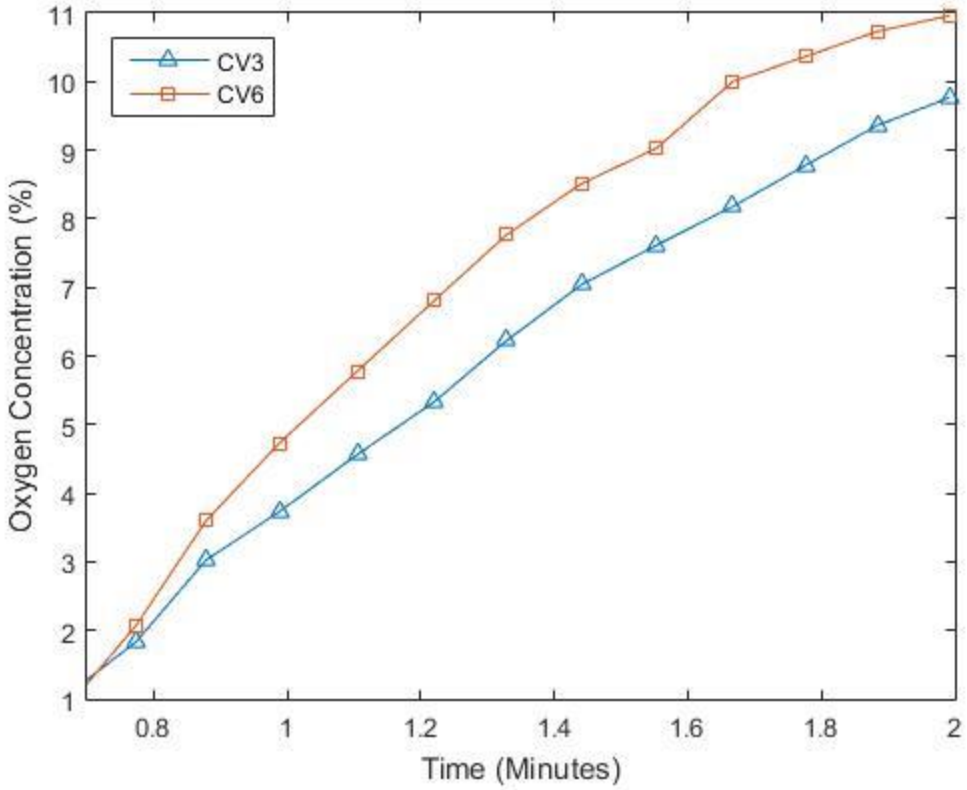

Figure 41. Oxygen concentration inside CV3 and CV6 30 seconds after the initial pressurization to 2 minutes after the initial pressurization.

slightly less to the CV6 oxygen concentration profile with a root mean squared error in the concentration of ±0.7540. CV3, therefore, exhibits a much more linear trend in the air refill during the first few moments after depressurization. Some subtleties that may have skewed the goodness of the fit may have been from the error in the oxygen probes themselves, which depend on the measured pressure from the internal pressure transducers or inconsistencies in the thermoprobes for measuring the appropriate gas temperature.

As an aside, the oxygen sensors in CV3 and CV6 each have a different base concentration reading that slightly deviates from an ambient concentration reading, usually around 20.9% at standard temperature and pressure and is the reason for the gap between the steady state concentration readings. This deviation in the baseline reading can be attributed to the internal pressure transducer or external temperature transducer having a slight offset from the actual experimental pressure and temperature or an error in the fluorescence decay and the corresponding response to the partial pressure of oxygen and temperature. The oxygen sensors are factory calibrated and come with a certificate of calibration for the applicable oxygen concentration ranges. The oxygen probes may be recalibrated internally from a two-point calibration described by Equation (5), but requires precise knowledge of the fluorescence decay constant τ_0 at some known condition and was not recommended by the manufacturer. The oxygen probes also use a special coating applied to the tip of the probes that absorb oxygen and quench the emitted light. If the end of the probe is damaged or the coating removed in any increment, the oxygen probe settings may also be disturbed. However, the response was consistent throughout the duration of the experiments involving the oxygen probes.

V.3 Rapid Depressurization Through Hinged Louvre

The depressurization through a hinged louvre located between CV4 and CV6 through flow path V64 was evaluated. The hinged louvre was constructed of a polycarbonate material, similar to that of the test facility, and attached using hinges to a

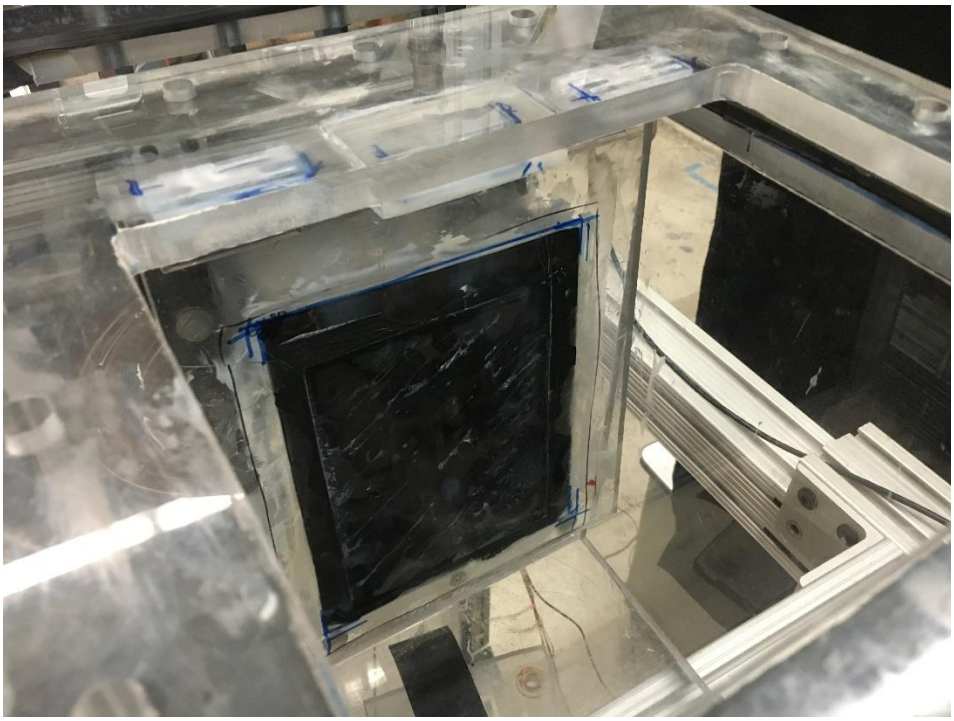

Figure 42. Hinged louvre located between CV4 and CV6.

polycarbonate flange that was placed between CV4 and CV5 as shown below in Figure 42. The hinges were glued to the polycarbonate flange and the louvre was glued to the hinges and a piece of gasket material with similar dimensions as that of flow path V34 and V64 was also glued to the louvre.

Figure 42 shows the louvre through the top of CV4 where CV5 would usually be situated. The gasket material was used to seal flow path V64 and prevent gas leakage during the pressurization stages of the experiment and coated with Molykote® 111 to increase adhesion of the gasket to the polycarbonate wall of CV4.

For this set of tests, again, only CV3 and CV6 were in operation with CV1 and CV2 isolated from the designated test volumes through the use of polycarbonate flange caps. Leak paths L3A and L6A were also in operation and allowed gas to escape during pressurization and testing and flow path V36 allowed for communication between CV3 and CV6. For this test, flow path V34 was closed through the use of the aluminum flange placed between CV3 and CV4. Therefore, flow path V64 was the only pathway for gas to both enter and leave the test facility after the hinged louvre opened. The desired operating pressure was 1 psig, and correspondingly, the hinged louvre should open when the pressure inside of CV3 and CV6 exceeded 1 psig. This was achieved through the use of neodymium magnets that were strategically placed along the bottom edge of the hinged louvre. One magnet was placed at the bottom between CV4 and the hinged louvre while the opposing pole magnet was placed outside of CV4 and directly facing the magnet inside of the test facility. The target cracking pressure of the hinged louvre was attained through the strategic placement of the neodymium magnets and trial and error until a configuration was found that achieved an operating pressure of 1 psig. Once a candidate configuration was found the trial and error testing was repeated multiple times to ensure repeatability and precision of the hinged louvre to open at the desired operating pressure.

Three oxygen probes were used instead of two for the previous set of leak tests. Two of the oxygen probes were located inside of CV6; one was located at the very top next to the exit at flow path V64 and the other at the bottom near the center of flow path V36. The remaining oxygen probe was located at the bottom of CV3 and parallel to the

center of flow path CV3 and the bottom oxygen probe in CV6. The final configuration of oxygen probes inside of CV3 and CV6 are shown in Figure 43 and Figure 44, respectively along with the position of the hinged louvre and aluminum flange.

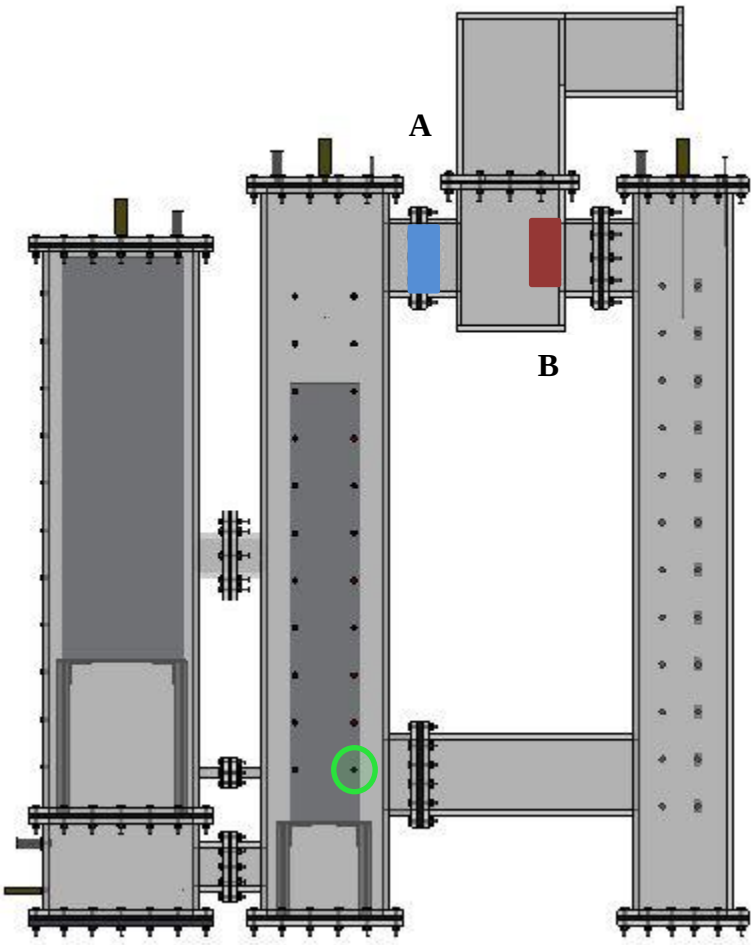

Figure 43. Simplified HTGR test facility with location of oxygen sensor, aluminum flange and hinged louvre indicated.

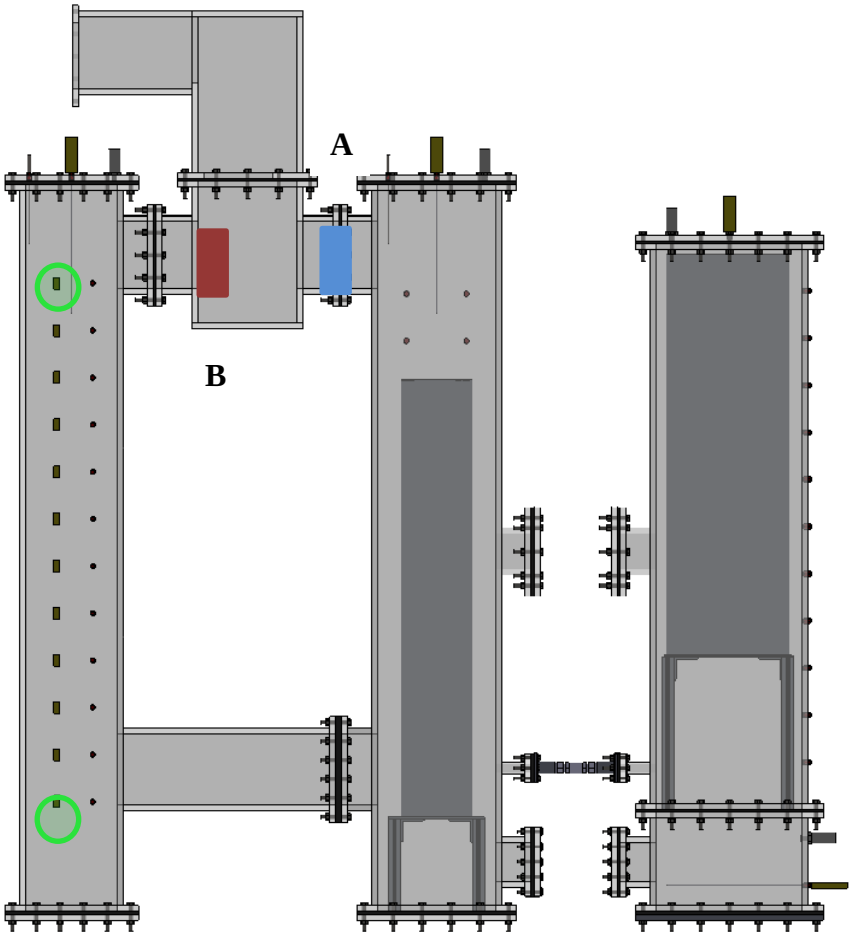

Figure 44. Simplified HTGR test facility with location of oxygen sensors, aluminum flange and hinged louvre indicated.

The aluminum flange is indicated by the blue and designated as "**A**" in Figure 43 and Figure 44 while the hinged louvre is designated in both figures as "**B**" and indicated by the maroon bar. For this test a steady gas injection into the test facility was also desired as one of the test parameters. This was achieved by connecting the end of

the gas line to one end of a Micro Motion® ELITE Coriolis flow and density meter. The flow meter is connected to a Micro Motion® Model RFT9739 field-mount transmitter that is used to compute and display the mass flow rate and density of the fluid. The flow meter and transmitter are shown in Figure 45 and Figure 46, respectively. The meter operates on the principle of inducing a vibration of the flow tube through which the fluid passes. Sensors analyze changes in frequency, phase shift, and amplitude of the vibrating flow tubes that occur from the Coriolis effect of the rotating reference frame that is provided through the vibration. The observed changes may then be used to deduce the mass flow rate and density of the fluid. The flow meter, when connected to the field-mount transmitter has a flow accuracy for a gas of ±0.10% with a further error added or

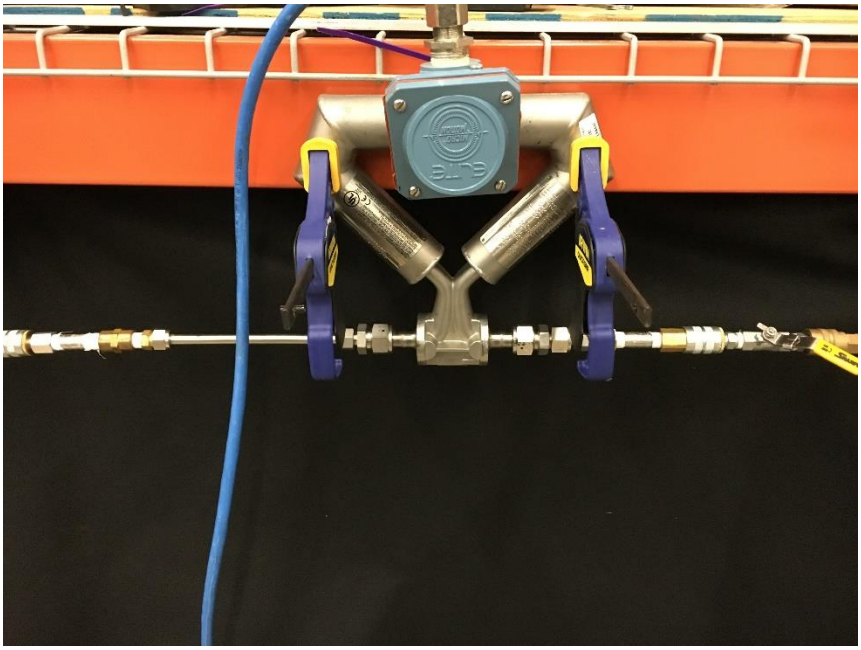

Figure 45. Micro Motion Coriolis flow meter.

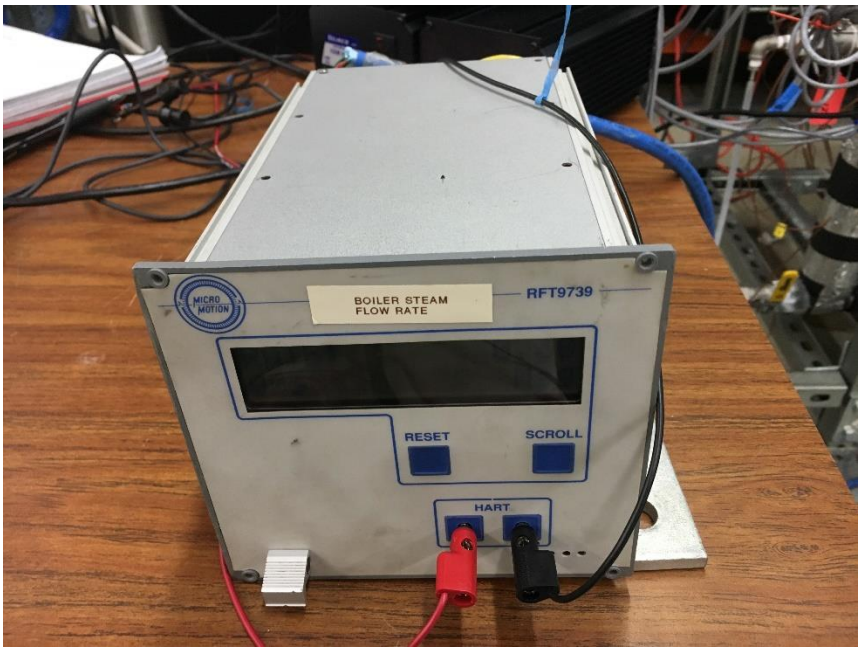

Figure 46. Field-mount transmitter.

subtracted based on the flow rate of the gas, flow repeatability of ±0.05% and density accuracy of ±0.5% $kg \cdot m^{-3}$.

The desired flow rate for this test was 1.66 $kg \cdot hr^{-1}$, or 0.46 $g \cdot s^{-1}$. From Figure 45 an adjustable ball valve was installed at the inlet of the Coriolis flow meter where the inlet of the gas line was connected. The gas line from the helium tank regulator was connected to the inlet of the Coriolis flow meter and the ball valve was adjusted until the desired flow rate was achieved, as indicated on the micro-transmitter display. The ball valve was not adjusted after the required mass flow rate was achieved at the outlet of the Coriolis flow meter. One observation from conducting tests with the helium is that once the helium tank begins to deplete the flow rate and outlet pressure may change

accordingly. As a result, helium tanks with at least 50 psig were desired throughout the duration of the experiments. Tanks that were nearly empty interfered with the testing conditions and maintaining the constant flow rate became more problematic. To keep the gases injected into the test facility as pure as possible, the gas line was purged with helium for 5 minutes before connected to the test facility to initiate the experiments.

Before proceeding with the experiment, the polycarbonate flange with the joined hinged louvre was placed between CV4 and CV5 at flow path V45. The hinged louvre was then situated between CV4 and CV6 at flow path V64. The Molykote vacuum sealant was applied around the edge of the hinged louvre and pressed firmly against the wall of CV4 to form a leak-tight door that was further reinforced by the neodymium magnets installed on the hinged door and outer wall of CV4. The combination of the magnets and leak-tight door created a seal that would open at or close to 1 psig. To hasten the retesting process, which required reapplying the vacuum sealant and ensuring a leak-tight seal between the hinged louvre and flow oath V64, the flanges on CV4 and CV5 were joined together by the neoprene gaskets and locked in place with four small Dewalt trigger clamps, placed at each corner of the two flanges instead of with bolts. Although this configuration might allow for some helium leakage through the two flanges and gaskets, the main flow path that opened after the depressurization expedited the removal of helium to the outside environment so that it was a significant factor in the final oxygen concentration measurements.

To initiate the test, the helium regulator was set to 18 psig and the outlet gas line was connected to the inlet to the Coriolis flow meter. Since the ball valve regulating the

mass flow rate was already set to allow a mass flow rate of 0.46 $g \cdot s^{-1}$. The outlet gas hose line was connected to the top of CV3 through the quick-disconnect fitting. CV1 and CV2 were not in communication with the test facility and were isolated through the use of polycarbonate flange caps at the flow path junctions that would normally allow for communication with CV3. Leak path L3A and L6A were active during this test and further enabled helium and air leakage during testing. After connecting the gas line, helium was injected by operating the ball valve at the end of the line connected to the quick-disconnect and allowing the facility to rapidly pressurize until the mechanical operating pressure of the hinged louvre was exceeded. The overpressurization forced the door open and opened vent path V64 to the environment which resulted in the facility quickly returning to ambient pressure while air entered the facility with a subsequent ejection of helium through momentum and diffusive forces.

The pressurization and depressurization of CV3 and CV6 is shown in Figure 47. The plot in Figure 47 shows the pressure inside of CV3 and CV6 over a duration of 100 seconds. The initial pressurization is shown as time zero where helium was first injected into the test facility. The results show that the pressurization and subsequent opening of the hinged louvre happened in around four seconds at a pressure of around 1.08 psig. The depressurization was instantaneous, as noted in Figure 47 by the sudden drop in both pressure profiles at around four seconds and that the pressure drop ensued at the same instant. The drop in the pressure profile of CV3 below zero was due to the calibration of the pressure transducer since the intercept value at ambient

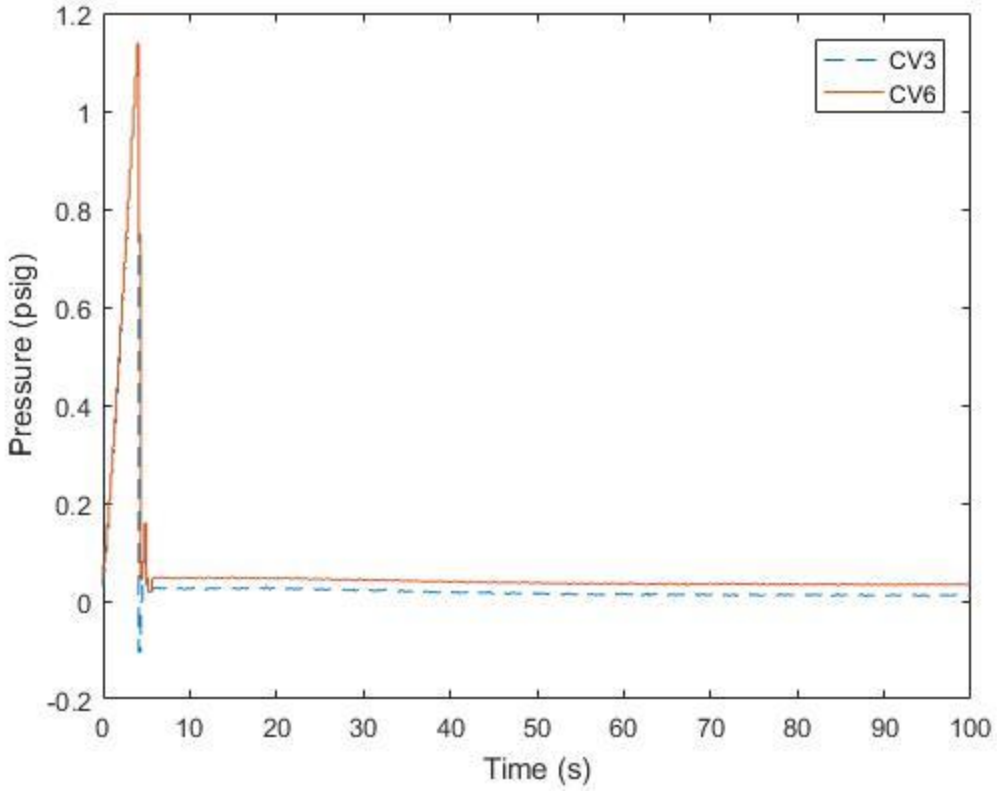

Figure 47. Pressure inside of CV3 and CV6 during rapid depressurization at 1 psig.

pressure is below zero. During the initial pressurization the pressure profile for both CV3 and CV6 is slightly curved that may be from the selected sampling period. Since the pressurization, and thus pressure change, happens at a much faster rate than during the air refilling phase as indicated by the relatively flat profile starting at 10 seconds, the sampling rate may not have been fast enough to capture and reconstruct the pressure profile and then reproduce a smooth continuous signal, which was set to 60 Hz. This may be mitigated by some foresight into how fast the pressure changes during a specified phase of future tests. Consideration of the processor speed, extraneous signal

noise and the control algorithm frequency might be other factors to consider when selecting an appropriate sampling rate for the pressure transducers. Nonetheless the dynamics of the pressurization and depressurization phases are precisely captured as indicated in Figure 47. After the rapid depressurization the hinged louvre returned to the initial position with a small gap between the door and the wall of CV4 to allow for air to enter and helium to escape through the exit flow path. In other words, the rapid buildup of helium inside of CV3 and CV6 resulted in a pressure exceeding the design pressure of the hinged louvre and forcing the louvre open almost instantaneously. The door then quickly returned to the initial position with a small opening where the helium exited during the lock-exchange flow of both gases at flow path V64.

H.P. Gröbelbauer et. al. discussed the intrusion of light gases into heavier gases and vice versa [36]. The discussion concluded that the velocity of a lighter gas, such as helium, moving into air is four times lower as that of air moving into helium [36]. The discussion also concluded that an organized vortex motion of an intruding gas front might develop for large density differences where the heavier gas is released with initially high potential energy [36]. The velocities determined from the experiments for both air moving into helium and helium moving into air were constant and linear that indicated that viscous effects were negligible but that air moving into helium produced a more turbulent front [36]. Although the indication of this phenomena is difficult to identify strictly from intrusive measurements, other pertinent behavior may be identified that is a direct consequence of previous results. The oxygen concentration measurements inside

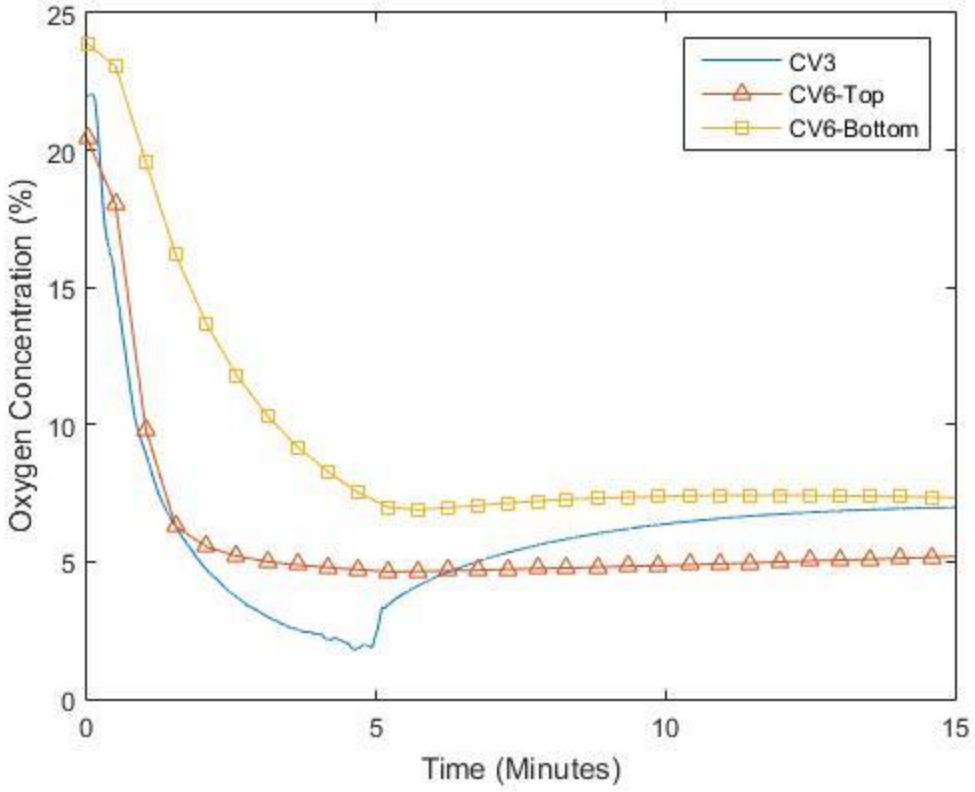

Figure 48. CV3 and CV6 Oxygen concentration after depressurization.

of CV3 and CV6 are shown in Figure 48. The oxygen concentration measurements inside of CV6 are for the oxygen probes located at the top and bottom of the test volume. The concentration measurements shown are for a time span of 15 minutes, over which 5 minutes were of continuous injection of helium into the test facility through CV3. Time zero in Figure 48 was just before the instant the facility pressurized to 1.08 psig and activated the hinged louvre. The oxygen concentration profiles in Figure 48 show apparent humps nearing the end of the pressurization inside of the test facility. The hump in the CV6-Bottom profile appears to decrease back to the ambient oxygen concentration

reading while the oxygen concentration in CV3 decreases immediately after the initial spike. The reason for the immediate decrease in the oxygen concentration in CV3 after the sudden bump was from the pressurized helium forcing the air into the neighboring test volume, CV6. The sudden increase in pressure temporarily forced more air into CV6, slightly increasing the density and subsequent oxygen concentration as detected by the oxygen probe while CV3 quickly filled with helium and purged the air out of the test chamber. This can be further supported by the lack of an apparent bump in the pressure profile of CV6 at the top, where most likely the pressurization occurred so rapidly that the oxygen probe did not detect the change in density before the hinged louvre was activated and the excess gas expelled. Qualitatively evaluating the two bumps that occurred at the bottom of CV3 and bottom of CV6, the time difference between the two peaks was around 0.7 seconds. Therefore, the velocity across flow path V36 was around 3.63 $ft \cdot s^{-1}$ (1.11 $m \cdot s^{-1}$). This is slightly faster than for the combined leak rate test in CV3 and CV6 with the polycarbonate door at the exit of CV5 removed at 1 psig. However, the pressure in this case was slightly higher at the moment of depressurization and may have been injected at a higher mass flow rate since the mass flow rate for the previous combined leak rate test was not actually measured, but the time frame for depressurization was almost instantaneous for both tests.

Further support for the rapid depressurization from the forcing of air into CV6 by the pressurized helium is the relative constant oxygen concentration before the hinged louvre operated as shown in an extended plot of the oxygen concentration at an arbitrary

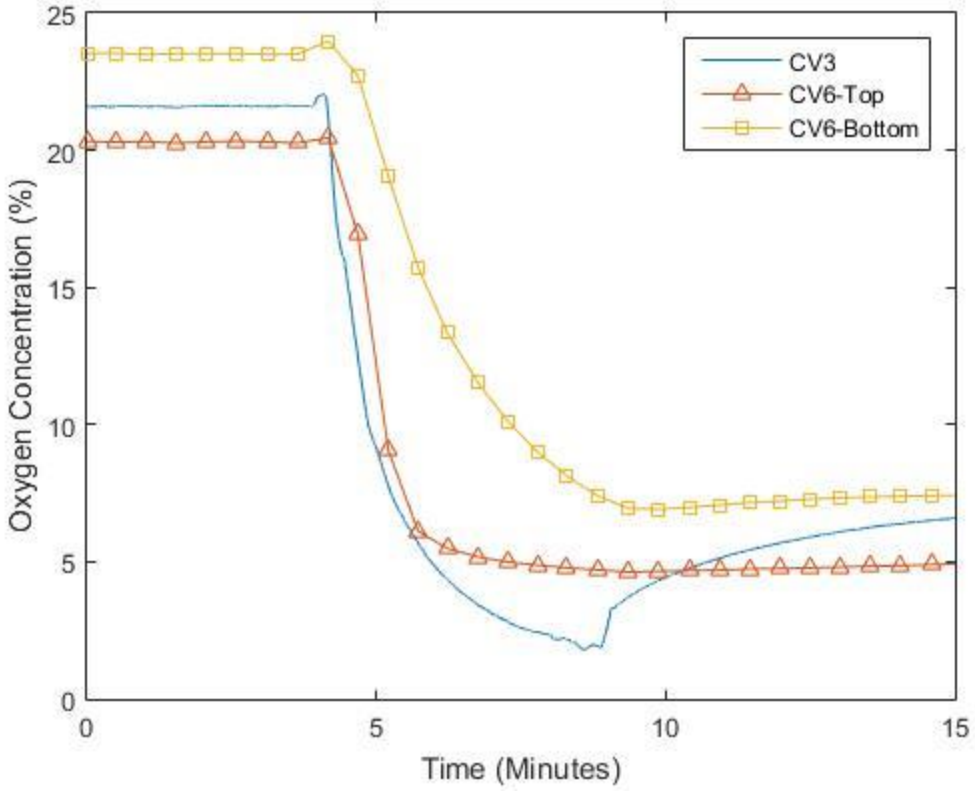

Figure 49. CV3 and CV6 Oxygen concentration after depressurization.

time before the door opened and after over the same time period as in Figure 49. The plot of the oxygen concentration in Figure 49 shows the flat oxygen concentration profile in CV3 and CV6 before the depressurization. After depressurization the oxygen concentration values quickly fall as shown previously, indicating that the helium was then allowed to move freely through the flow paths to the outside environment after the initial volume of air had been forced out of the facility, leading to the sudden drop in helium concentration. The increased density of the pressurized helium allowed for the forceful removal of air from CV3 into flow path V36 into CV6, but the depressurization

resulted in the helium quickly returning to ambient pressure. The gas exchange and helium flow was then governed by both momentum and buoyancy forces after depressurization of CV3 and CV6.

Because of the speed of the depressurization and the precision of the oxygen probes, the time frame for the gases to exchange and move from the bottom of CV6 to the top of CV6 is more difficult to identify. Other additional factors include the aforementioned vortex development or Rayleigh-Taylor instabilities that may serve to disturb the flow and reduce the momentum of either both the air and helium as the gases exchange and fill or exit the test facility. Numerical results of air superposed over helium in a downward acting gravitational field have shown the development of flow instabilities at the interface of the two fluids, forming a mushroom cap and growing more unstable over time [37]. This may be a reason for the unapparent peak in the oxygen concentration profile for the top of CV6 compared with the other two profiles since helium and air are more likely to interact at a higher elevation where the gases have a higher potential energy. One other feature to observe is that the oxygen concentration immediately begins to increase in CV3 at the 5 minute mark while slowly increasing at the bottom of CV6 and appears to increase only slightly before leveling off at the top of CV6. The small increase at the top of CV6 is from the stratification of the lighter helium after reaching ambient pressure and the large increase from the heavier air settling at the bottom of CV3. The helium and air are diffusion driven and is the primary reason for the slow change in the concentration after the 14 minute mark.

The peculiarity is at the bottom of CV6 where the concentration does not increase by much over the 10 minute observation window after the helium injection is stopped. One reason may be from the positioning of the oxygen probe. Because the probe did not penetrate completely to the center of CV6, the probe may not have made contact with the air refilling the test facility. This can be corroborated by the slope of the oxygen concentration profile at the bottom of CV3 being less than the other two oxygen concentration profiles during the injection period. The slope of the oxygen concentration profile before the end of the injection period for CV3 and CV6-top display the same trend compared with the bottom of CV6 and, again, may be from the positioning of the probe since air entering the test facility immediately flows through flow path V36 as identified by the instantaneous increase in the oxygen concentration in CV3 after the end of the injection period at around 9 minutes. The delay in the drop in the oxygen concentration at the top of CV6 compared with the bottom of CV3 is because helium is injected inside CV3, and as the door operates, a counter-current of air quickly intrudes into the test facility before the first stream of helium moves towards the exhaust after equilibrium of the pressures.

Since the velocity of the helium is approximately zero since the gas exchange is mainly governed by diffusion and buoyancy forces, then according to the densimetric Froude number the helium behaves nearly as a plume. T. J. O'Hern et. al. showed that for a helium plume, a Rayleigh-Taylor instability develops at the base of the plume that leads to a vortex that grows to dominate the flow [38]. This supports the previous claim about vortex development for an intruding gas front with large density differences. The

results also showed that strong turbulent structures developed at the plume interface between air and helium that formed from buoyancy-driven vorticity generation [38]. Therefore, the two gases inside of CV6 were more highly disturbed from the presence of air flowing in at the top of CV6 and the lower density helium flowing into CV6 at the bottom. This may have served to interfere with the gas refill phase of the test where air should have stratified at the bottom of CV6 and helium at the top. The vortex development may have entrained fluid below this plume, including air entering the test volume and inhibited the development of equilibrium between helium and air. Consequently, air entering CV6 did not reach the oxygen probe located at the bottom over the observation time of the experiment and resulted in the flat oxygen concentration profile after 5 minutes in Figure 49.

Stratification of helium occurs in CV3 where the injection point was. Therefore, the gas exchange is more stable since the lighter fluid resides above the heavier fluid, air, as it re-enters the facility through flow path V36. The dynamics of the air flow entering the facility is largely dominated by diffusion and the fraction of air inside of CV3 may be determined by Equation (51)

$$\frac{\partial \mathrm{X}_a}{\partial t} = D_{a,he} \frac{\partial^2 \mathrm{X}_a}{\partial z^2} \tag{51}$$

where X_a is the mole fraction of air and the same as the previous definition for mole fraction, y_i. The diffusion coefficient between air and helium is denoted by $D_{a,he}$ and the

coordinate z is in the vertical direction. The value of the diffusion coefficient was experimentally determined to be 0.7335 $cm^2 \cdot s^{-1}$ at room temperature [39]. Assuming the test volume is an infinite medium, the mole fraction of air may be analytically determined from Equation (52) [40]

$$\mathrm{X_a}(z,t) = X_{a,he}\left(1 - \mathrm{erf}\left(\frac{z}{2\sqrt{D_{a,he}t}}\right)\right) \tag{52}$$

where $\mathrm{X}_{a,he}$ is the mole fraction at the interface of helium and air and is assumed constant because of the constant helium-air counter-current flow at the inlet to CV3 through flow path V36. The concentration measurements at the bottom of CV3 agree with the computation of this result over a time period of 10 minutes, the time period of observation after shutting off the helium injection into the test facility, indicated by the flat oxygen concentration profile in CV3. Comparison between the analytical solution may be facilitated in the future by the addition of oxygen concentration sensors in CV3 that are spatially distributed inside of CV3. The initial jump in the oxygen concentration profile of CV3 may be from the stratification of helium after the injection is shut off, resulting in air and helium rapidly coming to equilibrium inside of the test volume. The results in Figure 50 show that the trend in the oxygen concentration does follow the behavior of the analytical solution described in Equation 76. Correspondingly, the results of the analytical solution in Figure 50 show that the oxygen concentration should

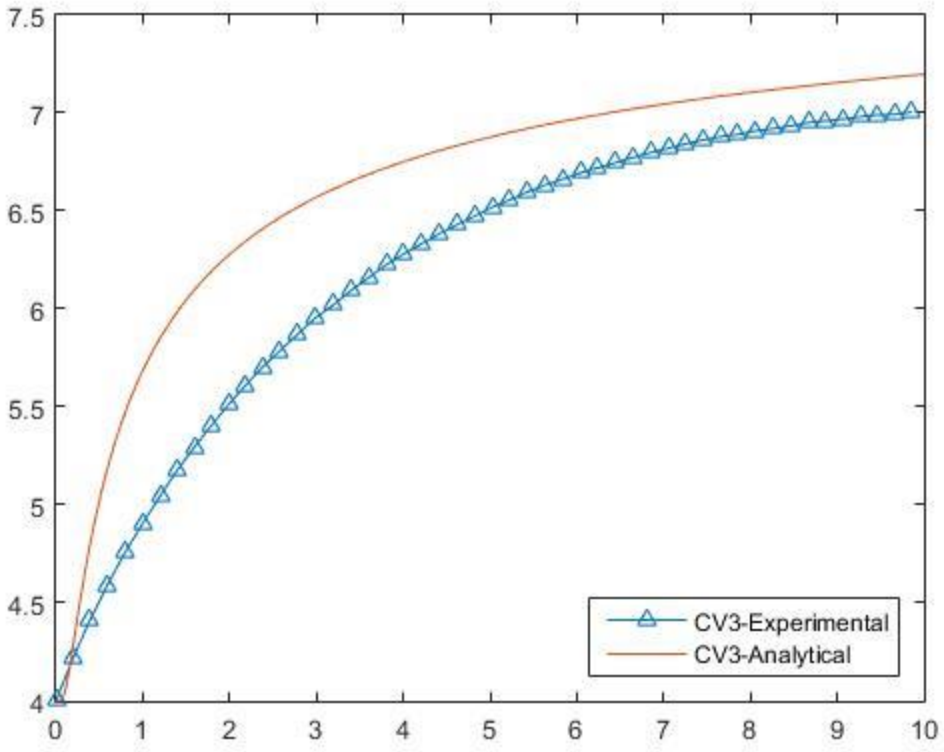

Figure 50. Analytical solution of oxygen concentration measurements inside of CV3.

increase by around 3% over 10 minutes and is confirmed by the oxygen concentration profile at the bottom of CV3 in Figure 50 and is shown below.

V.4 Impinging Horizontal Jet of Helium Inside of CV3

A horizontal jet of helium ejecting into CV3 through the check valve was analyzed qualitatively using particle image velocimetry (PIV). The test was conducted inside of CV1 and CV3 only. CV6 was completely disconnected from the rest of the test

facility. CV4 was connected to CV3 through flow path V34 and CV5 was situated on top of CV4 that allowed venting to the outside environment. CV2 was not in communication with the test facility during this experiment. For this test the scaled facility retained the previous configuration shown previously in the HTGR building scaled model design with the check valve installed between CV1 and CV3 in lieu of the bypass system installed at a later date. The Swagelok˚ 316 stainless steel check was designed to operate at 1 psig using a precisely manufactured spring that was designed to close prior to flow reversal.

The PIV setup in Figure 51 consists of a Ningbo Yuanming Laser Technology Co. 10 Watt (10W) Nd:YAG continuous wave laser with an output of 532 nm. Images were collected using a NAC Memrecam GX-3 high-speed camera with 12-bit depth and a maximum resolution of 1280 by 1024 pixel and CMOS image sensor. A TSI 610026 collimator was installed in front of the laser and used to produce a 3 mm thick laser sheet. The collimated laser was reflected off a small mirror placed in front of the laser and was situated above the check valve. The collimated beam was reflected 90˚ into CV3 directly down the center of the test volume and produced the desired interrogation region described above.

The helium flow was seeded with AkzoNobel hollow, thermoplastic microspheres that contain isobutane gas. Each microsphere has an average diameter of 40 μm and the isobutane gas has an average density of 2.51 $kg \cdot m^{-3}$. The particles were injected into the flow through a 1/4” NPT threaded hole in leak path L13 and allowed

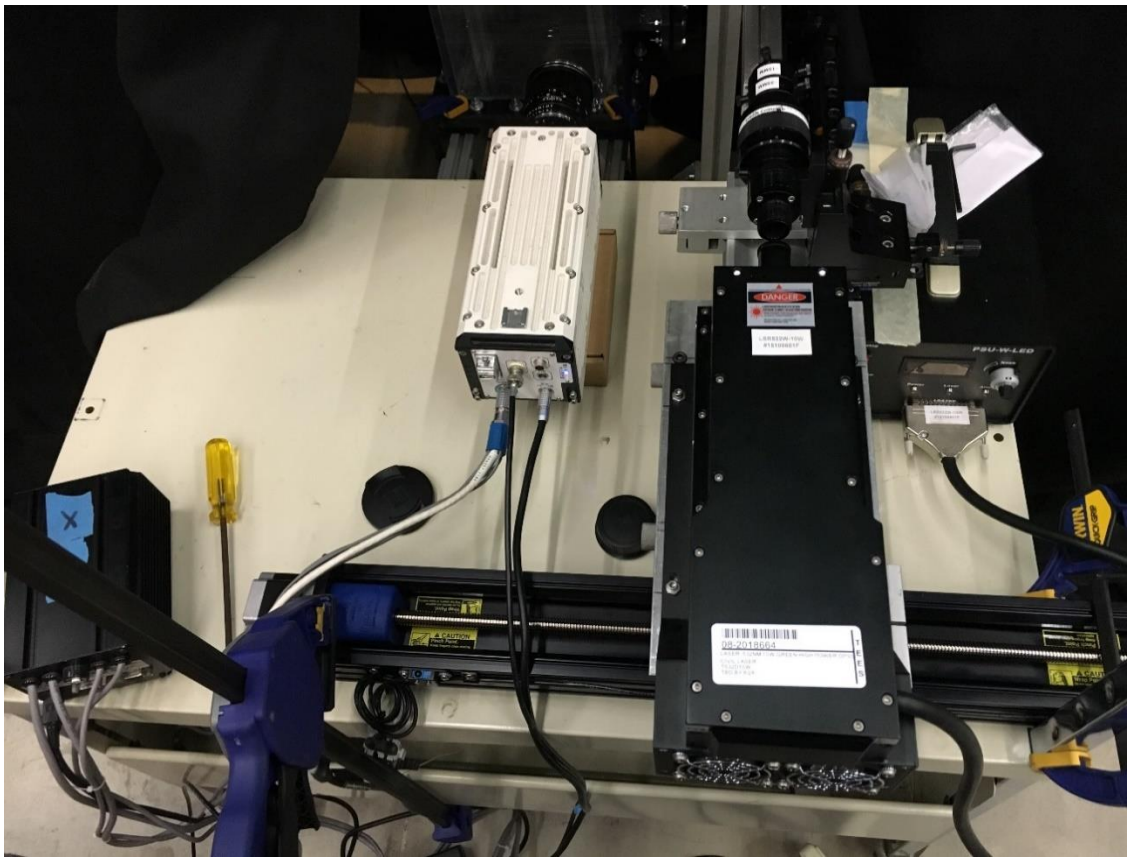

Figure 51. PIV setup.

to partially fill the region where the helium entered CV3 at flow path V13 through the check valve. The particles were selected because of their reflectivity and relatively low density compared with other seeding particles suitable for gases. Other seeding particles such as olive oil would form a residue on the walls of the test facility and might be too arduous to remove completely. The PIV code *prana* and MATLAB was used for post-processing the input images.

The experiment was initiated by the injection of helium into CV1 through the

quick-disconnect fitting on the top of the volume from a helium tank with the regulator pressure set to 15 psig. A collimated laser sheet was emitted into CV3 through a series of optics and mirrors. The laser sheet was produced perpendicular to the image acquisition system and directly above the centerline of the check valve and through the center of CV3. An animated description of the laser sheet intruding into CV3 is shown below in Figure 52. The interrogation region where the laser sheet was produced was 1.57” (0.40 cm) wide and 4.72” in height (1.20 cm) and was between the right wall of CV3 and the steam generator. CV1 was filled with helium until the operating pressure of the check valve was exceeded, allowing for flow into CV3 where the seed particles were picked up by the flow. The PIV images were collected using the NAC camera operating at a frequency of 2000 Hz, a frame size of 384 by 1024 pixels and the laser operating continuously at 10W. A multi-pass system was utilized to post-process every 10 images

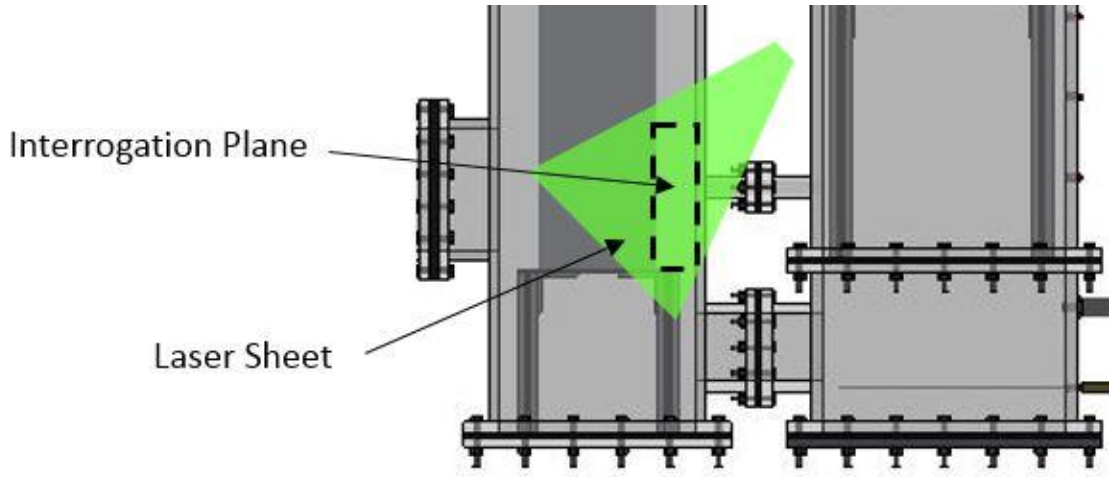

Figure 52. Animated description of interrogation region.

and were correlated using a standard cross-correlation algorithm. The interrogation window size chosen was 64 pixels by 64 pixels on the first pass and 32 pixels by 32 pixels on the second pass with a window overlap of 75% on both passes. Multiple passes were used in an iterative manner to increase the accuracy of the displacement peak estimation and to reduce noise by shifting the interrogation window by a discrete pixel amount based on the estimated velocity field obtained in the first pass.

The pressure response inside of CV1 is represented by Figure 53 for a duration of around 25 seconds. Time zero is arbitrary in this case and is before pressurization inside of CV1 was initiated. The pressure response shows that the time frame from the beginning of pressurization to the point where the check valve operated was around 2.8 to 3 seconds and cracked at a pressure of 0.6 psig. The pressure inside of CV1 dropped from 0.6 psig to 0.1 psig in around 3 seconds and was almost completely depressurized after 25 seconds. The check valve did not open at the manufactured operating pressure of 1 psig and has shown inconsistencies in previous benchmark testing. The inconsistency in the check valve is most likely from the delicacy of the components since the spring required must be manufactured to perform at a low operating pressure, and as a result, is made very thin. This results in a spring that is easily deformable and consistent use quickly wears down the spring's elasticity. Check valves designed for higher operating pressures such as those in the industry are manufactured more rugged with thicker spring. Unfortunately, the springs inside of the check valve are extremely thin and

malleable. Preliminary benchmark testing for different helium regulator pressures showed that the check valve did consistently operate at the same pressure, but not at

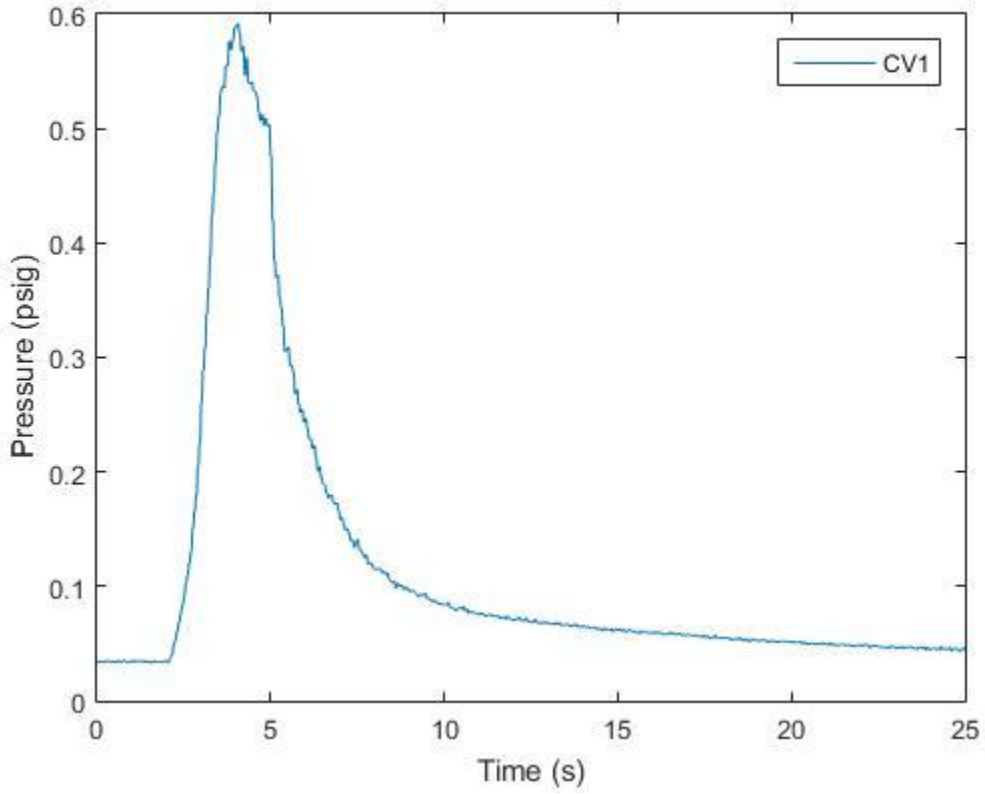

Figure 53. Pressure response inside of CV1 for a duration of 25 seconds.

1 psig and is further detailed in the Appendix. One other observation is that the depressurization was not sudden as seen in previous depressurization testing. The small orifice of the check valve did not allow for a large flow rate through flow path V13, which also depended on how much the spring inside of the check valve deformed. If the check valve opened partially then the resulting orifice through the flow path would have been significantly smaller and would have further reduced the amount of helium that

could flow through to CV3. Choked flow conditions were not suspected, however, since previous reports for air through an orifice of 0.010" have shown that for an upstream pressure of 1 psig the gauge pressure would have to be negative [41]. The pressure inside of CV3 during testing never exceeded ambient conditions, and consequently sonic flow conditions through the check valve were unlikely.

The velocity profiles inside of CV3 for the first second after the helium flow is discharged from the check valve is shown in Figure 54 for the first 0.25 seconds. Observation of Figure 54 shows that the helium discharged from the check valve into the ambient air with a velocity 0.7 $m \cdot s^{-1}$. Calculation of the Richardson number from Equation (53) resulted in a value slightly lower than one, indicating that the helium flow entering CV3 was not entirely a plume but was still advected by a momentum flux and displays some jet behavior

$$Ri = \frac{(\rho_\infty - \rho_j) g D}{\rho_\infty U_0^2} \tag{53}$$

where the density of the ambient air and of the initial jet are represented by ρ_∞ and ρ_j, respectively, D is the diameter of the intrusion, g is the acceleration due to gravity and the initial velocity is given by U_0. However, computation of the transition from momentum dominated flow to buoyancy dominated flow for an initial velocity of 0.7 $m \cdot s^{-1}$ showed that the length scale was less than 0.03 mm and was indicated by the vertical motion of the helium flow upon entry into CV3. A qualitative evaluation of the

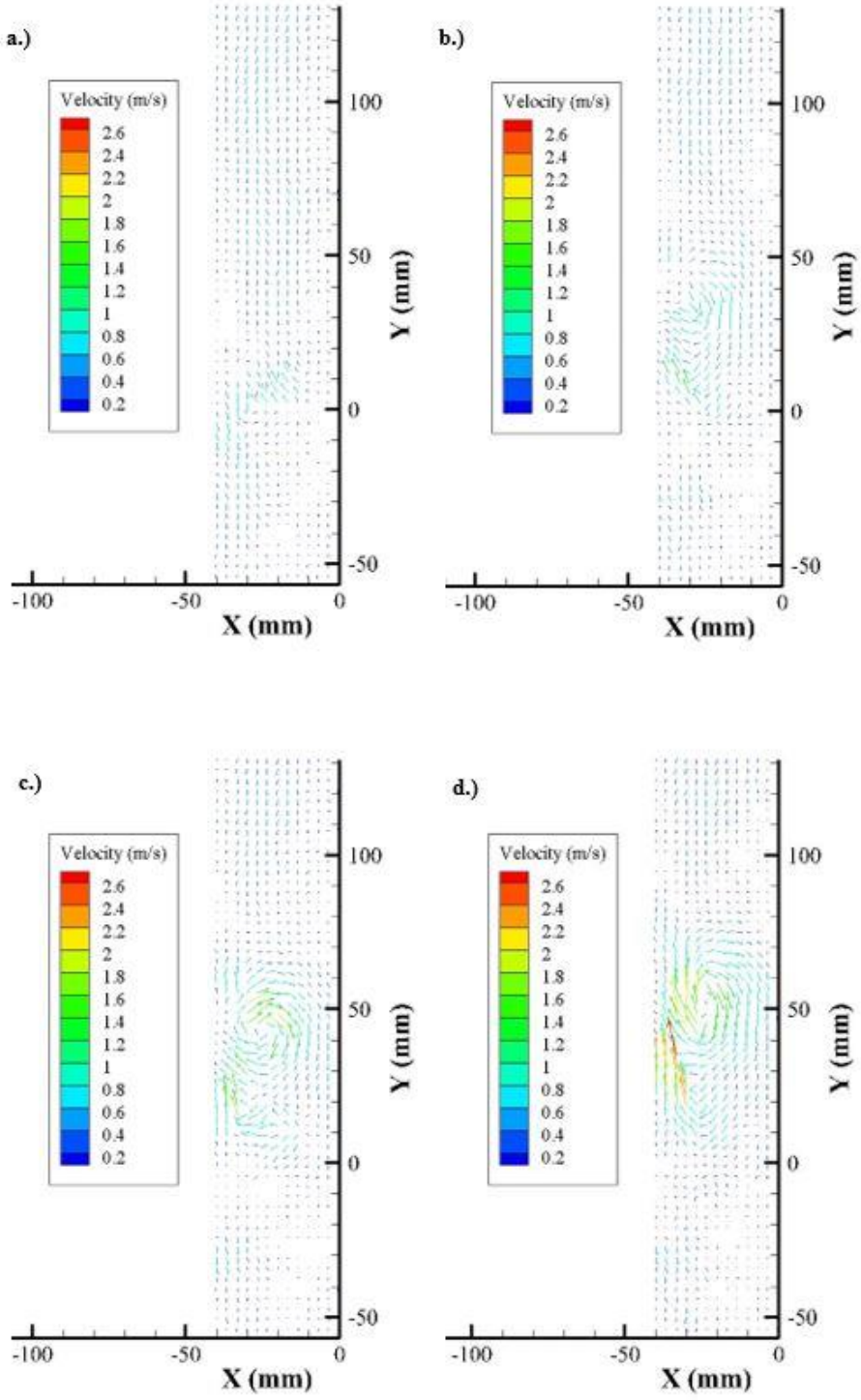

Figure 54. Velocity profile inside of CV3 at **a.)** time zero **b.)** 0.16 seconds **c.)** 0.21 seconds and **d.)** 0.25 seconds.

helium flow in CV3 resulted in a dependence on the angle as more fluid was discharged into the surrounding air. The initial flow of helium discharged into CV3 with an angle of around 50˚ to 55˚ but increases past 75˚ as time progresses and more of the initial helium content in CV1 flows through the check valve. This behavior is signified in Figure 54 by the increase in slope of the velocity vectors near the entrance of CV3 at a y-elevation equal to zero. The flow in Figure 54, upon discharge into CV3, immediately begins to rise in the vertical direction at the defined angle and impinges upon the steam generator model about one nozzle diameter from the entry point. The helium flow then begins to exhibit vortical motion upon impact as the fluid rolls up clockwise into the vortex and advect vertically up the side of the steam generator. As the vortical structure flows along the side of the steam generator the velocity vectors increase in magnitude. Previous experiments by Cetegen showed a rapid acceleration of the flow in the region just lagging behind the vortex and increased velocities in the region where the vortex resides [42]. Increases in turbulence were revealed by evaluating the velocity field as the vortex convected downstream, exhibited by scatter in the velocity vectors, along with increased entrainment of air around the tail of the vortex [42]. Reports from previous experiments have suggested that the development formation of turbulent structures at the interface between the helium and air are a result of buoyancy-driven, as opposed to gravitational, vorticity generation [38]. Although turbulent structures formation is not apparent from a quantitative evaluation of the PIV results, the chaotic motion of the seed particles and formation of vortical structures suggest strong turbulence at the point of impingement. As the vortical structure advects further along the interrogation region, air is entrained

underneath the vortical structure and is signified qualitatively in the flow by the seeding particles closely trailing the vortex along the steam generator.

The entrainment of air supports the previous hypothesis for the rapid depressurization test for the cause of the oxygen concentration at the bottom of CV6 not increasing at the rate of the concentration in CV3. The condition in CV3 is stable with helium residing at the top of the facility at the point of injection and air at the bottom where it most likely situates after entering the facility through CV6. However, inside CV6 the lighter helium intrudes into the heavier air, triggering the Rayleigh-Taylor instability that resulted in the vortex formation for the impingement case. As the two fluids mix inside, vortex formation occurs and entrains any air residing outside of the combined gas mixture, or plume that is then driven by buoyancy forces. This continual mixing draws in any remaining air outside of the plume, trapping the remaining helium situated around the oxygen probe at the bottom of CV6. This claim is not apparent and may be validated or refuted in the near future through further qualitative analysis such as flow visualization.

The velocity distribution at the wall of the steam generator is shown in Figure 55 starting at a height about four inlet diameters above the entry point into CV3 and is denoted Elevation 1. The other three elevations are separated by a distance of 5 mm where Elevation 4 is at the maximum height relative to the other three velocity profiles. The velocity profile at each elevation display the same behavior and tendency over the 1.9 second time frame. The initial peaks at 0.6 seconds represent when the helium flow first impinges the steam generator and generates the initial vortex. Observation of the

flow field in the region of the steam generator shows that after the vortex moves toward the top of CV3, the particles at the wall of the steam generator decelerate and come to a standstill. A previous analysis of buoyant helium jets reported the deceleration of the downstream [42]. The transition from a strong vortex to a plume is observed in the resulting flow field and will be presented in the next set of velocity vectors. After the initial peak in the velocity vectors the flow field again remains quiescent until around 1.2 seconds when the velocity suddenly increases to 4 $m \cdot s^{-1}$ at Elevation 1 up to 5 $m \cdot s^{-1}$ at Elevation 4. The flow field then appears to oscillate with an average frequency between

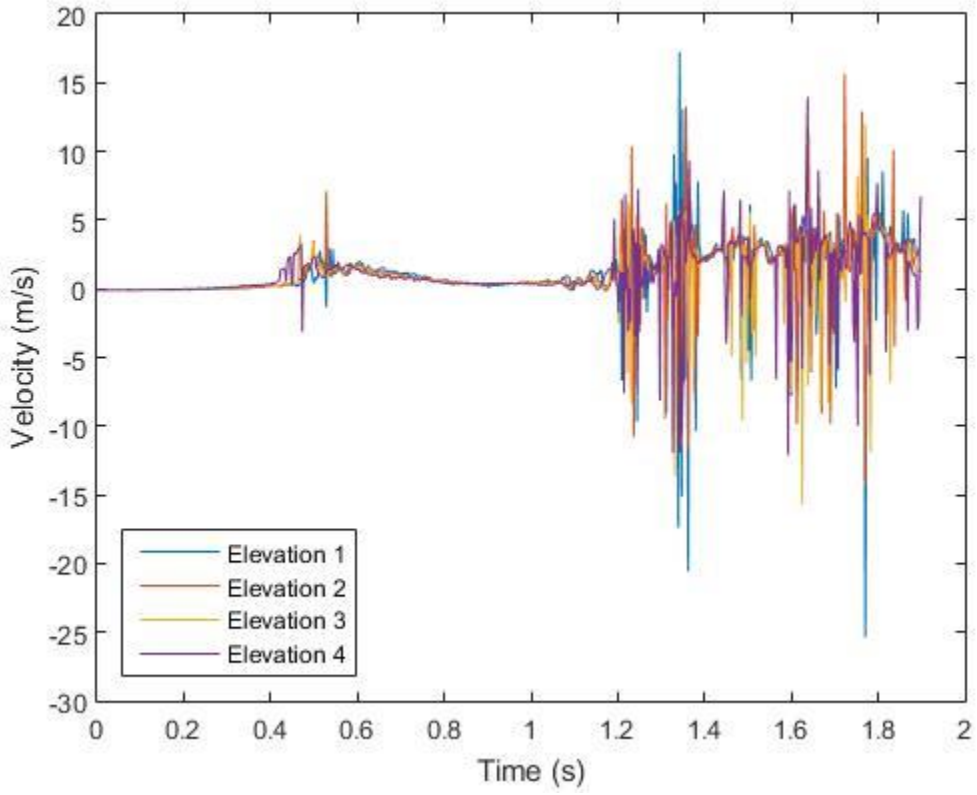

Figure 55. Velocity distribution at four separate elevations near the steam generator.

the four elevations of 5 Hz, as indicated for the velocity profile for Elevation 2 and Elevation 4 in Figure 56 and Figure 57, respectively. Previous studies have recorded frequencies from 3.5 up to 4 Hz for a helium-air plume [42]. The velocity at the steam generator before about 0.4 seconds is zero, indicating that up to the point of the jet impacting the steam generator the gas composition in that region was mostly air and no helium. The resulting velocity field from the entrainment of the gases and the advection of the vortical structure is first indicated by the strong peak at around 0.6 seconds with an intermediate peak of a smaller magnitude but longer duration. The gas mixture around the steam generator then decelerates and returns to the initial state.

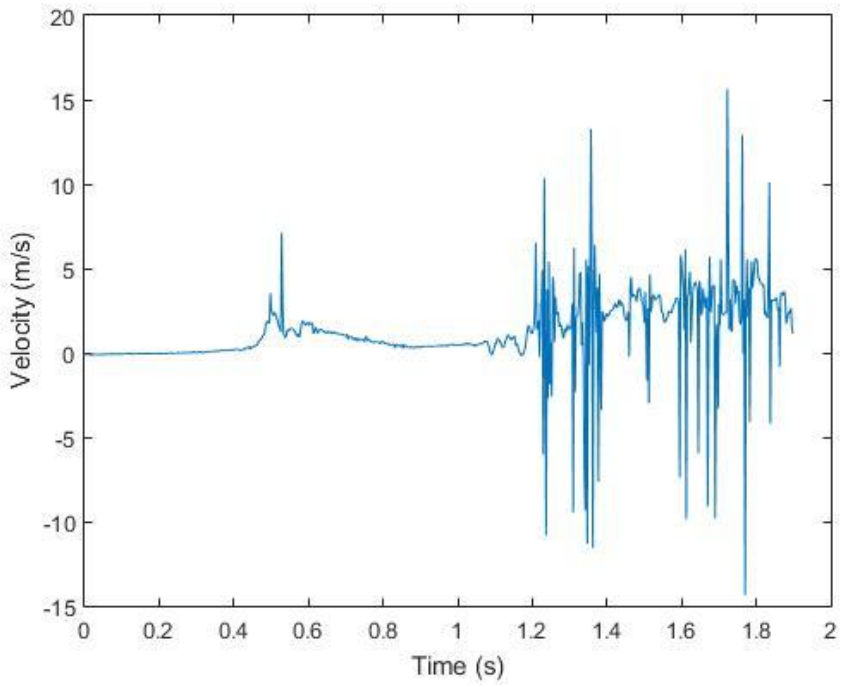

Figure 56. Velocity profile at Elevation 2 near the steam generator.

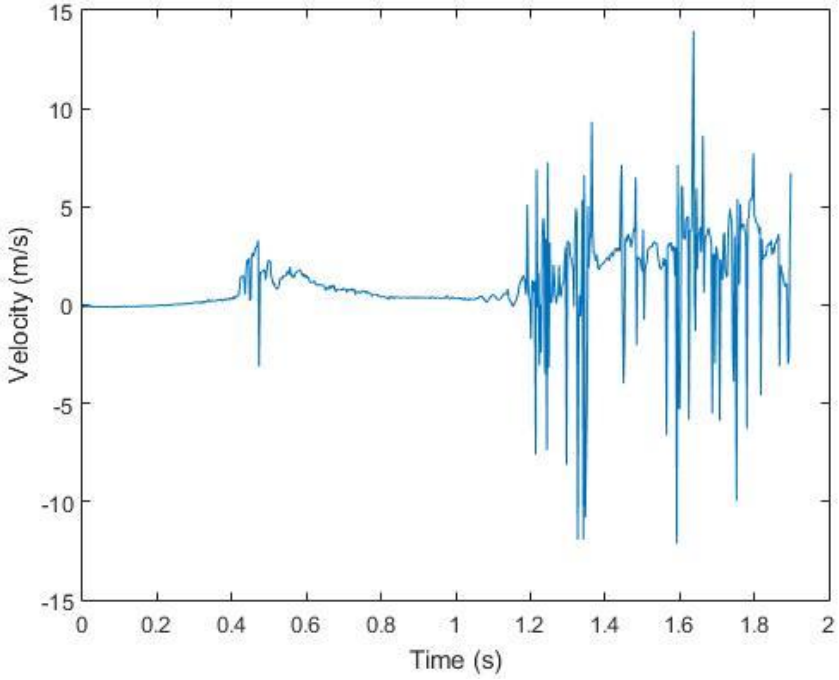

Figure 57. Velocity profile at Elevation 4 near the steam generator.

Figure 58 shows the velocity distribution inside CV3 from 0.30 to 0.45 seconds. The velocity profile in each frame shows deflected velocity vectors toward the central vortex which indicated a large radial entrainment of air over the helium flow toward the centerline, results similar to those found previously [38]. The velocity vectors trailing the main vortex in frame b.) also appear to accelerate to around 4 $m \cdot s^{-1}$. "Necking" of the fluid may also be observed in frame b.) as the vortex entrains the air below it and accelerates upwards, again indicated by the increase in velocity vectors at a subsequent time in frame c.). Finally, in frame d.) the helium/air mixture assumes a columnar shape with high velocities around the axis of the flow, which matches previous PIV experiments of buoyant plumes [42].

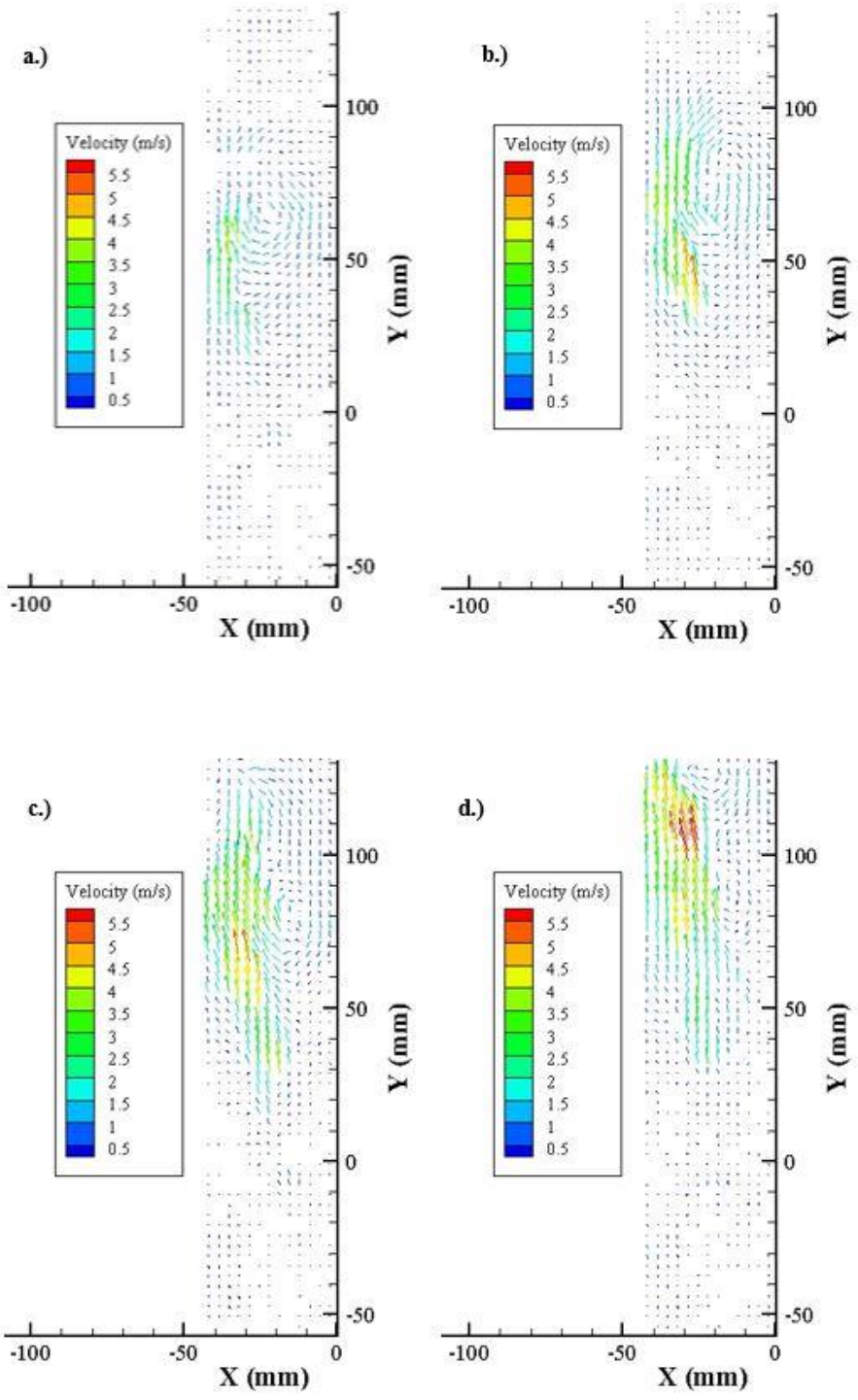

Figure 58. Velocity profile inside of CV3 at **a.)** 0.30 seconds, **b.)** 0.34 seconds, **c.)** 0.41 seconds and **d.)** 0.45 seconds.

The velocity profile in the vertical direction for three separate locations in the flow field, starting at 110 mm and separated by a distance of 5 mm, is displayed in Figure 59. The velocity in Figure 59, starting at frame **a.)**, displays much more fluctuations in the velocity as indicated by the erratic series of peaks. Moving from frame a.) to frame c.) the velocity profile before 0.6 seconds appears to smooth out and oscillate between -0.01 $m \cdot s^{-1}$ and 0.01 $m \cdot s^{-1}$. From observation of the flow field in Figure

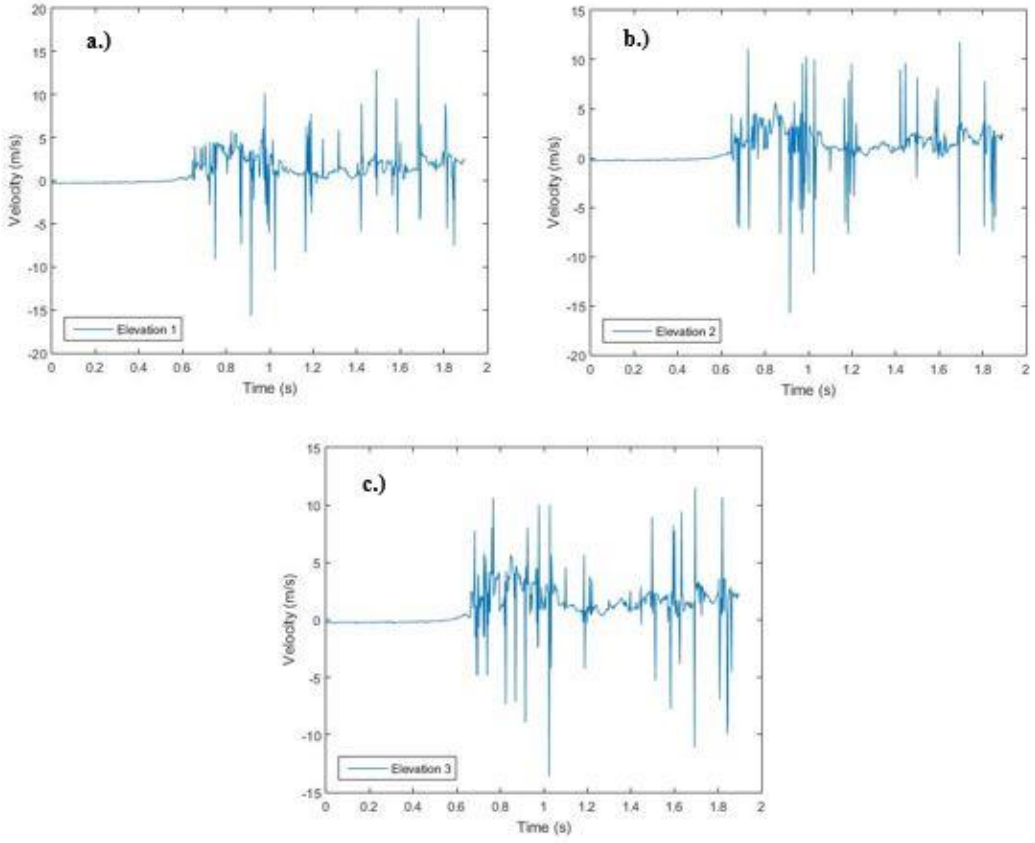

Figure 59. Velocity profile at **a.)** 112 mm, **b.)** 117 mm and **c.)** 122 mm.

60 shows the development of a secondary vortex while the initial vortex is advects to the top of CV3. The development of this secondary vortex and subsequent turbulent structures from the increased vorticity may account for the large oscillations in the velocity field as the elevation increases. Each velocity profile in Figure 59 has a prominent peak in the respective velocity separated by a time period of 0.10 seconds starting at 1.4 seconds in

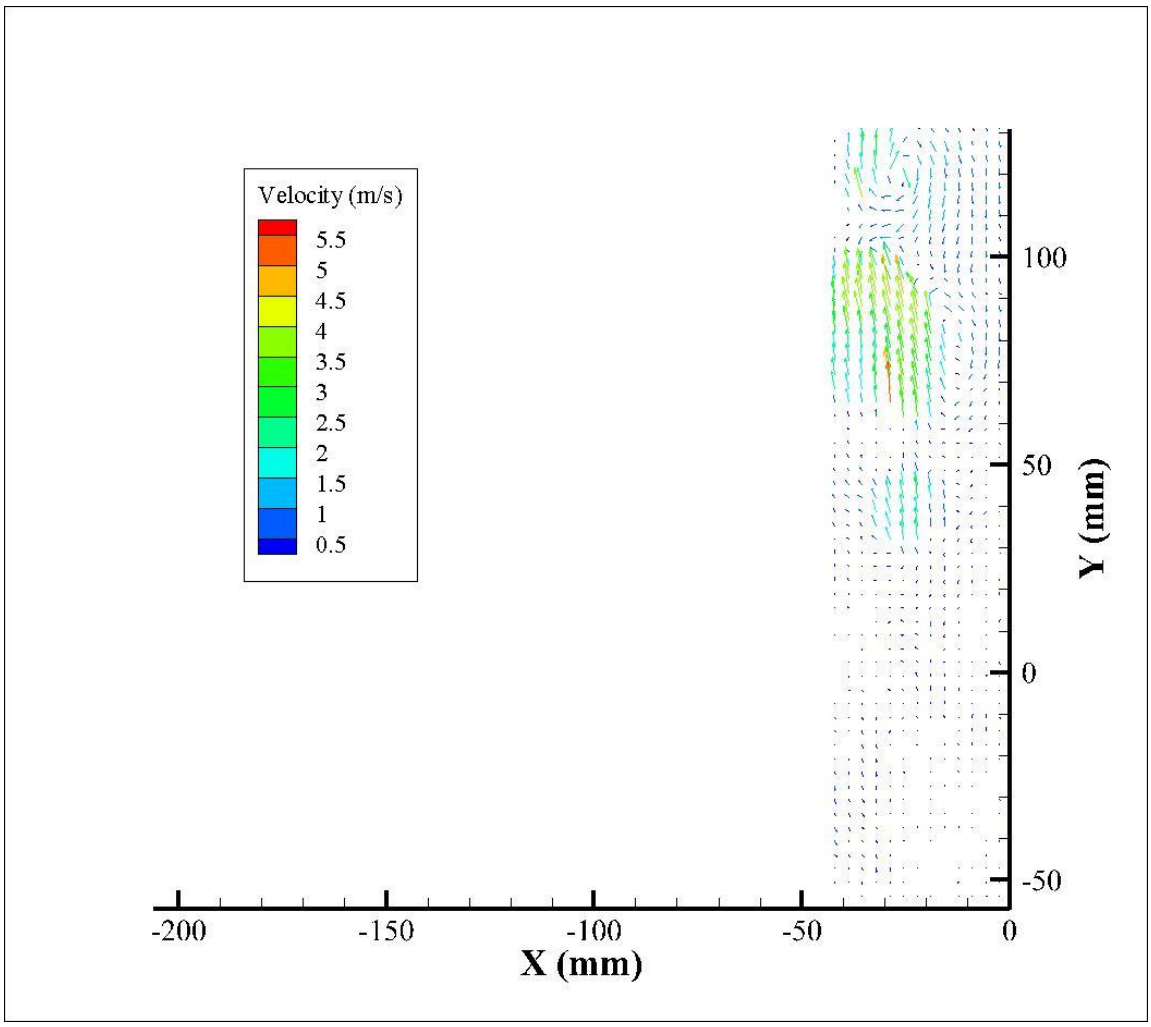

Figure 60. Velocity profile inside of CV3 at 0.43 seconds.

frame a.). Previous literature has described the “puffing” of a helium/air plume where the lighter fluid slowly accumulates until it reaches a sufficient volume to trigger a Rayleigh-Taylor instability caused by a heavy fluid overlying a light fluid [38]. As the vortex rises, it entrains air below it and accelerates upwards, narrowing down to a thin “neck.” This necking of the fluid was previously observed for the initial vortex formation at the wall of the steam generator. Acceleration of the flow is also observed as the primary vortex advects to the top of the interrogation region along with the entrainment of air as indicated by the tilt in the velocity vectors. The velocity vectors above the helium/air flow are angled downwards towards the center of the vortex while the vectors below are angled upwards at the same location. O’Hern et. al. found that the velocity in this region of puffing displayed periodic fluctuations in the velocity with occasional smaller peaks that signify weaker puffs [38]. However, the average puffing frequency was found to be around 1.37 Hz while it is almost 8 times that for the prominent peaks in Figure 59. Similar experiments found that the onset of vortex production was initiated about one a half nozzle diameter away from the entry point. For this particular test the onset of vortex production began somewhere between one a half and two nozzle diameters away from the entry point into CV3 [43].

A deeper understanding of the mean flow behavior was extracted from the resulting velocity measurements using the continuous wavelet transform and is defined as follows in Equation (54)

$$W(a,b) = \frac{1}{\sqrt{a}} \int_{-\infty}^{\infty} f(t)^{*} \psi \left(\frac{t-b}{a} \right) dt \tag{54}$$

where ψ is the mother wavelet and a and b are the *scale* and *translation* parameters, respectively. High and low frequency information is captured by convolution of the mother wavelet with the signal, $f(t)$, that generates a family of wavelets by dilation or contraction of the scale parameter. Starting from the lowest scale, the wavelet is compressed and placed at the beginning of the signal at time t = 0. The wavelet function is multiplied by the signal and integrated over all times and then normalized by the scale factor. This wavelet is then shifted by the translation parameter and recomputed. This procedure is repeated until the end of the signal is reached. Incrementally increasing the scale parameter generates a family of wavelet coefficients, ψ with a product dependent on whether the signal has a spectral component that corresponds to the current scaling parameter.

An infinite number of basis functions exist that provide localized information, each with different trade-offs between how compactly the basis functions are in space and how smooth they are [44]. Mother wavelets are generally oscillating, finite-length, fast-decaying waves that satisfy Equation (55)

$$C_{\psi} = \int_{0}^{\infty} \frac{|\psi(f)|^2}{f} df < \infty \tag{55}$$

where $C\psi$ is the admissible constant and implies that the Fourier transform of the mother wavelet vanishes at zero frequency and that the average value of the wavelet in the time domain is zero. The Morlet wavelet was selected because of its previous use in analyzing turbulent behavior [45], [46]. Tennekes and Lumley also proposed that eddy structures are characteristically similar to a superposition of Gaussian wave-packet and resemble the Morlet wavelet, which is a complex exponential carrier wave multiplied by a Gaussian window [47].

The results of the wavelet transform are shown below in Figure 61 for the corresponding velocity signals in Figure 59 over a time period of 1.9 seconds. The results of the wavelet transform show repeating structures in all three frames with frequencies less than 20 Hz every 0.1 seconds between 0.8 and 1.1 seconds. A separate set of repeating structures appears around 1.4 seconds and repeats every 0.2 seconds but decreases in magnitude from frame a.) to frame c.). The velocity profile in frame a.) in Figure 59 shows a series of minor peaks between 1.2 and 1.4 seconds and is represented by the lower magnitude wavelet coefficients from 30 to 70 Hz and is supported by the apparent absence of similar wavelet coefficients, and corresponding velocity peaks, in frame b.). All three frames have peaks centered around 60 Hz at around 0.8 seconds where the largest magnitude coefficients are located in frame c.) and stretched beyond 80 Hz. The reason for this stretching at larger frequencies is from through Heisenberg's Uncertainty principle where the relationship between time and frequency resolution limits the choice of scale. At lower frequencies, corresponding to larger scale values, the

frequency is well resolved but the time duration over which the frequency appears in the signal is spread out over a larger time interval as a consequence of Equation (56)

$$\sigma_f \sigma_t < \frac{1}{4\pi} \tag{56}$$

where σ_f and σ_t are the frequency and time width, respectively, of the mother wavelet. As the frequency increases for a certain time period the wavelets appear to stretch and

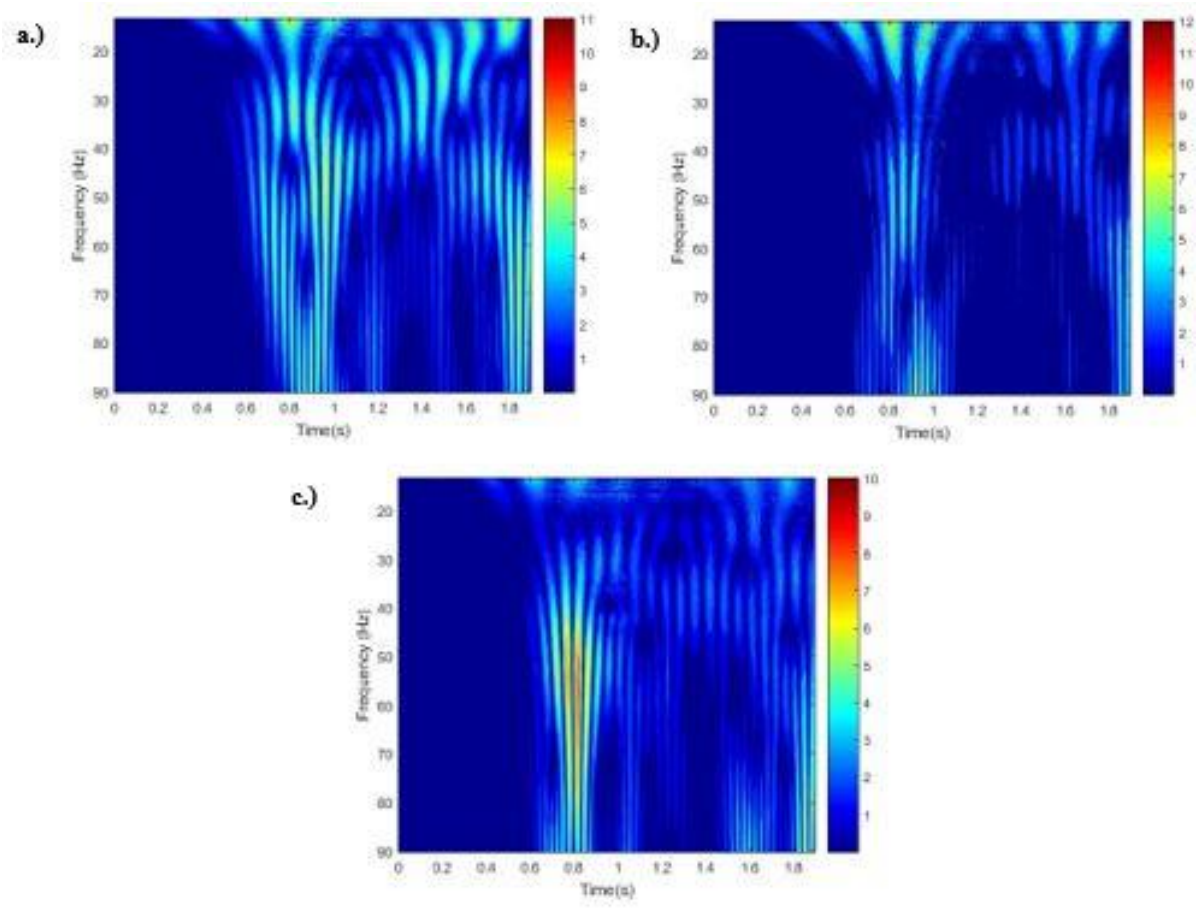

Figure 61. Continuous wavelet transform at **a.)** 112 mm, **b.)** 117 mm and **c.)** 122 mm.

distort, a consequence of the resolution window retaining a constant area centered around the central frequency of the wavelet function. As a result, the true frequency over a certain time duration is uncertain. The magnitude of the wavelet coefficients, indicating the strength of the convolution of the mother wavelet and velocity signal at each scale, is displayed in Figure 61 and denoted by the contour bar to the right of the plot.

Figure 62 represents the wavelet coefficients at 112 mm and 122 mm over a time frame of 1.9 seconds. The frequency range shown is from 8 Hz up to 90 Hz and selected to highlight important features of the mean flow without distorting the contour mapping. The plot in Figure 62 shows repeating structures frequencies less than 8 Hz in

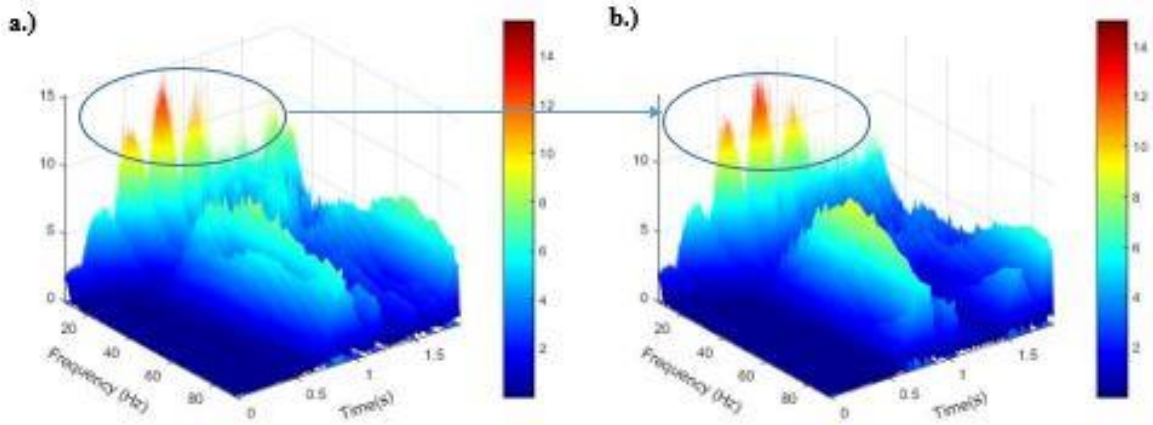

Figure 62. Continuous wavelet transforms at **a.)** 112 mm, **b.)** 122 mm.

both frame a.) and frame b.), but due to Heisenberg's Uncertainty principle the wavelets at low frequencies are stretched across several seconds and the true resolution of the wavelets are difficult to interpret. However, the structures display intermittency starting around 0.6 seconds and signify a large, low frequency eddy structures advecting through that portion of the interrogation region. Another structure at one second is shown in Figure 62 in both frames, indicating another large eddy structure with a larger frequency of rotation. The actual frequency for this structure is unknown because of the accurate resolution in time but it appears that the peak is close to 60 Hz and was indicated in Figure 61.

The single-sided discrete Fourier transform of each elevation is displayed in Figure 63 over a range of 350 Hz. The range of dominant frequencies at all three elevations are less than 10 Hz, and more accurately, less than 5 Hz. At elevation 1 and elevation 2 the dominant frequency is centered around 2 Hz while the dominant frequency at elevation 3 has a larger frequency component around 1 Hz. Nonetheless, the magnitude at these two frequencies is much larger than the frequencies. The resulting Fourier transform at each elevation reveals that toward the end of the spectrum higher frequency components is not negligible, having the same magnitude as the lower frequency components that more accurately describe the mean flow properties. At elevation 2 and elevation 3 the frequencies between 100 and 150 Hz displays a lower peak than the surrounding frequency components.

Overall, the range of dominant frequencies appear to reside below 5 Hz, closer to 1 to 2 Hz. These frequencies were found for a plume that is dominated by puffing from the

presence of large-scale turbulent dynamics in previous literature [38]. The puffs were not exactly periodic, separated by an occasional weaker puff but was found to be around 1.37 Hz and agreed with Cetegen and Kasper's correlation for low Richardson numbers. The presence of puffing inside of CV3 near the top of the interrogation region could be a possibility and further experiments are necessary to examine this phenomenon more closely and in deeper detail.

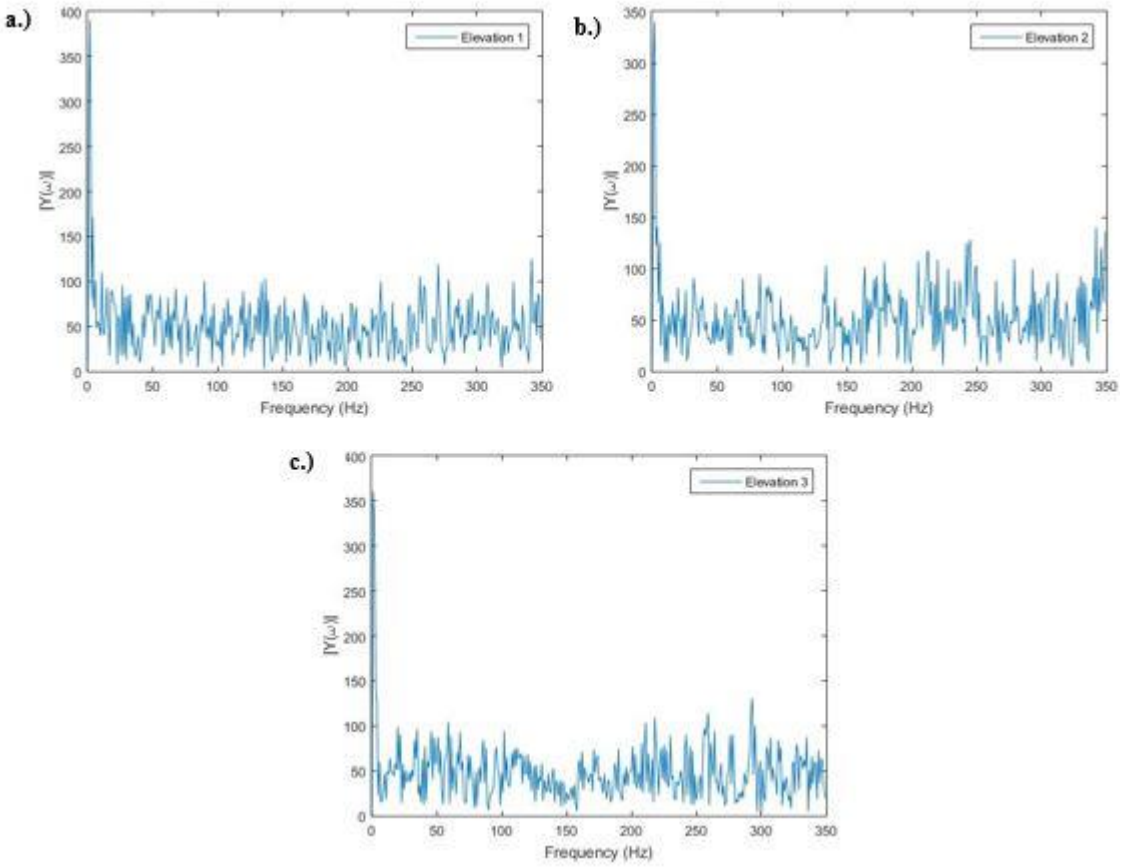

Figure 63. Discrete Fourier transform of the velocity at **a.)** 112 mm, **b.)** 117 mm and **c.)** 122 mm.

The results of the wavelet analysis show repeating, intermittent structures at different regions of CV3, resulting from the formation and advection of large and smaller toroidal vortexes. As these vortex structures move toward the top of the test volume more air is entrained as the result of instability development from the density gradient between the helium and air. Rapid acceleration and radial entrainment of the air trailing the vortex structures increase the velocity of the fluid characteristic of buoyancy effects and plume oscillation mechanisms occur. These effects may be deduced from the repeating structures centered around a particular frequency, but the velocity field is not definitive and a longer time sequence is necessary to fully characterize the flow behavior and underlying phenomena.

VI. CONCLUSION AND FUTURE WORK

A simplified high temperature gas-cooled reactor building was developed at Texas A&M University to understand the response of an actual facility to a depressurization accident scenario. By employing a set of scaling laws that preserve the thermal hydraulic phenomena that is predicted to occur during a depressurization accident in the actual HTGR reactor building, an experimental facility was realized that will assist in present and future testing of various scenarios. The geometry of the test facility was simplified to focus on characterizing the key phenomena that determine the reactor building atmospheric concentration over time without the complexity of modeling the detailed features of an actual reactor building. The simplicity of the model is dependent on a set of assumptions about the performance of the building during accident scenarios and of the intricacy of the geometry and distribution of helium inside the HPB. Finally, the scaled reference length, velocity and time for diffusion were derived based on the pertinent dimensionless numbers that portray the flow behavior and a sensible dimension that avoided very small flow paths in the simplified facility, leading to a decrease in the capabilities to obtain precise measurements using the available tools and devices.

The test facility was then outfitted with several instruments used to collect pressure, temperature and oxygen concentration measurements. The oxygen concentration was collected point-wise using oxygen sensors that determine the ratio of oxygen present depending on the quenching of emitted blue LED light from an optic

fiber. The quenching occurs from oxygen diffusing into a sensing material coated on the end of the probe and reduced the fluorescence intensity of the reemitted light in the red region of the spectrum. Other instruments installed were heating pads inside of the reactor pressure vessel model that will be implemented in future testing to replicate the actual temperature, scaled in the test facility, of the reactor cavity immediately after a depressurization accident when hot helium is ejected from the core through small or large size breaks.

The target rates were set using needle valves at the top of CV1, CV3 and CV6 to match the amount of gas that diffuses from a prototypical HTGR building in one day. This was achieved with a high degree of accuracy by constantly adjusting the needle valves until the final pressure after five minutes matched the theoretical estimation from the computed leak rate constant. The R^2 values for CV1 and CV3 were over 0.99 while less than 0.95 for CV6. The theoretical curve for CV1 matched the curve from the experimental data almost precisely. Several tests were conducted for CV3 and CV6 to ensure repeatability and accuracy in the measurements, and again, showed a high degree of similitude from computation of the R^2 values of experimental data with an exponential curve fit. The oxygen concentration measurements collected from the combined leak rate test in CV3 and CV6 showed that the profiles in both test volumes displayed little change after around 10 minutes for a sudden depressurization inside of CV3. Furthermore, flow instabilities were proposed to have developed in flow path V36 from CV3 to CV6 gravity drive flow from the density difference between helium and air that resulted in billows developing from instabilities at the interface. Taking the time

difference between the oxygen probe measurements at the minimum in CV3 and CV6, the time for helium to move from CV3 and CV6 was found to be 1.1 seconds and the velocity of the gravity current through flow path V36 was computed to be 2.31 $ft \cdot s^{-1}$.

A similar test was conducted inside of CV3 and CV6 for a rapid depressurization inside of CV6. This ensured by installing a hinged louvre that operated when the pressure inside exceeded 1 psig. The louvre actually operated at a pressure of 1.08 and depressurized almost instantaneously. Helium was continuously injected for 5 minutes after the louvre opened and the velocity across flow path V36 was around 3.63 $ft \cdot s^{-1}$, slightly faster than for the combined leak rate test in CV3 and CV6. Analysis of the oxygen concentration profile inside CV3 and CV6 show that air was forced into CV6 once the pressurized helium was injected into CV3 and is responsible for the sudden increase in pressure and oxygen concentration inside CV6 while CV3 quickly filled with helium and purged the air out of the test chamber. Various phenomena were identified including potential Rayleigh-Taylor instability development inside CV6 from the overlying air intruding into the facility and mixing with the exiting helium. Vortex development may have served to interfere with the gas refill phase of the test where air should have stratified at the bottom of CV6 and helium at the top. Diffusion of air into the helium inside CV3 was estimated to dominate after a few minutes after the initial depressurization and was compared with a theoretical model for gaseous diffusion into a semi-infinite test volume. The concentration measurements at the bottom of CV3 agree with the computation of this result over a time period of 10 minutes where some error

may have been introduced from the method for determining the diffusion constant of air into helium.

Investigation of a horizontal helium jet impacting the steam generator model were facilitated through velocity measurements collected using PIV. The velocity profiles inside of CV3 for the first second after the helium flow is discharged from the check valve is shown in Figure 54 for the first 0.25 seconds. Observation of Figure 54 shows that the helium discharged from the check valve into the ambient air with a velocity 0.45 $m \cdot s^{-1}$. Calculation of the Richardson number from Equation (77) resulted in a value slightly lower than one, indicating that the helium flow entering CV3 was not entirely a plume but was still advected by a momentum flux and displays some jet behavior. Discharged helium from the check valve immediately began to move vertically and began to exhibit vortical motion upon impact of the steam generator and advect vertically up the side towards the top of CV3. Chaotic motion of the seed particles and formation of vortical structures suggest strong turbulence at the point of impingement. As the vortical structure advects further along the interrogation region, air is entrained underneath the vortical structure and is signified qualitatively in the flow by the seeding particles closely trailing the vortex along the steam generator. Vortex development and the acceleration of the seeding particles were presumed to be attributed to Rayleigh-Taylor instabilities. Vortex formation occurs and entrains any air residing outside of the combined gas mixture, or plume that is then driven by buoyancy forces. This claim may be validated through future experiments for whole-field concentration measurements.

The flow field near the steam generator appeared to oscillate with an average frequency between the four elevations of 5 Hz and may indicative of "puffing" phenomena where where helium slowly accumulates until it reaches a sufficient volume to trigger a Rayleigh-Taylor instability caused by air overlying the lighter helium. A deeper understanding of the mean flow behavior was extracted from the resulting velocity measurements using the continuous wavelet transform and the Morlet wavelet was selected because of its previous use in analyzing turbulent behavior and has been proposed to resemble eddy structures. The results of the wavelet transform show repeating structures in all three frames with frequencies less than 20 Hz every 0.1 seconds between 0.8 and 1.1 seconds. The single-sided discrete Fourier transform the range of dominant frequencies appear to reside close to 1 to 2 Hz. This range of frequencies. Results from previous literature found that the average frequency of the velocity peaks for a plume dominated by puffing was 1.37 Hz and agreed with Cetegen and Kasper's correlation for low Richardson numbers.

Future testing should expand upon the tests included in the preliminary measurements. The tests should consider heating the gas inside of the facility, particularly CV1, to understand how the dynamics changes as a function of temperature that replicates an actual HTGR depressurization accident scenario. Other testing might consider separate configurations that incorporates CV2 along with the other test volumes connected to the test facility and create a flow path that joins CV2 with CV1. The results displayed interesting flow phenomena depending on where helium was injected and the relative flow rate upon entry into the facility. Spatial or temporal concentration or

pressure measurements will serve to capture the transient performance as air or helium is exhausted or inserted into the test facility as opposed to point-wise or localized measurements. Spatial concentration measurements can be achieved from alternative flow visualization techniques including molecular tagging velocimetry where the fluorescence of a seed particle is traced along the flow path, along with Schileren techniques that rely on the refractive index change through a mixture of gases. Other methods might include the use of pressure sensitive paint that utilizes the oxygen concentration to determine the spatial distribution of pressure along a painted surface. Applying the aforementioned equations and Kay's rule could be implemented to evaluate the oxygen concentration as the gas composition changes inside of the simplified test facility.

The development of flow instabilities as a result of a buoyant jet of helium was only hypothesized based on the corresponding flow dynamics and spectral analysis. However, the true nature of the flow field should be resolved in future flow visualization studies to either verify or append the results presented in the preliminary measurements. The results were limited to PIV measurements that may or may not have had adequate seeding or proper spatial or temporal resolution. The PIV measurements may be repeated, paying close attention to the flow field development and modify the measurement parameters accordingly such as the camera frequency, seed density distribution etc. The improved PIV results should improve upon the initial measurements conducted and, along with spatial concertation measurements, greatly assist in characterizing the flow phenomena as helium and air are interchanged.

REFERENCES

[1] "Next Generation Nuclear Plant (NGNP)," United States Nuclear Regulatory Commission, 14 December 2016. [Online]. Available: https://www.nrc.gov/reactors/advanced/ngnp.html. [Accessed 10 November 2016].

[2] "Next Generation Nuclear Plant: A Report to Congress," The U.S. Department of Energy Office of Nuclear Energy, 2010.

[3] "Very-High Temperature Reactor (VHTR)," GEN IV International Forum, 2017. [Online]. Available: https://www.gen-4.org/gif/jcms/c_42153/very-high-temperature-reactor-vhtr. [Accessed 9 November 2016].

[4] S. Ball, "Sensitivity Studies of Modular High-Temperature Gas-Cooled Reactor Postulated Accidents," *Nuclear Engineering and Design,* vol. 2006, no. 236, pp. 454-462, October 2005.

[5] D. Chapin, S. Kiffer and J. Nestell, "The Very High Temperature Reactor: A Technical Summary," MPR Associates, Inc., Alexandria, 2004.

[6] "AREVA High Temperature Gas-Cooled Reactor: Information Kit," March 2014. [Online]. Available: http://us.areva.com/home/liblocal/docs/Nuclear/HTGR/HTGR-InfoKit-2014-03.pdf. [Accessed 9 November 2016].

[7] J. Beck and L. Pincock, "High Temperature Gas Cooled Reactors Lessons Learned Applicable to the Next Generation Nuclear Plant," Idaho National Laboratory/10-

19329 Revision 1, April 2011. [Online]. Available: https://inldigitallibrary.inl.gov/sti/5026001.pdf. [Accessed 10 November 2016].

[8] W. Slover, M. Bridges, R. Chambers and L. Loflin, "Containment Versus Confinement for High-Temperature Gas Reactors," Electric Power Research Institute (EPRI) Nuclear Maintenance Application Center (NMAC), Charlotte, 2005.

[9] "High Temperature Gas Cooled Reactor Fuels and Materials," International Atomic Energy Agency, Vienna, 2010.

[10] "General Atomics' Prismatic Modular High Temperature Gas Cooled Reactor," [Online]. Available: https://aris.iaea.org/PDF/PrismaticHTR.pdf. [Accessed 11 November 2016].

[11] J. Saurwein, "Next Generation Nuclear Plant (NGNP) Prismatic HTGR Conceptual Design Project - Final Technical Report," General Atomics, San Diego, 2011.

[12] R. D. Blevins, Applied Fluid Dynamics Handbook, Krieger: Van Nostrand Reinhold Co., 1984.

[13] "Probabilistic Risk Assessment for the Standard Modular High Temperature Gas-Cooled Reactor," General Atomics, San Diego, 1987.

[14] S. R. Yang, M. Silberberg, C. Fullerton, T. Nguyen, R. Vaghetto and Y. Hassan, "Experimental Study on a Simplified HTGR Reactor Building Response to Depressurzation Accidental Scenarios," in *2016 HTR Conference - International Topical Meeting on High Temperature Reactor Technology*, Las Vegas, 2016.

[15] J. Reyes, J. Groome, B. Woods, B. Jackson and T. D. Marshall, "Scaling Analysis for the High Temperature Gas Reactor Test Section (GRTS)," *Nuclear Engineering and Design,* vol. 2010, no. 240, pp. 397-404, 2009.

[16] M. Ishii and I. Kataoka, "Scaling Laws for Thermal-Hydraulic System Under Single Phase and Two-Phase Natural Circulation," *Nuclear Engineering and Design,* vol. 1984, no. 81, pp. 411-425, 1983.

[17] H.-G. Woo, Advanced Functional Materials, New York City: Springer, 2011.

[18] "Oxygen Sensing," Ocean Optics, [Online]. Available: http://oce.oceanoptics.com/measurementtechnique/oxygen-sensing/. [Accessed 13 November 2016].

[19] E. A. Permiakov, Luminescent Spectroscopy of Proteins, Boca Raton: CRC Press, 1993.

[20] "NeoFox Phase Fluorometer Installation and Operation Manual," Halma plc, Cincinatti, 2015.

[21] T. E. Hicks, D. Petti, J. C. Kinsey and G. Gibbs, "Modular HTGR Safety Basis and Approach," Idaho National Laboratory Next Generation Nuclear Plant Project, Idaho Falls, 2011.

[22] H. G. Jin, H. C. No and H. I. Kim, "Stratified Flow-Induced Air-Ingress Accident Assessment of the GAMMA Code in HTGRs," *Nuclear Engineering and Design,* vol. 2011, no. 241, pp. 3216-3223, 2011.

[23] D. J. J. Arcilesi, K. T. Ham, H. I. Kim, X. Sun, R. N. Christensen and C. H. Oh, "Scaling and Design Analyses of a Scaled-Down, High-Temperature Test Facility for Experimental Investigation of the Initial Stages of a VHTR Air-Ingress Accident," *Nuclear Engineering and Design,* vol. 2015, no. 288, pp. 141-162, 2015.

[24] C. H. Oh and E. S. Kim, "Air-Ingress Analysis: Part 1. Theoretical Approach," *Nuclear Engineering and Design,* vol. 2011, no. 241, pp. 203-212, 2010.

[25] Y. Cengel and M. Boles, Thermodynamics: An Engineering Approach, New York City: McGraw Hill-Education, 2014.

[26] A. G. Kikkert, *Buoyant Jets with Two and Three-Dimensional Trajectories,* Christchurch: Thesis for the Doctor of Philosophy in Civil Engineering at the University of Canterbury, 2006.

[27] E. A. Hirst, "Analysis of Round, Turbulent, Buoyant Jets Discharged to Flowing Stratified Ambients," Oak Ridge National Laboratory, Oak Ridge, 1971.

[28] A. Dewan, J. H. Arakeri and J. Srinivasan, "A Note on High Schmidt Number Laminar Buoyant Jets Discharged Horizontally," *International Communications in Heat and Mass Transfer,* vol. 19, no. 5, pp. 721-731, 1992.

[29] J. Xiao, J. Travis and W. Brietung, "Non-Boussinesq Integral Model for Horizontal Turbulent Buoyant Round Jets," *Science and Technology of Nuclear Installations,* vol. 2009, no. ID 862934, pp. 1-7, 2009.

[30] S. N. Michas and P. N. Papanicolaou, "Horizontal Round Heated Jets into Calm Uniform Ambient," *Desalination,* vol. 2009, no. 248, pp. 803-815, 2008.

[31] G. H. Jirka, "Integral Model for Turbulent Buoyant Jets in Unbounded Stratified Flows. Part I: Single Round Jet," *Environmental Fluid Mechanics,* vol. 2004, no. 4, pp. 1-56, 2003.

[32] Y. A. Cengel and J. M. Cimbala, Fluid Mechanics, McGraw-Hill Education: New York, 2013.

[33] R. J. Lowe, J. W. Rottman and P. F. Linden, "The Non-Boussinesq Lock-Exchange Problem. Part 1. Theory and Experiments," *Journal of Fluid Mechanics,* vol. 537, pp. 101-124, 2005.

[34] C.-S. Yih, Dynamics of Non-Homogeneous Fluids, London: MacMillan, 1965.

[35] J. E. Simpson, Gravity Currents: In the Environment and the Laboratory, Cambridge: Cambridge University Press, 1999.

[36] H. P. Gröbelbauer, T. K. Fanneløp and R. E. Britter, "The Propogation of Intrustion Fronts of High Density Ratios," *Journal of Fluid Mechanics,* vol. 250, pp. 669-687, 1992.

[37] K. Ohmori, "Convergence of the Interface in the Finite Element Approximation for Two-Fluid Flows," Toyoma University, Gofuku.

[38] T. J. O'Hern, E. J. Weckman, A. L. Gerhart, S. R. Tieszen and R. W. Schefer, "Experimental Study of a Turbulent Buoyant Helium Plume," *Journal of Fluid Mechanics,* vol. 544, pp. 143-171, 2005.

[39] S. P. Wasik and K. E. McCulloh, "Measurements of Gaseous Diffusion Coefficients by a Gas Chromatographic Technique," *Journal of Research of the National Bureau of Standards - A. Physics and Chemistry*, vol. 73A, no. 2, pp. 207-211, 1969.

[40] B. R. Bird, W. E. Stewart and E. N. Lightfoot, Transport Phenomena, Hoboken: John Wiley & Sons, 2006.

[41] "Choked Flow of Gases," O'Keefe Controls Co., [Online]. Available: http://www.okcc.com/pdf/choked%20flow%20of%20gases%20pg.48.pdf. [Accessed 3 January 2017].

[42] B. M. Cetegen, "Measurements of Instantaneous Velocity Field of a Non-Reacting Pulsating Buoyant Plume by Particle Image Velocimetry," *Combustion Science and Technology*, vol. 123, pp. 377-387, 1996.

[43] B. M. Cetegen and K. D. Kasper, "Experiments on the Oscillatory Behavior of Buoyant Plumes of Helium and Air-Mixtures," *Physics of Fluids*, vol. 8, no. 11, pp. 2974-2984, 1996.

[44] A. Graps, "An Introduction to Wavelets," *IEEE Computational Science and Engineering*, vol. 2, no. 2, 1995.

[45] N. D. Kelley, R. M. Osgood, J. T. Bialasiewicz and A. Jakubowski, "Using Time-Frequency and Wavelet Analysis to Assess Turbulence/Rotor Interactions," in *19th American Society of Mechanical Engineers (ASME) Wind Energy Symposium*, Reno, 2000.

[46] M. L. S. Indrusiak and S. V. Möller, "Wavelet Analysis of Experimental Turbulence Time Series," in *IV Escola de Primavera de Transição e Turbulência at Universidade Federal do Rio Grande do Sul*, Rua Sarmento Leite, 2004.

[47] H. Tennekes, A First Course in Turbulence, Cambridge: The MIT Press, 1972.

APPENDIX A

A.1 Check Valve Operating Pressure Verification

Repeatability and reliability was determined for the check valve by performing several tests at different pressures to ensure that the check valve consistently operated at the same pressure. Operation of the check valve means that the spring-loaded seat opened when the desired differential pressure was applied. The tests were conducted by first allowing for communication between CV1 and the bypass system with the rest of the facility through flow path V13. A gas line with an adjustable valve at the end was connected from the helium tank regulator to CV1 through the quick-disconnect fitting at the top of the facility. A compression fitting with the bored through hole was installed into CV6 without any instrumentation, allowing for gas leakage through the fitting to the outer atmosphere. A mixture of soap and water was coated at the intrusion to the compression fitting.

Once helium was injected into the facility through the adjustable valve at the top of the facility, helium would fill CV1 until exceeding the pressure limit of the check valve. This allowed for one-way flow into the rest of facility, including CV6. Once helium activated the check valve, the pressurized helium would produce bubbles in the soap and water mixture coated on the compression fitting. This indicated that the check valve had operated and the corresponding pressure was noted. This repeated seven times

for five separate pressures, except for 4 psig and was only repeated six times for that pressure. The results of the preliminary check valve tests are shown below in Table A.1

Table A.1. Check valve operating pressure verification tests.

Pressure (psig)	CV6-1	CV6-2	CV6-3	CV6-4	CV6-5	CV6-6	CV6-7
1	0.35	0.36	0.34	0.23	0.35	0.34	0.32
2.5	0.36	0.32	0.21	0.22	0.25	0.33	0.33
3	0.25	0.35	0.35	0.35	0.34	0.32	0.36
4	0.31	0.23	0.38	0.35	0.37	0.44	N/A
5	0.34	0.37	0.34	0.33	0.35	0.69	0.36

The results show that, despite a couple of extraneous pressure values the check valve consistently operated at around 0.35 psig with low deviation between measurements.